Inclusive strange vector and tensor meson production in hadronic Z^0 decays

Allan J. Skillman

Department of Physics and Astronomy

A thesis submitted to The University of Manchester for the degree of Doctor of Philosophy in the Faculty of Science and Engineering.

September 1994

Contents

Abstract

Measurements have been made in the OPAL experiment at LEP of the inclusive production of strange vector $\phi(1020)$ and $K^*(892)^0$ mesons, and the tensor meson $K_2^*(1430)^0$. The overall multiplicities per hadronic Z^0 decay have been determined to be: $0.100 \pm 0.004 \pm 0.007$ $\phi(1020)$ mesons, $0.74 \pm 0.03 \pm 0.03$ $K^*(892)^0$ mesons and (for $x_E < 0.3$) $0.19 \pm 0.04 \pm 0.06$ $K_2^*(1430)^0$ mesons. The measurements for the vector states update previously published results based on lower statistics, while the $K_2^*(1430)^0$ rate represents the first measurement of a strange tensor state in Z^0 decay. Both the overall production rates, and normalised differential cross sections for the vector states, have been compared to JETSET and HERWIG predictions. The peak positions in the $\xi = \ln(1/x_p)$ distributions have been measured and found to be consistent with measurements of other hadron states.

No portion of the work referred to in this thesis has been submitted in support of an application for another degree or qualification of this or any other university or other institute of learning.

The author was educated at Bishop Stopford School Kettering, between 1981 and 1988. In 1991 he obtained a 1st class BSc. (Hons.) in Physics at the University of Lancaster. The work presented in this thesis was conducted at the University of Manchester and the European Centre for Particle Physics, CERN, Geneva.

Chapter 1

Introduction

In this thesis, results are presented from a sample of 1.2 million multihadronic Z^0 decays recorded by the OPAL detector at LEP between 1990 and 1992. Measurements are given of the inclusive production rates of the strange vector $K^*(892)^0$ and $\phi(1020)$ mesons, updating the previous OPAL results [1] and providing a significant improvement in precision. In addition the first measurement of the strange tensor $K_2^*(1430)^0$ meson is reported. The K^* mesons are reconstructed in their $K^{\pm}\pi^{\mp}$ decay modes, and the $\phi(1020)$ in K^+K^-.

The inclusive production rates for a large number of identified meson and baryon states have now been measured in hadronic Z^0 decays. In the meson sector, results have been published for all the pseudoscalar states [2, 3, 4] and all the vector mesons [1, 5, 6] except the $\omega(782)$. However, only one scalar meson, the $f_0(975)$, and one tensor meson, the $f_2(1270)$, have been reported [6].

A number of QCD-based Monte Carlo models exist which allow interpretation of measurements of meson production. In JETSET [7] for example a number of variable parameters can be tuned to reproduce the observations. The values of these parameters may be interpreted as providing information about the nature of the fragmentation process. Measurements of light mesons, as well as of baryons, in all of the various spin-parity and strangeness states are therefore required to provide a full picture of the parton fragmentation.

Using the measurements reported in this thesis for the vector states, studies are made of the fragmentation functions and overall multiplicities and also the dependence of the differential cross sections on the variable $\xi = \ln(1/x_p)$, where x_p is the scaled meson momentum. This allows comparisons to be made with predictions of the modified leading log approximation in QCD, using local parton-hadron duality. The measured $K_2^*(1430)^0$ rate is used to alter the JETSET parameter which governs the level of tensor meson production. The effect of this parameter on the inclusive rates of other particles is also investigated.

The production of $\phi(1020)$ with a large fraction of the beam energy is also investigated. According to JETSET Monte Carlo these mesons have a high probability of containing one of the primary quarks from the Z^0 decay. A preliminary study is made of how this characteristic can be used to determine whether properties such as quark polarisation are transferred to the final state hadrons in fragmentation.

Chapter 2

Theory

2.1 The Standard Model

The Standard Model [8] is a set of quantum field theories which describe the strong, weak and electromagnetic interactions of quarks and leptons. These fermions are divided into three generations, each containing two quarks and two leptons, as shown in table 2.1. A corresponding set of antiparticles also exists. The theory is based on the principle of local gauge invariance with respect to the lie group: SU(3)×SU(2)×U(1). Interactions between the fermions are mediated by gauge bosons : γ, $W^{\pm}$, Z^0 and gluons. The masses of the fermions and the bosons associated with the weak interactions are generated through the process of spontaneous symmetry breaking, by the Higgs mechanism [8].

Generation	quarks		leptons	
	$Q = 2/3$	$Q = -1/3$	$Q = -1$	$Q = 0$
1st	u	d	e	ν_e
2nd	c	s	μ	ν_μ
3rd	t	b	τ	ν_τ

Table 2.1: The three generations of quarks and leptons in the Standard Model, grouped according to their electromagnetic charge Q.

2.1.1 The electroweak sector

In the Standard Model, the electromagnetic and weak interactions are combined into a single theory based on local SU(2)×U(1) gauge invariance [9]. The theory is chiral with the left and right handed components of the fermion fields treated differently. The 'handedness' of a field ψ is defined in terms of the projection operators, $(1 \pm \gamma_5)$, as follows :

$$\psi_L = \frac{(1-\gamma_5)}{2}\psi \qquad ; \qquad \psi_R = \frac{(1+\gamma_5)}{2}\psi \ , \tag{2.1}$$

where γ_5 is the chirality operator. The left handed quark and lepton fields form SU(2) doublets, whereas the right handed fields form SU(2) singlets :

$$\text{quarks} : \begin{pmatrix} U \\ D \end{pmatrix}_L ; U_R ; D_R \qquad\qquad \text{leptons} : \begin{pmatrix} \nu \\ l \end{pmatrix}_L ; l_R \ .$$

Here U, D and ν, l represent one of the three generations of quarks and leptons respectively. There is no experimental evidence for the existence of right handed neutrinos and so ν_R fields are not included in the theory. The multiplets are described in terms of two quantum numbers, weak-isospin, T, from the SU(2) symmetry and hypercharge, Y, from U(1). The latter is defined in such a way that the electromagnetic charge Q, written

$$Q = T_3 + \frac{Y}{2} \ , \tag{2.2}$$

is the same for the left and right handed components of each fermion. Local gauge invariance in the electroweak Lagrangian is provided by the addition of three SU(2) vector bosons W^i and one U(1) vector boson B. These are interpreted as the mediators of the weak and electromagnetic forces. Note that the W^i fields only couple to the left handed fermion fields (which have non-zero weak-isospin), providing a mechanism for parity violating interactions which have been experimentally observed. The physical charged weak bosons are formed from a mix of the fields W^1 and W^2,

$$\mathrm{W}^{\pm} = \mathrm{W}^1 \pm i\mathrm{W}^2 \ . \tag{2.3}$$

In order to explain the 'weakness' of the weak force without defining a coupling constant which is much smaller than that used in electromagnetism, i.e. $\alpha_{\mathrm{W}} \ll \alpha$,

masses are introduced for the weak gauge bosons. These masses, according to the uncertainty principle, restrict the range of the force and hence make it weak.

These masses cannot be included directly into the Lagrangian without destroying the local gauge invariance of the theory. Instead the Higgs mechanism [8] is used. An SU(2) doublet of scalar fields is introduced,

$$\mathrm{H} = \begin{pmatrix} \mathrm{H}^{+} \\ \mathrm{H}^{0} \end{pmatrix}_{Y=1} , \tag{2.4}$$

with a potential defined in such a way, figure 2.1, that it induces a non-zero vacuum expectation value for the Higgs field. This means that the vacuum state cannot be SU(2)×U(1) invariant. However by the definition of charge, Q, in equation 2.2, the vacuum is electromagnetically neutral and so the U(1) symmetry is retained. This process, where the theory is invariant but the vacuum is not, is known as spontaneous symmetry breaking. By this mechanism the weak fields gain rest masses, but as the U(1) symmetry is not broken, the photon remains massless. Excitations from the vacuum produce a massive neutral Higgs particle, and three massless 'Goldstone bosons', which can be interpreted as the longitudinal components of the weak gauge fields W^{i}.

The addition of mass terms in the Lagrangian, through the Higgs mechanism, causes the neutral fields W^{3} and B to mix, and form the physical fields Z^{0} and γ, the photon. The mixing angle θ_{W} is an important observable in the Standard Model. Fermion mass terms are introduced through Yukawa type interactions with the Higgs scalar doublet H.

2.1.2 The strong interactions : QCD

Strong interactions between quarks are described in the Standard Model in terms of a local SU(3) gauge symmetry. Unlike the electroweak sector, the theory is not chiral; the left and right handed components of the quark fields undergo the same interactions. In order to make the Lagrangian locally gauge invariant under this symmetry group, eight gauge fields are required, called gluons. As the SU(3) symmetry in the theory is exact, these gauge bosons are all massless. In this respect, it

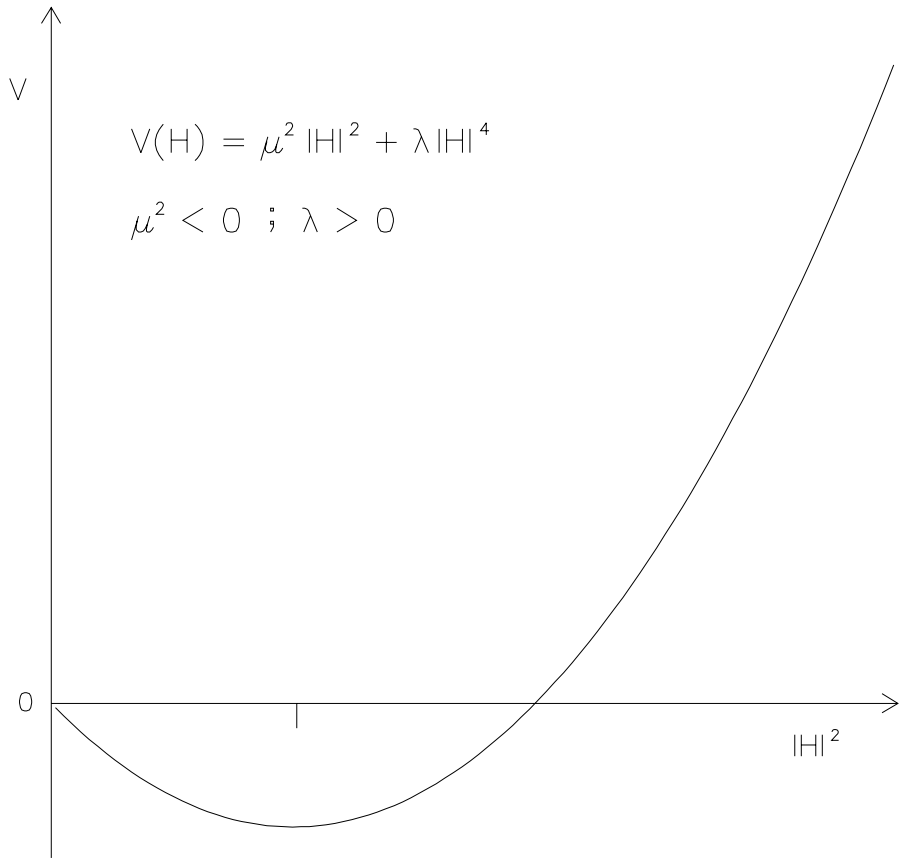

Figure 2.1: The Higgs potential, with a minimum at $|H|^2 \neq 0$. This feature gives rise to a non-zero vacuum expectation value for the Higgs field.

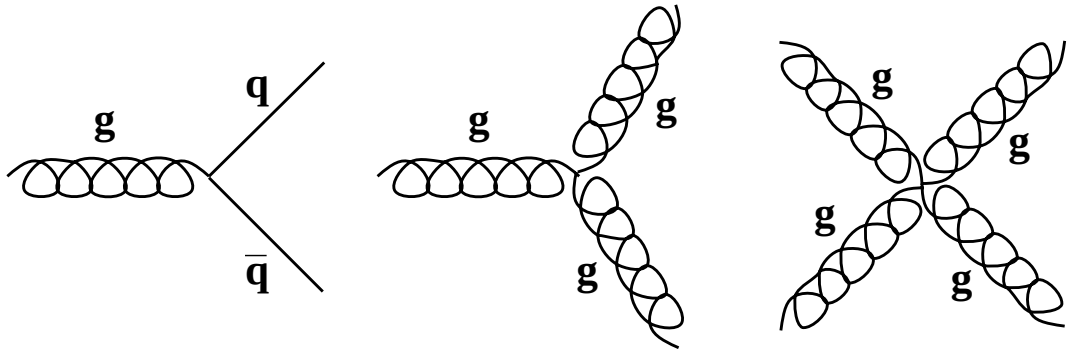

Figure 2.2: QCD interactions involving quarks and gluons, including those between the gauge bosons which are not present in theories based on abelian symmetry groups, such as electromagnetism.

is like quantum electrodynamics, QED [10], the gauge theory based on U(1) symmetry, developed to describe electromagnetic interactions. The charge associated with the symmetry is called colour, and so the theory is referred to as quantum chromodynamics (QCD). The most important difference in terms of physics between SU(3) and U(1) symmetries is the non-abelian nature of the higher order group. This gives rise to gauge fields which carry the colour charge and so can interact directly with each other as well as with the quarks, as shown in figure 2.2. These interactions are not possible in electromagnetism as the photon is a neutral object. The existence of diagrams like these in the expression for the strong coupling constant, α_s, cause it to depend on the energy scale. At high energy α_s is small, allowing calculations to be made using perturbation theory, but at energy scales less than 1 GeV the coupling is very large. In this region the perturbative approach breaks down.

The non-abelian properties of the SU(3) symmetry also lead to a gluonic potential which is approximately proportional to the distance between coloured objects. This implies that quarks and gluons may not exist on their own, but only in colour singlets. This idea is known as confinement. The simplest possible 'colourless' combinations of quarks are $q\bar{q}$ and qqq states; these correspond to the observed mesons and baryons. Bound states of more than three quarks, and states made up of gluons are also theoretically possible, but none have been unambiguously observed.

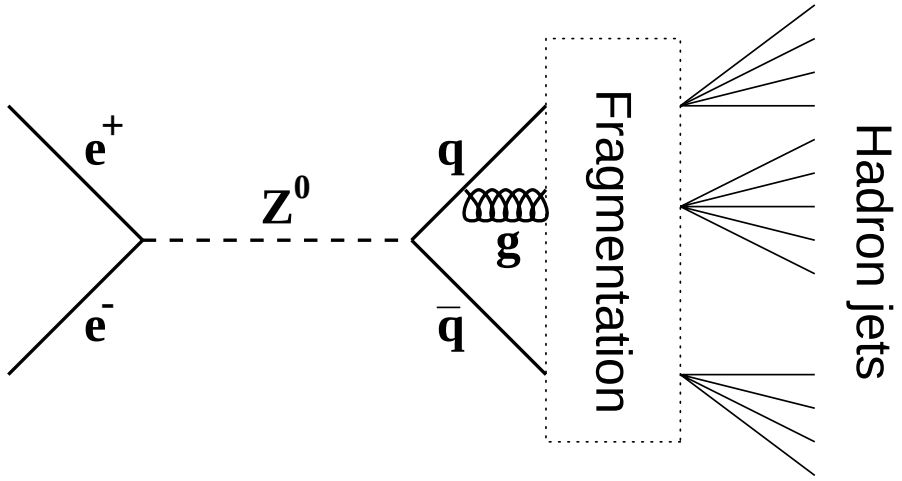

Figure 2.3: The production of hadron jets in e^+e^- annihilation through the non-perturbative process of fragmentation.

2.2 Multihadronic Z^0 decays at LEP

At LEP, the dominant process is electron-positron annihilation to Z^0, which then decays to fermion-antifermion pairs. The process can also take place via the exchange of a virtual photon, γ^*, but the rate is small as the e^+e^- centre of mass is close to the Z^0 mass. For all fermions, the initial interaction can be described using electroweak perturbation theory.

As the particles move away from the interaction region, the energy scale decreases from $Q^2 \sim M_Z^2$. In the case of $q\bar{q}$ production, this decrease in energy scale causes the strong coupling constant α_s to increase, until a non-perturbative region is reached. Here confinement leads to the production of hadrons from the quarks through a process known as fragmentation. The kinematics of the interaction cause the final states to be collimated into jets of particles, which are observed by the detectors. Events of this type are usually called multihadronic. The primary quarks may radiate hard gluons in a process similar to bremsstrahlung in electromagnetism. These gluons will also fragment into hadrons, resulting in three or more jets in the final state. A diagrammatic representation of the process $e^+e^- \rightarrow$ jets is shown in figure 2.3.

As the fragmentation process happens in a non-perturbative region, there is no reliable way to describe it in QCD, and hence to predict the properties of the final state hadrons. Instead a number of QCD-based models have been developed which simulate the decay of the Z^0 to quarks and use various pictures of fragmentation to produce final state hadrons. Two widely used models of this type are JETSET [7] and HERWIG [11], which are described in the next section. Other Monte Carlo models commonly used in multihadron analyses are ARIADNE [12], COJETS [13] and PARJET [14].

On the other hand, there are a few concepts which allow some predictions about the inclusive particle spectra to be made using perturbative QCD. One such idea is 'local parton-hadron duality' (LPHD) [15]. In this scheme, the spectra of the final state hadrons are directly related to those of the quarks and gluons present before fragmentation. This means the fragmentation process can be bypassed and calculations can be made using perturbative methods. One such method, which has been used together with the LPHD hypothesis, is the modified leading logarithm approximation (MLLA) [16]. Although a great deal of the detail of multihadronic events is lost in the MLLA+LPHD framework, it does make certain predictions about the momentum spectra of the hadrons. One such prediction, investigated in this thesis, is that the inclusive differential cross sections of hadrons with respect to the variable $\xi = \ln(1/x_p)$, where x_p is the scaled hadron momentum, has a Gaussian-like shape, the peak position of which decreases linearly with increasing hadron mass.

2.3 Monte Carlo models: JETSET and HERWIG

The JETSET and HERWIG programs both simulate the production of final state hadrons in electron-positron annihilation in four distinct stages. First a quark-antiquark pair is produced though the interaction $e^+e^- \rightarrow Z^0 \rightarrow q\bar{q}$; to a first approximation this process is electroweak and is calculated using perturbative electroweak theory. Processes such as initial and final state radiation are also included in this stage.

The quarks are then allowed to radiate gluons. These gluons can subsequently

decay into quarks and other gluons, and possibly diquarks. The resulting particles (including the primary quarks from the Z^0 decay) are generally referred to as partons. This bremsstrahlung process is in theory calculable using perturbative QCD. The simplest approach to the calculation, using matrix elements, has been found to be of little use at LEP energies, as calculating the higher order terms required to account for the observed event structures is extremely difficult. Instead the parton shower approach [17] is used, which is based on the leading logarithm approximation. The partons produced are then fragmented into hadrons using phenomenological models. Finally unstable hadrons are allowed to decay to final state particles according to measured branching ratios.

The main difference between the two programs lies in the particular model used to carry out the fragmentation process. JETSET uses 'string fragmentation', where colour flux tubes, or strings, are extended between partons. HERWIG uses the 'cluster fragmentation' scheme, where partons are combined into colourless clusters which decay into hadrons. Figure 2.4 shows a diagrammatic representation of the JETSET production scheme.

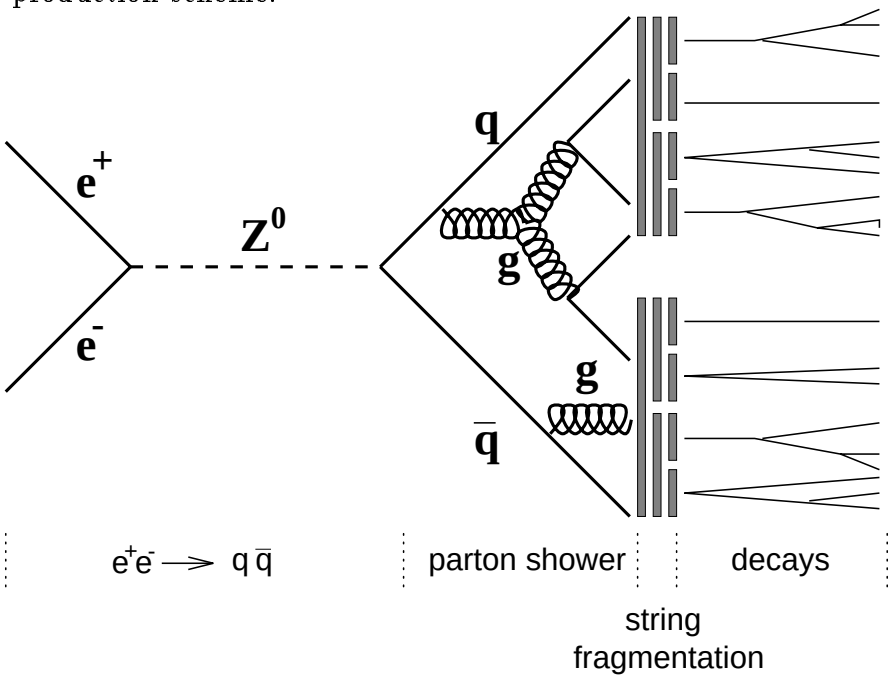

Figure 2.4: The JETSET scheme for the production of multihadronic events from e^+e^- annihilation, using string fragmentation. The process evolves with time from left to right.

2.3.1 String fragmentation in JETSET

The fragmentation picture used by JETSET is based on the Lund model, and is often referred to as Lund symmetric fragmentation. The model uses the idea of linear confinement between quark-antiquark pairs suggested by QCD. In the simplest possible case, a $q\bar{q}$ produced in e^+e^- annihilation with no gluon radiation, confinement is described in terms of a colour dipole field. Unlike in electromagnetism, the dipole field is not spread in the transverse direction, but is closely packed into a tube-like structure due to the coloured nature of the gluonic field, figure 2.5. A 'colour flux tube' of this type can be described using the dynamics of a massless relativistic string, with potential energy linearly proportional to the length of the tube. Using hadron spectroscopy the string constant of such a string (energy stored per unit length) can be deduced to be ~ 1 GeV/fm.

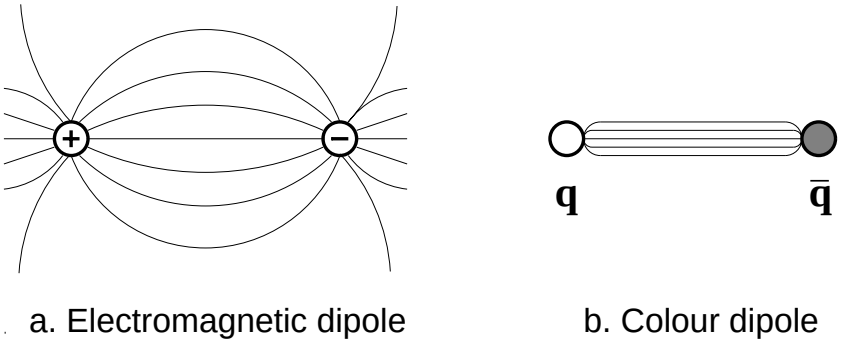

Figure 2.5: Comparison of the fields due to electromagnetic and colour dipoles. The colour carried by the gluons causes the $q\bar{q}$ field to be concentrated into a 'flux tube'.

As the quark and antiquark move apart the potential energy in the string increases until a break occurs and a new $q\bar{q}$ is produced. In Lund fragmentation, this process continues until the energy in all the string pieces is such that no further $q\bar{q}$ can be created. The remaining fragments become the final state hadrons, figure 2.6. This picture lends itself well to the formation of mesons, but the production of baryons in string fragmentation is not so well understood. Two mechanisms exist in JETSET, shown in figure 2.7. The simplest involves the production of a diquark-antidiquark pair ($qq\bar{q}\bar{q}$) in the break up of a string. The second more complex mechanism does not involve diquarks, rather the production of two quark-antiquark pairs one after the other. This scenario is called the 'popcorn mechanism' [18].

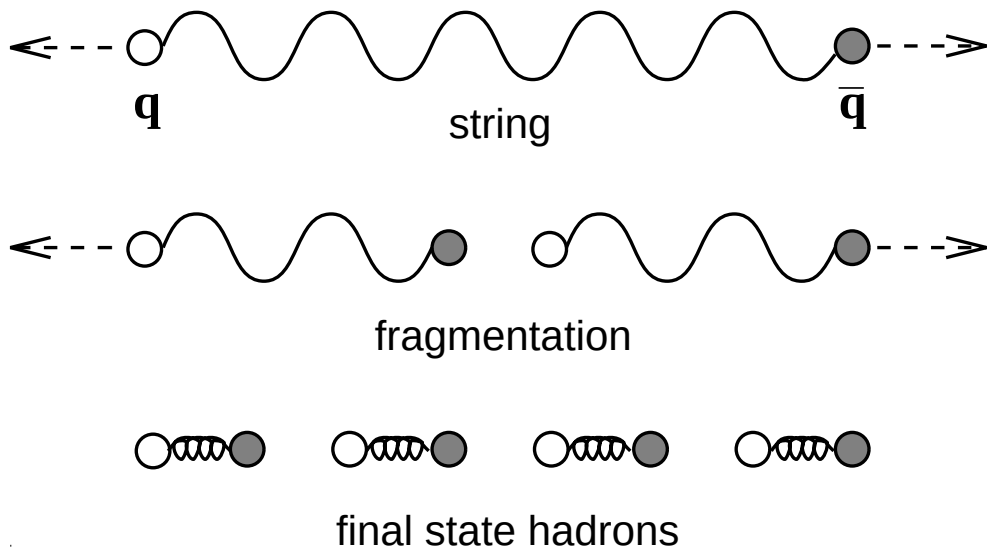

Figure 2.6: The Lund string fragmentation process for a simple $q\bar{q}$ system.

Experimental results concerning the correlations between baryon-antibaryon pairs produced in LEP events [19], tend to favour a larger amount of popcorn production relative to diquark production, but the results are not very conclusive.

The string mechanism is not very predictive in terms of the spin properties of the resulting hadrons. Instead JETSET includes a number of variable phenomenological parameters which govern the relative amount of each state produced.

When the partons involved in the fragmentation include gluons as well as quarks, as in the full simulation of multihadronic events, the string picture becomes more complicated. For a $q\bar{q}g$ event the string is stretched between the neighbouring quarks via the gluon, so it forms a 'kink' in the string. To a first approximation, when fragmentation occurs in this setup a hadron will be produced at the gluon 'kink' together with a $q\bar{q}$ pair. This pair and the original quarks form the ends of two new strings, which fragment as before.

The model is said to be symmetric because the fragmentation is the same no matter which end of a string is considered the starting point, i.e. the energy and momentum given to the hadrons is equivalent whether the fragmentation is initiated at the quark end of the string or at the antiquark end. This feature of Lund fragmentation constrains the shape of the associated fragmentation function which

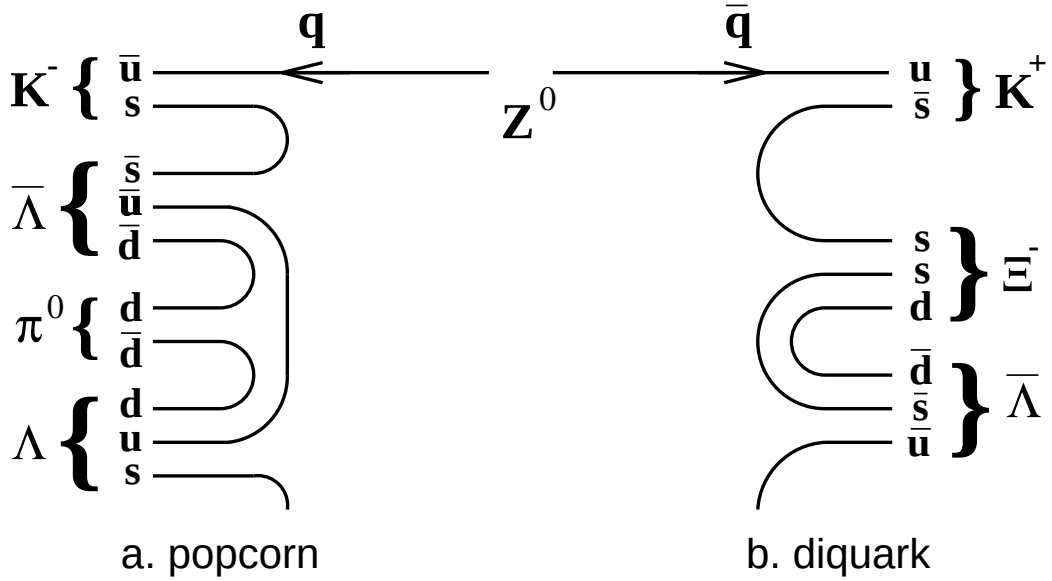

Figure 2.7: The two mechanisms for baryon production used in JETSET string fragmentation.

is defined as the differential cross section of hadrons with respect to the fraction of the total parton energy carried by the particles.

2.3.2 Cluster fragmentation in HERWIG

In HERWIG the final state hadrons are created using cluster fragmentation from the quarks, diquarks and gluons produced in the parton shower process. This model, like string fragmentation, uses the QCD property of confinement between coloured objects. As described above, this property causes a parton to be close in phase-space (and real space) to a parton of opposite colour. This is true both for the production of $q\bar{q}$ pairs and the more complex situation in a parton shower. The partons can therefore be associated with colourless low mass objects called clusters. The clusters may be composed of quark-antiquark pairs or diquark-antidiquark systems. Gluons present at the end of the parton shower are split into quark-antiquark pairs, which are clustered in the same way. Figure 2.8 shows the simplest case where the clusters contain only $q\bar{q}$ pairs.

The mechanism by which these clusters decay into hadrons is governed by their mass and flavour content. For a cluster C composed for example of quarks q_A and $\bar{\mathrm{q}}_B$, two mass limits are defined :

$$M_u = m(\mathrm{q}_A, \bar{\mathrm{u}})_{\mathrm{lightest}} + m(\mathrm{u}, \bar{\mathrm{q}}_B)_{\mathrm{lightest}} \tag{2.5}$$

and

$$M_d = m(\mathrm{q}_A, \bar{\mathrm{d}})_{\mathrm{lightest}} + m(\mathrm{d}, \bar{\mathrm{q}}_B)_{\mathrm{lightest}} \tag{2.6}$$

where $m(\mathrm{q}_1, \bar{\mathrm{q}}_2)_{\mathrm{lightest}}$ is the lightest possible hadron with quark composition $(\mathrm{q}_1, \bar{\mathrm{q}}_2)$. If the cluster mass M_C is lower than both M_u and M_d then it will be transformed into a single final state, whose identity is determined as the lowest mass hadron with flavour structure equal to that of the cluster.

Most of the clusters formed from the partons will have masses greater than one of the limits and will undergo two-body decays to form hadrons. In this scheme a $\mathrm{q}\bar{\mathrm{q}}$ pair or $\mathrm{qq}\bar{\mathrm{q}}\bar{\mathrm{q}}$ system is created. The flavour of $\mathrm{q}\bar{\mathrm{q}}$ pairs are chosen from u, d, c, s, t, and b quarks. In the case of diquark-antidiquark systems, the flavours are chosen from the following combinations: uu, ud, us, dd, ds and ss, paired with the appropriate $\bar{\mathrm{q}}\bar{\mathrm{q}}$. This quark-antiquark pair or diquark-antidiquark system is combined with the cluster to form a pair of mesons or baryons. For example, for a cluster $C(\mathrm{q}_A, \bar{\mathrm{q}}_B)$, combined with $\mathrm{q}_C\bar{\mathrm{q}}_C$, the result will be two mesons m_1 and m_2 made up of $(\mathrm{q}_A, \bar{\mathrm{q}}_C)$ and $(\mathrm{q}_C, \bar{\mathrm{q}}_B)$.

The combined mass of the two lightest possible hadrons must not exceed the mass of the cluster, to prevent for example the production of top hadrons from the decay of non-top clusters. The combination of clusters containing diquarks with diquark-antidiquark systems is also not allowed, preventing the formation of exotics in the fragmentation process. The low cluster mass scale used in the model results in hadrons with limited transverse momentum, producing a jet structure, as observed in experiment.

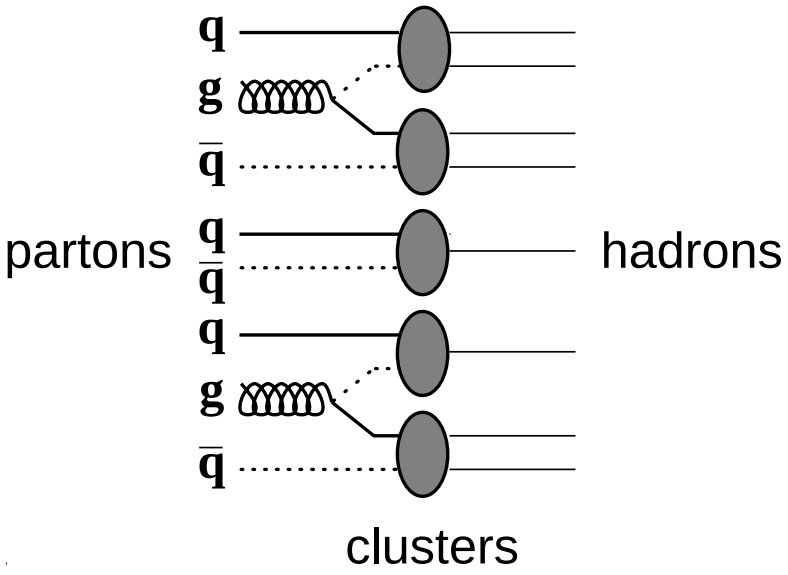

Figure 2.8: The cluster fragmentation picture, as used by the HERWIG Monte Carlo program. Note that gluons are forcibly converted to $q\bar{q}$ before clustering is attempted.

The identities of the hadrons produced in a two-body cluster decay are determined by a phase-space factor, which includes both the mass and the spin degeneracy of the possible final states. For example, a $u\bar{u}$ cluster more is likely to decay to $\pi^+\pi^-$ rather than the higher mass state K^+K^-. Also, given enough mass, a similar cluster is likely to decay to a state containing a tensor meson, such as the $f_2(1270)$, rather than the equivalent axial vector state, $a_1^0(1260)$, due to the spin factors involved. This is very different to JETSET, where the spectrum of hadrons is governed by phenomenological parameters. The concept of cluster fragmentation represents an implementation of local parton-hadron duality, with the final state hadrons linked directly to the initial partons.

2.3.3 The use of Monte Carlo in multihadron analysis

As mentioned above, in the absence of a viable non-perturbative tool to describe fragmentation using the QCD Lagrangian, Monte Carlo models such as JETSET and HERWIG are invaluable in any analysis which involves strong interactions. For

example, in the study of the perturbative QCD processes involved in $Z^0 \rightarrow q\bar{q}$ a reliable model is required to 'strip away' the hadrons to reveal the parent partons.

The parameters in JETSET can be 'tuned' to reproduce the results of a real experiment, for measured quantities such as inclusive production rates and the shapes of hadron fragmentation functions. The values of the parameters can then be interpreted as providing information about the underlying fragmentation process. HERWIG, with very few parameters and a different picture of hadronisation, can be used in many situations as a cross check for any bias introduced by using the string fragmentation scheme.

Chapter 3

The OPAL detector

3.1 The LEP machine

OPAL (Omni-Purpose Apparatus for LEP), figures 3.1 and 3.2, is one of four experiments on the LEP (Large Electron-Positron) collider at CERN, the highest energy electron-positron colliding beam machine in the world. Since it came on line in 1989 LEP has been running at a centre of mass energy around the Z^0 mass, with beam energies up to 50 GeV. Operating in this environment has allowed many areas of high energy physics to be investigated. These include accurate measurements of the Z^0 line shape parameters, m_Z, Γ_Z and the peak cross section $\sigma_{\rm peak}$, leading to limits on the mass of the top quark and a determination of the number of light neutrino species [20, 21]. Investigations have been carried out in both light and heavy flavour physics [22, 23]. Particle searches have been made, both for expected states such as the top quark [24] and Standard Model Higgs boson [25], and for more exotic particles such as those predicted by supersymmetry [26].

In LEP running so far, all the precision tests of the Standard Model have yielded results compatible with the theoretical predictions, and the top quark and minimal Higgs have remained out of reach. However new limits have been set at LEP for the properties of such particles. Near the end of the century it is hoped that the machine will be upgraded, LEP phase II having a centre of mass energy close to

200 GeV. This new energy window will provide an opportunity for the study of the physics which lies above the W^+W^- threshold. The physics relating to LEP II are described in detail in reference [27].

3.2 The OPAL detector

The OPAL detector is described fully in reference [28] and only an overview is included in this thesis. The experiment consists of a cylinder 7 m in diameter and 7 m in length surrounding the LEP beam pipe and provides excellent acceptance for the products of Z^0 decays over a solid angle of nearly 4π. The apparatus is divided into three main subdetector systems: a central tracking system, within an axial magnetic field, for the measurement of momentum and energy loss of charged tracks, a set of calorimeters for the determination of electromagnetic and hadronic energy flow, and outer chambers for the identification of muons. Also included is a forward detector system situated close to the beam pipe on each side of the central detector, for accurate measurement of the LEP luminosity and the detection of particles which are emitted at small angles with respect to the beam line.

3.2.1 Central tracking system

The OPAL central tracking system comprises a vertex detector for accurate position measurement near the interaction region, a large jet chamber providing position and ionisation energy loss measurements, and an outer layer of chambers for the determination of track end points in z[1]. In 1991 a silicon microvertex detector was installed in the experiment around the beam pipe. The system lies within an axial magnetic field of 0.435 T produced by a warm coil solenoid. Just outside this coil is a set of time of flight detectors which act as a primary trigger and which are also used to distinguish events which do not come from the interaction region.

The jet chamber is designed for efficient recording of jet-like events, giving good

[1] A right-handed coordinate system is used by OPAL, where positive z is along the electron beam direction and r and ϕ are the usual cylindrical polar coordinates.

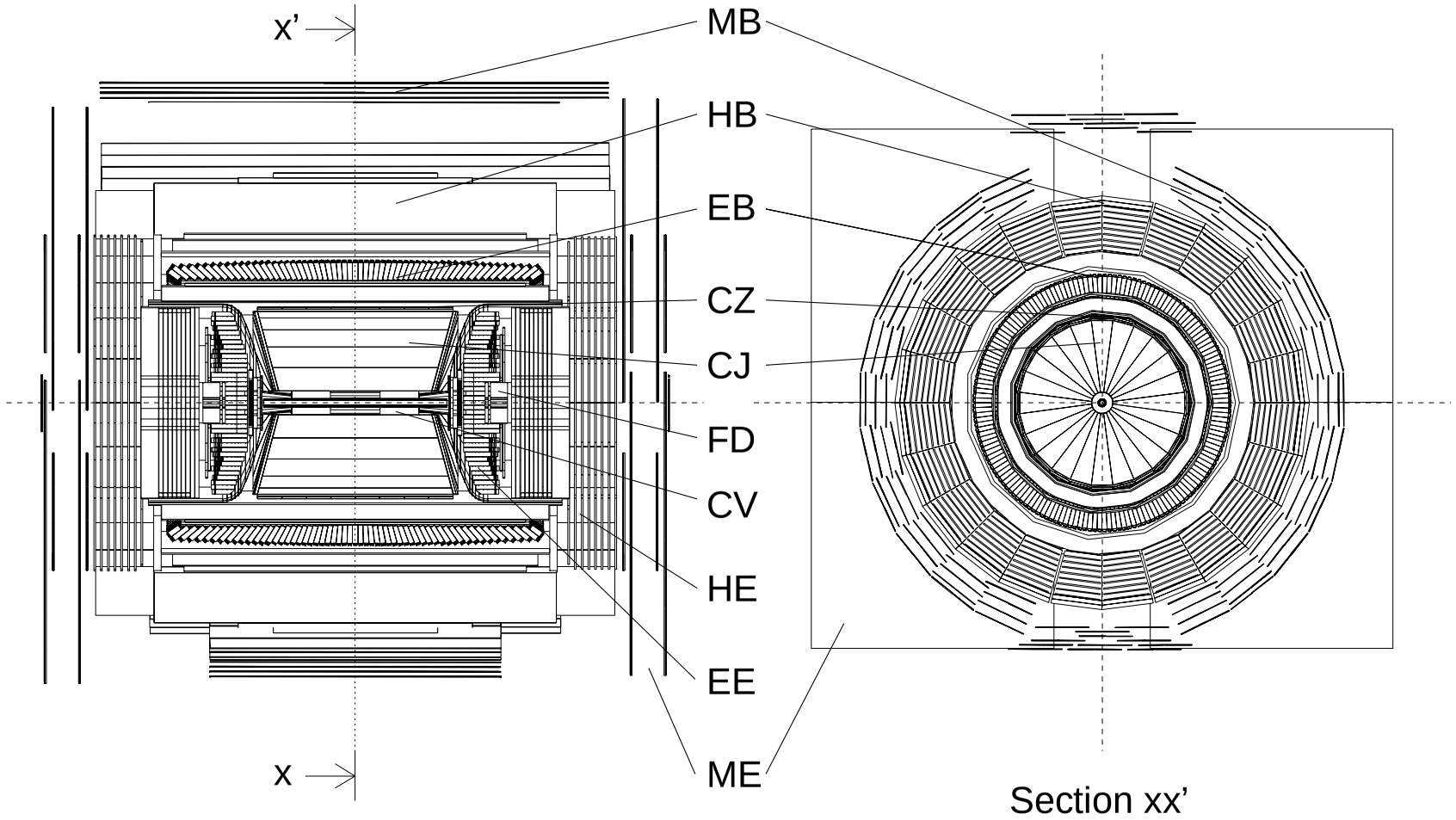

Figure 3.1: Side and end views of the OPAL detector, sectioned to show the main subdetector systems: central vertex chamber, jet chamber and z-chambers (CV, CJ and CZ), electromagnetic calorimeters (EB and EE), hadron calorimeters (HB and HE) and muon chambers (MB and ME). The forward detector modules (FD) can also be seen.

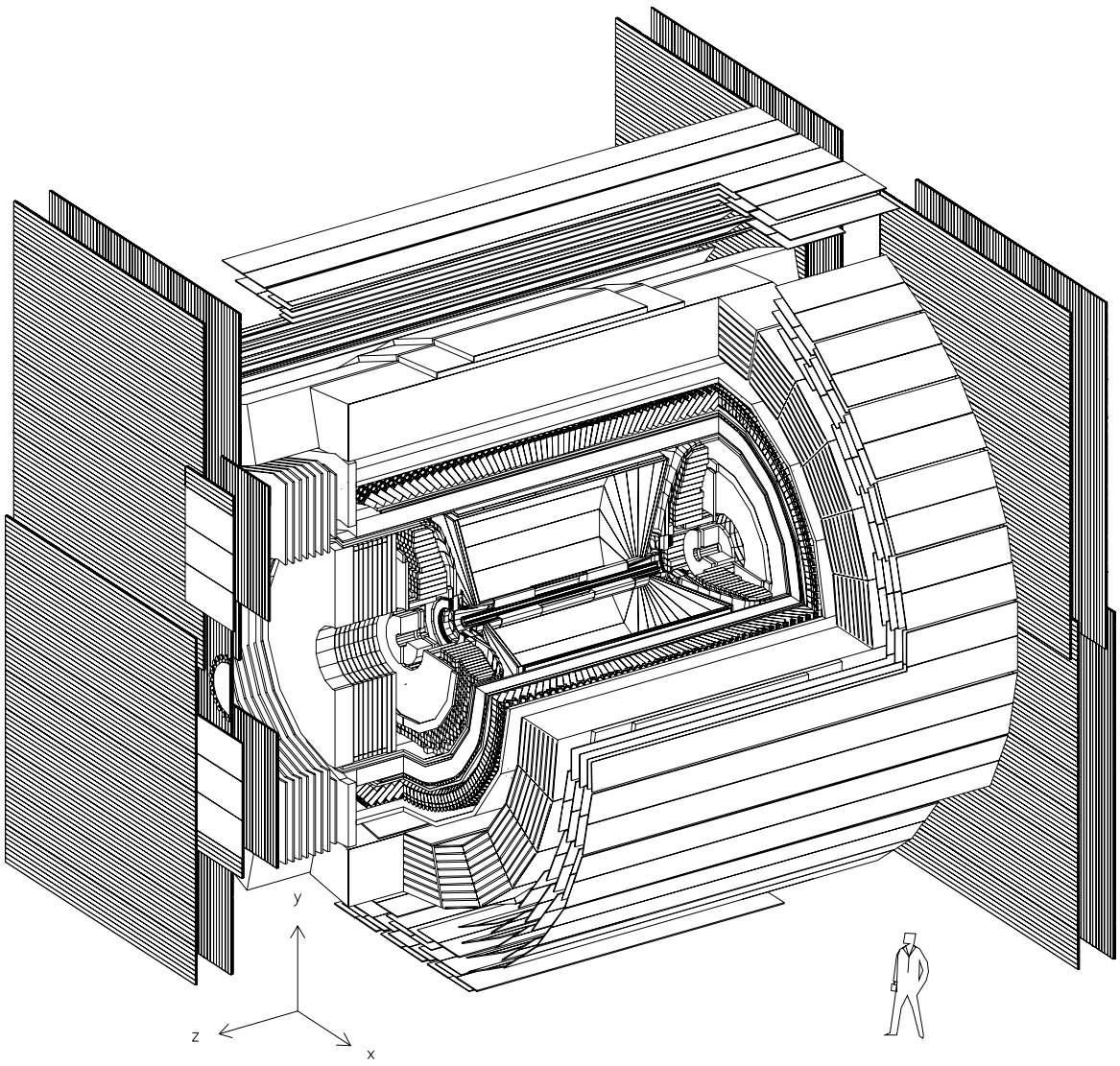

Figure 3.2: A cut-away view of the OPAL detector.

track-track separation down to $\sim$ 3 mm, within a solid angle close to 4π. The chamber contains 24 radial planes of sense and field wires running parallel to the beam pipe. Each radial plane contains 159 anode wires, equally spaced by 10 mm and staggered by ± 100 μm to resolve left-right ambiguities. The average position resolution in the $r-\phi$ plane is 135 μm. Using charge division at each end of the wires, an average z resolution of 6 cm can be achieved. For a well measured track the momentum resolution of the chamber, σ_p/p^2, is 2.2×10^{-3} $(\mathrm{GeV}/c)^{-1}$ [28]. Perhaps more relevant to the analysis in this thesis is the two-particle mass resolution, which typically varies from 2 MeV to 20 MeV depending on the mass and momentum of the reconstructed state. The chamber also measures the ionisation energy loss, $\mathrm{d}E/\mathrm{d}x$, of charged particles traversing the volume. The measurement of this quantity and its implications in particle identification are described in chapter 5. A track with the maximum number of energy loss measurements has a $\mathrm{d}E/\mathrm{d}x$ resolution of 3.5% [4].

The vertex chamber is basically a scaled down jet chamber design, which is positioned within the jet chamber, and centred on the interaction point. The chamber uses both axial and stereo cells and has an average $r\phi$ resolution of 55 μm, and z accuracy, σ_z, of 500 μm for charged particles close to the interaction region [28]. Measurements from the detector are used to determine the position of secondary vertices in $\mathrm{e^+e^-}$ events.

Accurate z measurement of track end points is provided by a layer of z-chambers located outside the jet chamber. These consist of 24 drift chambers, matching the 24 sectors in the jet chamber, subdivided into cells along the z axis. Each cell can record up to six space point measurements. The absolute z resolution of the z chambers is 300 μm [28].

Outside the coil structure is located a set of 160 scintillation counters which make up the time of flight system. As the counters are at a radius of about two metres any cosmic ray muon passing close to the origin will take about 15 ns to traverse the distance. The resolution of the time of flight system on OPAL has been measured to be 460 ps [28], and so it can easily identify background events of this type.

The silicon microvertex detector consists of two layers of silicon microstrips mounted directly on the beam pipe. The inner layer is positioned at a radius of

6.1 cm and the outer layer at a radius of 7.5 cm. The position resolution of the device has been measured to be 5 μm in the $r-\phi$ plane and 13 μm in z [29].

3.2.2 Detector calorimetry

In the OPAL detector two types of calorimeters are employed, an electromagnetic calorimeter, ECAL, for the measurement of electromagnetic showers from electrons and photons, and a hadron calorimeter, HCAL, for the detection of hadronic showers.

Although the main purpose of the electromagnetic calorimeter is to detect and measure the energies of electrons and photons, it can also be used to discriminate between π^0 and photons and, in conjunction with the tracking system, electrons and hadrons.

The ECAL consists of a barrel section and two endcaps, which together cover 98% of the solid angle. The detector is made of lead glass blocks, which produce Čerenkov light, with a total absorption length of 24 X_0. This material was chosen because of its excellent intrinsic energy resolution ($\sigma_E/E \sim 5\%/\sqrt{E}$, E in GeV), spatial resolution, granularity, electron/hadron discrimination and gain stability. The individual blocks are instrumented with shielded, magnetic field tolerant phototubes in the barrel and vacuum photo-triodes in the endcaps.

As the OPAL ECAL lies outside the coil assembly with approximately two radiation lengths of material in front, a presampler consisting of drift chambers in limited streamer mode is used to improve the energy resolution and $\pi^0\gamma$ and electron / hadron discrimination. This is possible because the pulse height in the presampler is directly proportional to the number of charged shower particles produced, and hence the energy deposited in the material in front of the calorimeter. Without material in front of the ECAL the typical energy resolution has been measured to be $\sigma_E/E = 0.2\% + 6.3\%/\sqrt{E}$. Adding the 2.03 X_0 of aluminium in the coil degrades this by a factor of two at 6 GeV, but around 50% of this degradation can be recovered from presampler information [28].

Using the correlated response of both the presampler and calorimeter system, a pion rejection factor of $\sim 10^{-3}$ can be achieved for an electron identification efficiency

of 80 - 90% [28]. Further discrimination can be achieved using the charged particle identification capability of the jet chamber via $\mathrm{d}E/\mathrm{d}x$.

The purpose of the hadron calorimeter is to measure the energy of hadrons emerging from the ECAL. It also assists with the identification of muons by absorbing other particles, giving clean tracks in muon detectors placed outside the HCAL.

In OPAL the HCAL consists of layers of iron instrumented with limited streamer tubes. The iron acts as an absorber material and also provides the return yoke for the magnetic flux from the solenoid. Like the electromagnetic calorimeter it consists of a barrel region and two endcaps. Two pole-tip components are also included to extend the angular coverage of the hadron calorimeter down to the beam line. As there is a high probability of hadronic showers being initiated before the HCAL, overall energy flow is determined by combining signals from both ECAL and HCAL. Using combined signals from the ECAL and HCAL the energy resolution varies from $100\%/\sqrt{E}$ at shower energies less than 15 GeV to $140\%/\sqrt{E}$ at 50 GeV [28].

3.2.3 Muon detection

OPAL's muon identification system, like its calorimeters, is made up of a barrel and two endcap detectors. It is mounted outside the instrumented iron HCAL, forming the outermost part of the detector. The barrel consists of four layers of large area drift chambers with two sense anode wires in each chamber, staggered to resolve left-right ambiguities. Electrons drift in the ϕ direction giving an $r\phi$ resolution of 1.5 mm [28]. The z co-ordinate of a hit is determined by a three stage process involving diamond cathode pads and charge division along the wire, giving an overall z resolution of 2 mm [28].

The endcaps are made up of four layers of limited streamer tubes perpendicular to the beam axis with good overlap with the acceptance of the barrel. The resolution of the endcaps was found to be between 1 mm and 3 mm depending on the position of the readout strips [28].

3.2.4 Forward detector and luminometer

The forward detector is used to determine the LEP luminosity using small angle Bhabha scattering. It is also used to tag two photon events and to increase the angular acceptance of the electromagnetic calorimeter. The detector comprises two identical units positioned at each end of the central jet chamber around the beam pipe. Each unit contains a gamma catcher, two layers of radial drift chambers, a fine luminosity monitor and an electromagnetic calorimeter. The gamma catcher and calorimeter both consist of lead scintillator sandwich. The latter is split into a presampler and main calorimeter and also contains tube chambers for accurate shower position measurement. The energy resolution of the calorimeter is $18\%/\sqrt{E}$, and the shower position can be measured with a typical resolution of 3-4 mm [28].

In 1993 a silicon-tungsten (SiW) luminometer was installed in OPAL as part of the forward detector system. The luminometer consists of two finely segmented, position sensitive SiW calorimeters, placed on each side of the OPAL detector, just in front of the main forward detector units.

3.3 The OPAL online systems

3.3.1 The event trigger

The OPAL trigger system, described fully in [30], is designed to select beam crossings which have a possible e^+e^- interaction, reducing the 45 kHz crossing rate to an event rate of around 1-5 Hz which can be handled by the data acquisition system. The system uses programmable trigger logic and provides a large degree of redundancy for passing physics events while rejecting backgrounds from cosmic rays, beam gas interactions and detector noise.

The central trigger processor receives signals from five separate subdetector trigger systems. The input is subdivided into a '$\theta - \phi$ matrix' of overlapping bins in order to detect spatial coincidences. Of the five trigger inputs, only three are important for the detection of multihadronic events :

- The track trigger is provided by a dedicated hardware processor which uses information from the central detectors to find tracks which originate from the interaction region. Signals from three sets of twelve adjacent sense wires in each of the 24 jet chamber sectors and the twelve axial sense wires in each sector of the vertex chamber are combined. Tracks are identified by looking for coincidences in the $r - z$ plane between hits from the four wire groups, both within a single sector and between two adjacent sectors (to detect tracks which cross sector boundaries).

- For the time of flight trigger the 160 individual scintillation counters are combined into 24 overlapping ϕ bins. A trigger signal is produced in one of these bins if both ends of a counter have fired within 50 ns of each other, and within 50 ns of the arrival time of a particle from the interaction point.

- In the electromagnetic calorimeter, analogue energy sums are calculated for 144 $\theta - \phi$ cells. Twenty four ϕ segments are included which match as closely as possible those of the track trigger. Cells in θ are provided by both the barrel and endcap electromagnetic calorimeters. Trigger signals are also produced based on the total summed energy in the barrel and each of the two endcaps.

The other trigger inputs are provided by the barrel and endcap muon chambers and the two forward detector units.

3.3.2 Event readout and processing

Each of the subdetector systems contain their own data acquisition electronics. When a trigger is received, data are read out from the subdetectors and processed locally before being sent to the central 'event builder' where the data are concatenated into a single event record. This record is fed to the 'filter' [31] where the data are packed and the trigger logic is checked. Finally the data are processed by the OPAL reconstruction software, ROPE. This program reconstructs the tracks and energy clusters using the raw data and information from the OPAL calibration database, and produces a summary of the most important information in the event. This summary is written to permanent storage together with the raw data. As the reconstruction software is constantly updated and improved, the data can be passed

through the final processing stage offline. The ROPE program can also be used to read the data for analysis.

3.4 Detector simulation : GOPAL

Events produced using Monte Carlo generators can be processed using the detector simulation program GOPAL [32] which uses the GEANT3 package [33]. In the GEANT framework the OPAL detector is described in terms of a set of objects called volumes. Each volume contains detailed information about the geometry and material makeup of a section of the detector.

The generated particles in each event are tracked though the volumes, and physics processes such as multiple scattering, particle interactions and decays are simulated using tools provided by GEANT. In each of the detector volumes, hits and clusters are generated and effects such as detector response and efficiency are included. Finally, after all the tracking is complete the simulated signals are 'digitised' producing raw data equivalent to that from the real experiment. As the full simulation of events is a very time consuming process, GOPAL also provides an alternative mode of operation where only coarse tracking is performed and the detector response is simulated by smearing out the tracks with algorithms which include resolutions and efficiencies measured from the real apparatus.

The simulated raw data produced by GOPAL can be analysed using the OPAL reconstruction software in exactly the same manner as the data from the detector.

Chapter 4

Data selection

4.1 The selection of multihadronic events

Multihadronic events are selected from OPAL data using standard criteria described in [21]. The selection is based on both the charged tracks reconstructed in the central detector and the energy deposited in the electromagnetic calorimeter. Tracks are required to have at least 20 space point measurements and a point of closest approach within 40 cm of the interaction point in z and 2 cm in the $r-\phi$ plane. The transverse momentum of each track is required to be greater than 0.05 GeV/c. Clusters in the barrel region of the electromagnetic calorimeter are required to have an energy of at least 100 MeV and those in the endcaps at least 200 MeV. An event is defined as a multihadron candidate if the following criteria are satisfied : at least 5 tracks and 7 clusters pass the above cuts, the total energy deposited in the calorimeter is at least 10% of the centre of mass energy of the event and the energy imbalance along the beam direction, $R_{\rm imbal}$, is less than 0.65. The latter quantity is defined by

$$R_{\rm imbal} = \left|\sum (E_{\rm clus} \cos\theta_{\rm clus})\right| / \sum E_{\rm clus} \ , \tag{4.1}$$

where $E_{\rm clus}$ is the energy and $\theta_{\rm clus}$ is the polar angle of the cluster.

The requirements for tracks and clusters reduce the contamination from lepton pair events ($e^+e^- \rightarrow l^+l^-$). Demanding a minimum total visible energy removes

two-photon events, and the energy balance requirement removes background events such as interactions between the $e^{\pm}$ beams and the gas in the beam-pipe or the beam-pipe walls. It also reduces the background from cosmic rays which enter the detector through the endcap region and so cannot be detected using the time of flight system. The acceptance for multihadronic events selected using this procedure has been determined to be 98.4% [21].

Between 1990 and 1992 OPAL recorded 1.2 million events which satisfied the multihadron criteria. This sample is the basis for the analysis presented in this thesis.

4.2 The Monte Carlo event samples

Approximately one million hadronic events generated by the Monte Carlo program JETSET version 7.3 [7] were used in the analysis. The parameters of the JETSET model had been tuned [34] so that the program reproduced many global features of multihadronic events as observed at LEP. The events were passed through a full simulation of the OPAL detector [32] as well as the event reconstruction software and finally subjected to the same selection process as for the real data.

In addition to this JETSET Monte Carlo sample, 140k fully simulated events were taken from Monte Carlo based on HERWIG version 5.5 [11]. This sample was used to check for systematic effects which may arise from the JETSET model of fragmentation and to determine the experimental acceptance for the $K_2^*(1430)^0$ analysis.

4.3 Further event and track quality cuts

In addition to the selection outlined above, the events used in the analysis were subject to further requirements designed to isolate a sample of multihadronic events which were both well measured and could be simulated by the Monte Carlo programs.

For every charged track in each event in the sample the following quality cuts were applied :

- At least 20 space point measurements in the jet chamber were used to reconstruct the track.
- The point of closest approach of the reconstructed track was within 40 cm of the interaction point in z and 5 cm in the $r - \phi$ plane.
- The radius of the first recorded space point was less than 75 cm.
- The polar angle, θ, of the track was between 21.6° and 158.4°.
- The transverse momentum, p_T, of the track was greater than 0.15 GeV/c.

Figure 4.1 shows the distributions of selected charged track multiplicities, both for data and for the JETSET event sample. The agreement between the two indicates that the Monte Carlo generator together with the detector simulation program produces a good and reliable simulation of the kinematics of recorded OPAL events.

If at least five tracks passed the cuts then the event was tested for energy and momentum balance. The event was rejected if the magnitude of the total reconstructed momentum vector of the selected tracks was greater than 40% of the centre of mass energy, or if the total visible energy summed over all charged tracks (assuming all tracks to be pions) was less than 20% of the total available. The distributions of visible energy for the data and JETSET Monte Carlo samples are shown in figure 4.2. Although the distributions are only broadly in agreement above the cut value of 0.2 they agree well in the region below, indicating that the efficiency of the cut is the same for data and Monte Carlo.

For the subsequent inclusive meson analyses, only those tracks with $p > 0.25$ GeV/c, $|\cos\theta| \leq 0.72$ and at least one recorded z space point in the z-chambers were used. After all the cuts, 925453 events were left from the original multihadronic data sample, with an average of 11.54 selected tracks per event.

To correct for shortcomings in the simulation of track matching between the jet chamber and z-chambers in the central tracking system, a weight was assigned to

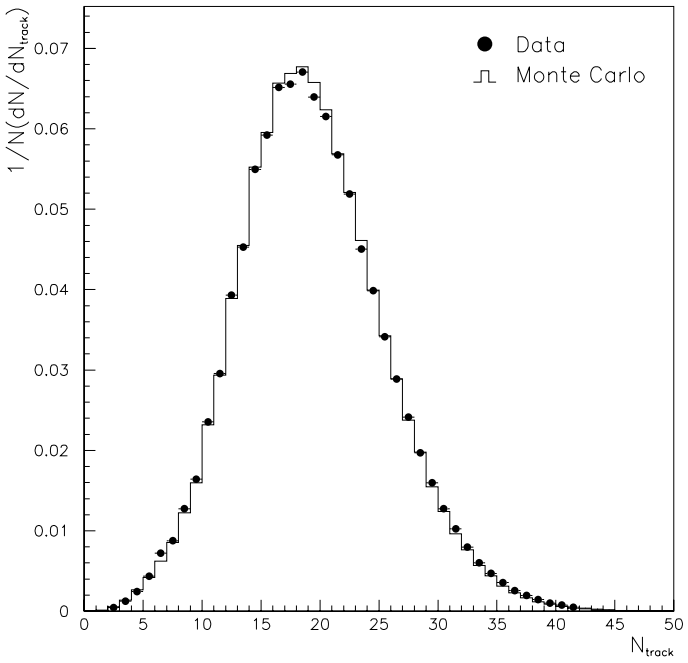

Figure 4.1: The distribution of charged track multiplicity for the data and JETSET events samples.

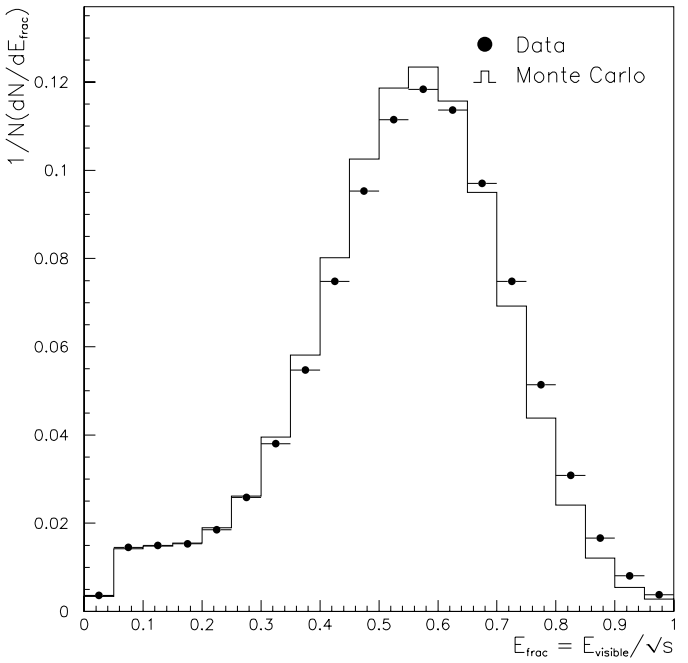

Figure 4.2: The distribution of the ratio of visible charged track energy (assuming all tracks to be pions) to the centre of mass energy, for the data and JETSET event samples.

each of the selected Monte Carlo tracks. These weights were based on a study in both data and Monte Carlo of the distribution of transverse momentum and polar angle of tracks with at least one point in z measured by the z-chambers. Figure 4.3 shows a histogram of the weights applied to tracks with momentum less than 0.5 GeV/c. The weights varied between 0.94 and 1.08, with a mean value of 1.01. The overall uncertainty in these weights, which amounted to 0.8% was taken into account in the final evaluation of systematic uncertainties in the inclusive meson analysis. After weighting, the mean track multiplicity for the JETSET event sample was 11.61 weighted selected tracks per event.

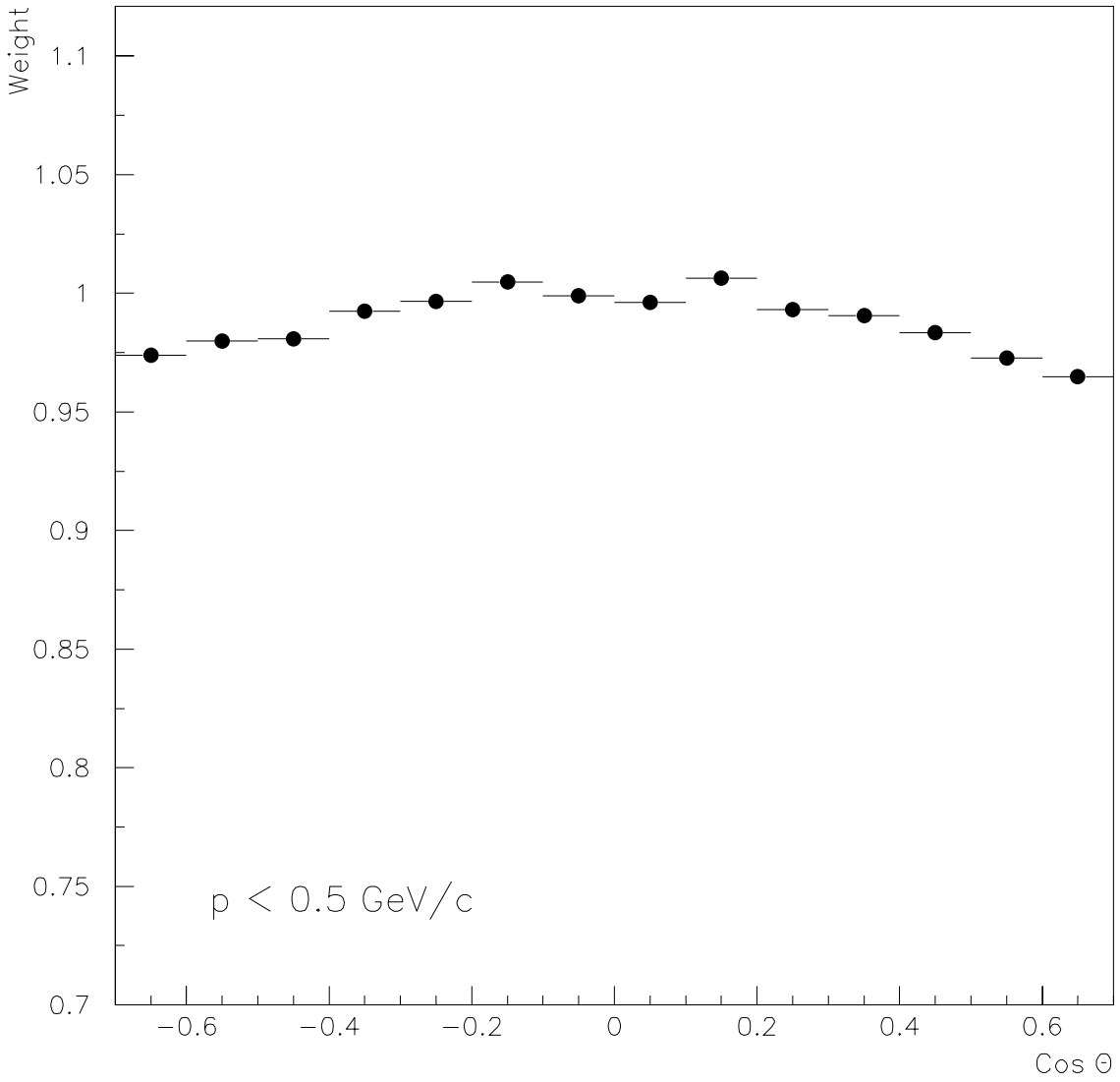

Figure 4.3: Example of the weights applied to tracks to account for the difference in track matching between the jet chamber and z-chambers in real and simulated data .

Chapter 5

Particle identification and mass spectra

5.1 Ionisation loss and particle identification

As charged particles travel through matter they can lose energy due to interactions with atoms, either by excitation or ionisation. This is usually called ionisation loss. Although the interactions depend on the structure of the atoms in question, it is possible to make approximations for the rate of energy loss with distance, $\mathrm{d}E/\mathrm{d}x$, by neglecting much of the fine structure. One such approximation derived by Bethe [35] for a particle with charge Q and velocity β is written :

$$\frac{dE}{dx} = -\xi\frac{Q^2}{\beta^2}\left\{\ln\left(\frac{2m_e c^2\eta}{I^2}\right) + \ln\beta^2\gamma^2 - \beta^2 - \delta(\beta)\right\} \ , \tag{5.1}$$

where

$$\xi = \nu.\frac{2\pi n_e e^4}{m_e c^2} \ . \tag{5.2}$$

In this formula n_e is the electron density of the gas, I is the mean ionisation energy, and η is the maximum energy transfer per collision. The factor ν in the expression for ξ is the fraction of electrons able to interact with the particle; from [36] $\nu \approx 0.9$. Ionisation loss is usually measured in units of keV/cm. The parameter $\delta(\beta)$ is

normally determined by fitting the curve to data; physically it depends on the density and other physical properties of the material the particle is moving through.

If $\mathrm{d}E/\mathrm{d}x$ is plotted against the product of the particle velocity β and the Lorentz factor γ (figure 5.1) it shows a characteristic shape. At low velocities $\mathrm{d}E/\mathrm{d}x$ falls like $1/\beta^2$ to a minimum at $\beta\gamma \sim 4$. Above this is a 'relativistic rise region' where the ionisation loss increases logarithmically until it saturates (the 'Fermi plateau'). The onset of the saturation after the relativistic rise region is governed by the factor $\delta(\beta)$ in equation 5.1. A particle whose momentum corresponds to the minimum in the curve is called a minimum ionising particle.

If the ionisation loss of a particle is plotted against its momentum, the general shape of the curve is the same but the position of the curve is determined by the identity of the particle. For example, figure 5.2 shows the theoretical curves for e, π, K and p. By measuring the ionisation loss of a particle together with its momentum, the mass of the particle can be determined, and hence its identity deduced. For particles with relatively low momenta (less than $\sim$ 2 GeV/c) the curves are well separated except where they cross over; however in the relativistic rise region the difference in energy loss between particle types is relatively small. For example, at a momentum of 10 GeV/c the separation in mean $\mathrm{d}E/\mathrm{d}x$ between electrons and pions is around 10%. In this region both the resolution of the ionisation loss measurement and the systematic errors involved must be kept small in order to achieve a useful level of particle identification.

5.1.1 The jet chamber and $\mathrm{d}E/\mathrm{d}x$ measurement

The measurement of ionisation loss in the OPAL jet chamber is described in detail in reference [37]. The stability of the measurements is ensured by tight requirements on detector parameters such as gas density, high voltage and electronics gain. In order to achieve the best possible resolution for $\mathrm{d}E/\mathrm{d}x$ measurements the online signals from the chamber are subject to quality cuts. Hits are only used which are assigned to the final track fit (used for momentum measurement) and have a distance to the sense wire plane of at least 2 mm. Due to the large amount of activity in the jet chamber in multihadronic events, it is relatively common to find

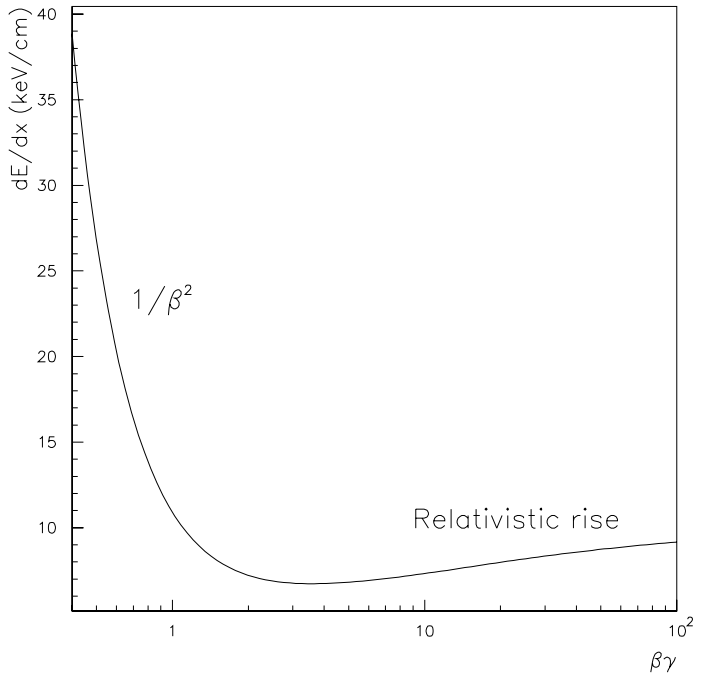

Figure 5.1: Plot, for a typical detector, of the variation of ionisation loss ($\mathrm{d}E/\mathrm{d}x$) with the product of the particle velocity and the Lorentz factor ($\beta\gamma$).

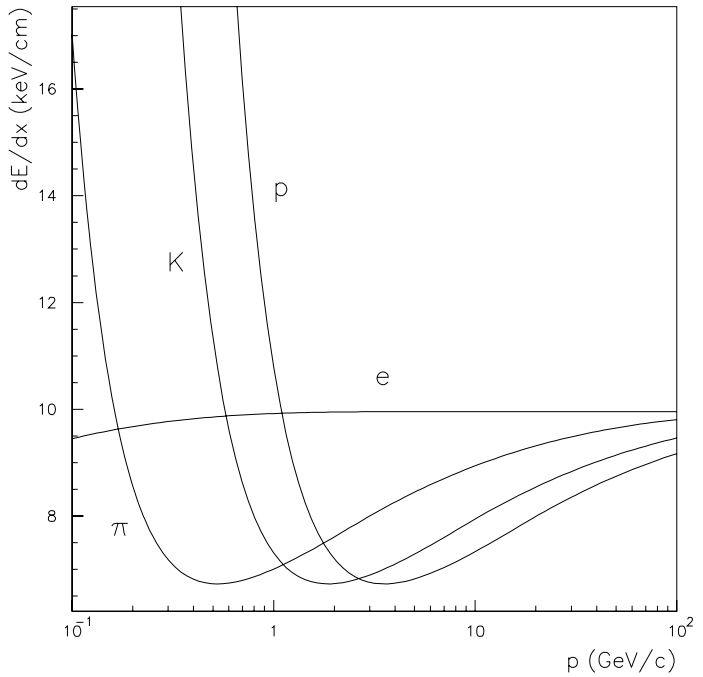

Figure 5.2: Plot, for a typical detector, of the variation of ionisation loss with momentum for charged electrons, pions, kaons and protons.

hits with only a small spatial separation between them. If two such hits are closer together than the double hit resolution of the chamber ($\sim$ 3 mm) then they are no longer resolved and only a single hit is recorded. The hits from parts of two tracks which are separated by less than 3 mm are therefore not included in the ionisation loss determination. For tracks which cross sector boundaries the hits closest to the boundary on each side are rejected if they lie closer than 1 cm to the interface. These quality cuts remove $\sim$ 7.5% of the hits per track for isolated tracks and $\sim$ 35% of the hits in multihadronic events.

Various corrections are applied to the charge measurements to take into account known features of the jet chamber and the associated electronics. These corrections are described in detail in [37]. The energy loss for each remaining hit is calculated by integrating the charge on the wire with time over a period of 200 ns.

The individual $\mathrm{d}E/\mathrm{d}x$ measurements from each wire for a track are analysed using a technique called truncated mean. The distribution of energy loss for a relativistic particle travelling through a 'thin' absorber such as the gas in the jet chamber is described by a Landau distribution, which has a long tail at high values of ionisation loss. This is due to the energy loss occurring from a small number of collisions, resulting in large fluctuations, and hence a wide overall distribution. This tail is cut so that only the lower 70% of the sample remains and the final $\mathrm{d}E/\mathrm{d}x$ value for the track is taken as the mean of the truncated distribution.

The precision of a $\mathrm{d}E/\mathrm{d}x$ measurement obviously then depends on the number of recorded hits for a track. In the OPAL jet chamber each of the 24 radial planes contains 159 sense anodes. This means that a track can have a maximum of 159 hits if it travels out of the barrel of the chamber. Tracks which travel out of the ends of the chamber will have fewer hits and so the recorded $\mathrm{d}E/\mathrm{d}x$ measurement will be less reliable. To reduce this problem and to get a large acceptance angle in the jet chamber the wires are strung between conical endplates.

For minimum ionising pions in multihadronic events, the $\mathrm{d}E/\mathrm{d}x$ resolution of the chamber has been measured [4] to be 3.5% if the maximum number of measurements per track is demanded. Figure 5.3 shows the distribution of $\mathrm{d}E/\mathrm{d}x$ versus particle momentum for a sample of well measured tracks (selected as described in chapter 4), with a minimum of one hundred measurements of energy loss per track,

in OPAL multihadronic data. The bands for electrons, muons, pions, kaons, and protons are all clearly visible on the plot, illustrating the quality of OPAL energy loss measurements.

5.1.2 Parametrisation of ionisation loss

A parametrisation of the energy loss for a given particle mass and momentum is vital for physics analyses which use $\mathrm{d}E/\mathrm{d}x$, both for particle identification and as the basis of Monte Carlo simulation of ionisation loss. In OPAL a quasi-empirical energy loss function is used, based on the Bethe-Bloch formula (equation 5.1), the values of the parameters ξ, η and $\delta(\beta)$ being determined from the data. A full description of the energy loss function is given in reference [37].

The energy loss of particles in Monte Carlo data is simulated in GOPAL [32]. As the particles are tracked through the jet chamber volume the measured ionisation loss for each hit is determined using the Bethe-Bloch parametrisation and smeared according to an experimentally determined Landau distribution. At the end of the tracking stage of the simulation the individual measurements of energy loss for each track are collected together and analysed using the truncated mean approach. Various detector effects are also included in the simulation so that the Monte Carlo distribution for ionisation loss with momentum reproduces all the detailed features of the real data, including the overall measured $\mathrm{d}E/\mathrm{d}x$ resolution.

A useful set of quantities calculated from the measured $\mathrm{d}E/\mathrm{d}x$ using the energy loss function are the $\mathrm{d}E/\mathrm{d}x$ weights or χ^2 probabilities for the charged particles which can be detected in the jet chamber: e, μ, π, K and p. For a track with momentum p and ionisation loss ϵ the following χ^2 is formed :

$$\chi^2(q) = \left(\frac{\epsilon - < \epsilon(q,m) >}{\sigma_\epsilon}\right)^2 + \left(\frac{p-q}{\sigma_p}\right)^2 , \tag{5.3}$$

where σ_ϵ and σ_p are the uncertainties on the measurements and $< \epsilon(q,m) >$ is the value of the parametrised mean energy loss function for a particle with momentum q and mass m. This χ^2 is minimised for each of the five particle masses by varying the value of q. The χ^2 probabilities for the particle types are calculated from the minima (χ^2_0) by integrating the normalised χ^2 distribution for one degree of freedom

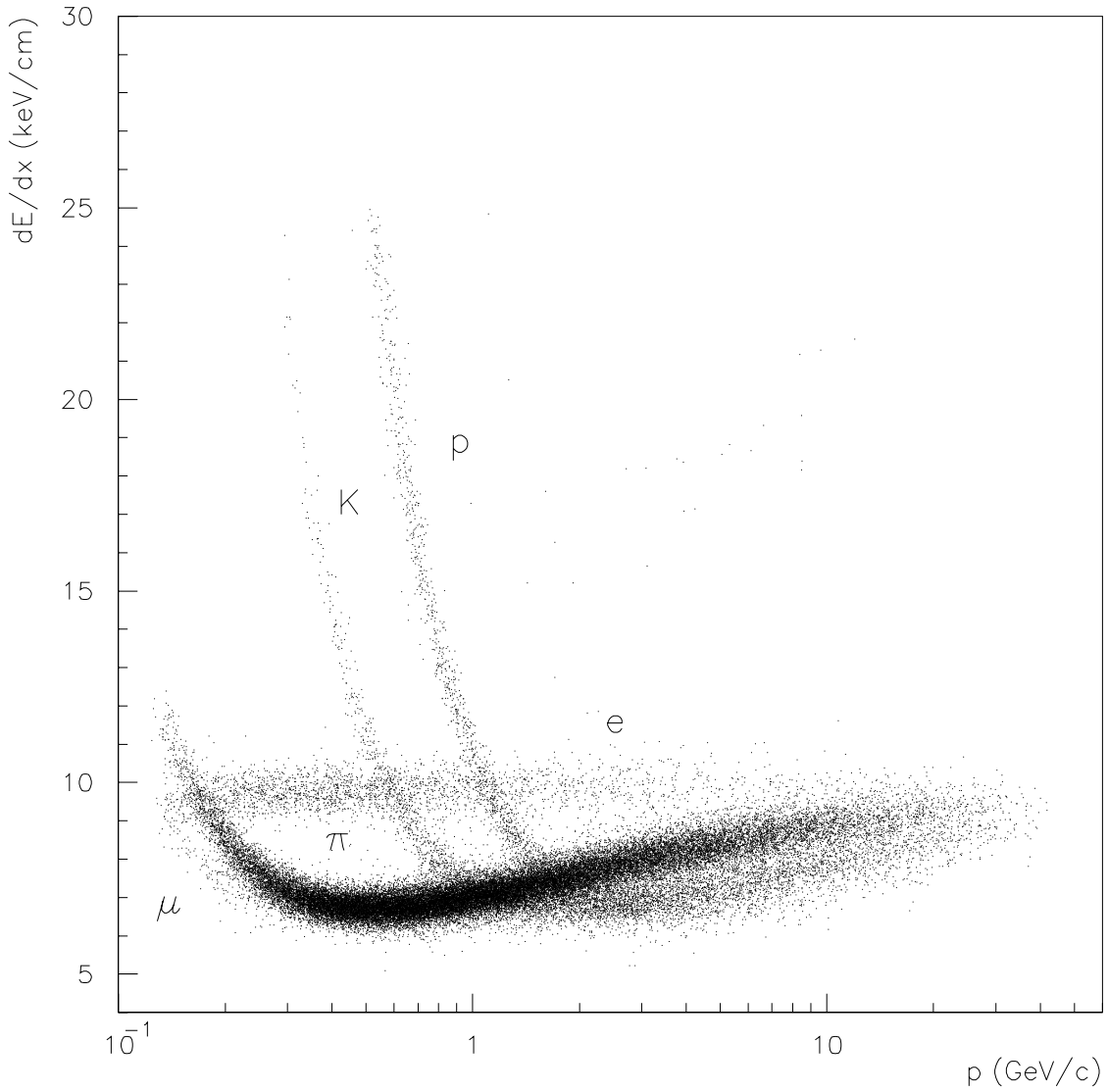

Figure 5.3: The distribution of ionisation energy loss ($\mathrm{d}E/\mathrm{d}x$) with particle momentum for a sample of selected well measured tracks in OPAL multihadronic data.

$P_1(z)$:

$$\text{prob}\,(\chi_0^2) = \int_{\chi_0^2}^{\infty} P_1(z)\,dz \ . \tag{5.4}$$

The general definition of the χ^2 distribution can be found in reference [38]. The main use of these 'weights' is in particle identification, as the χ^2 probability is a good indication of the compatibility of a $\mathrm{d}E/\mathrm{d}x$ measurement with a candidate particle type.

5.1.3 The particle identification algorithm

The particle identification algorithm used in the present analysis was based on that used in the original OPAL vector meson study [1]. Each track was required to have at least 20 separate points of $\mathrm{d}E/\mathrm{d}x$ measurement in the central tracking chamber and ionisation loss less than 40 keV/cm, in order to remove tracks that would not be well simulated. Given that the separation between the bands in the $\mathrm{d}E/\mathrm{d}x$ distribution depends strongly on momentum [37] it was not possible to identify kaons across the entire momentum range. A study of this effect was carried out in [1] and the same limits were applied in the present analysis: no tracks were identified as kaons between 0.8 and 2.0 GeV/c.

For a given track, a $\mathrm{d}E/\mathrm{d}x$ weight (χ^2 probability) was calculated as described above, for each of the four candidate particle types (electrons, pions, kaons and protons). Muon identification was not possible as the muon and pion bands in the $\mathrm{d}E/\mathrm{d}x$ distribution are poorly separated for particles with momenta above $\sim$ 0.2 GeV/c. If at least one of the four weights was above 0.05 then the track was assigned to the particle type corresponding to the largest χ^2 probability. Using this procedure on the real data, 10.23 tracks per event on average were assigned a particle type. The difference in mean track multiplicity between real data and the weighted JETSET Monte Carlo sample was only 0.6% for all tracks and 0.3% for those tracks with a particle type assigned to them from the identification process.

Although candidates for electrons, pions, kaons and protons were selected from the tracks in each event, only kaon identification was used in the inclusive meson analysis. The efficiency of kaon identification and the pion to kaon misidentification probability as a function of particle momentum for the JETSET Monte Carlo event

sample is shown in figure 5.4. As expected, the efficiency is high for low momentum kaons, but drops down to ~40% at around 0.6 GeV/c where the kaon band crosses the electron band (figure 5.3). For kaons in the relativistic rise region the identification efficiency drops with increasing particle momentum as the separation between bands decreases. Over the whole momentum region the probability of pions being misidentified as kaons is small. Below 0.5 GeV/c where the bands are well separated it is virtually zero, but it increases near the border of the region where the kaon/pion bands cross, and continues to increase in the region above 2 GeV/c, to reach a maximum at around 15%. These probability distributions were used in the $K^*(892)^0$ analysis to determine the effect of the $\rho(770)^0 \rightarrow \pi^+\pi^-$ background in the $K\pi$ mass spectra.

The efficiency of kaon identification was also determined directly from the real data, using the $\phi(1020)$ signal in the K^+K^- invariant mass spectra, as described later in chapter 6.

5.2 Two-particle invariant mass spectra

For each event in the sample of multihadronic data, the KK two-particle invariant mass was calculated for all two track combinations where both tracks were identified as kaons. In order to minimise systematic effects arising from pion identification, the $K\pi$ invariant mass was constructed for each kaon candidate combined with all the other tracks in the event. The invariant mass spectra were formed in various ranges of the scaled energy variable x_E defined by

$$x_E = E/E_{\rm beam} \ , \tag{5.5}$$

where E is the combined energy of the two particles and $E_{\rm beam}$ is the LEP beam energy for the event. In the analysis of the KK spectra six regions of x_E were considered, while the data were split into 10 regions for the $K\pi$ plots.

Separate histograms were used to record neutral and doubly charged combinations. Figures 5.5 and 5.6 show the resultant mass spectra for KK and $K\pi$ combinations, integrated over x_E. The plots from the JETSET Monte Carlo event sample

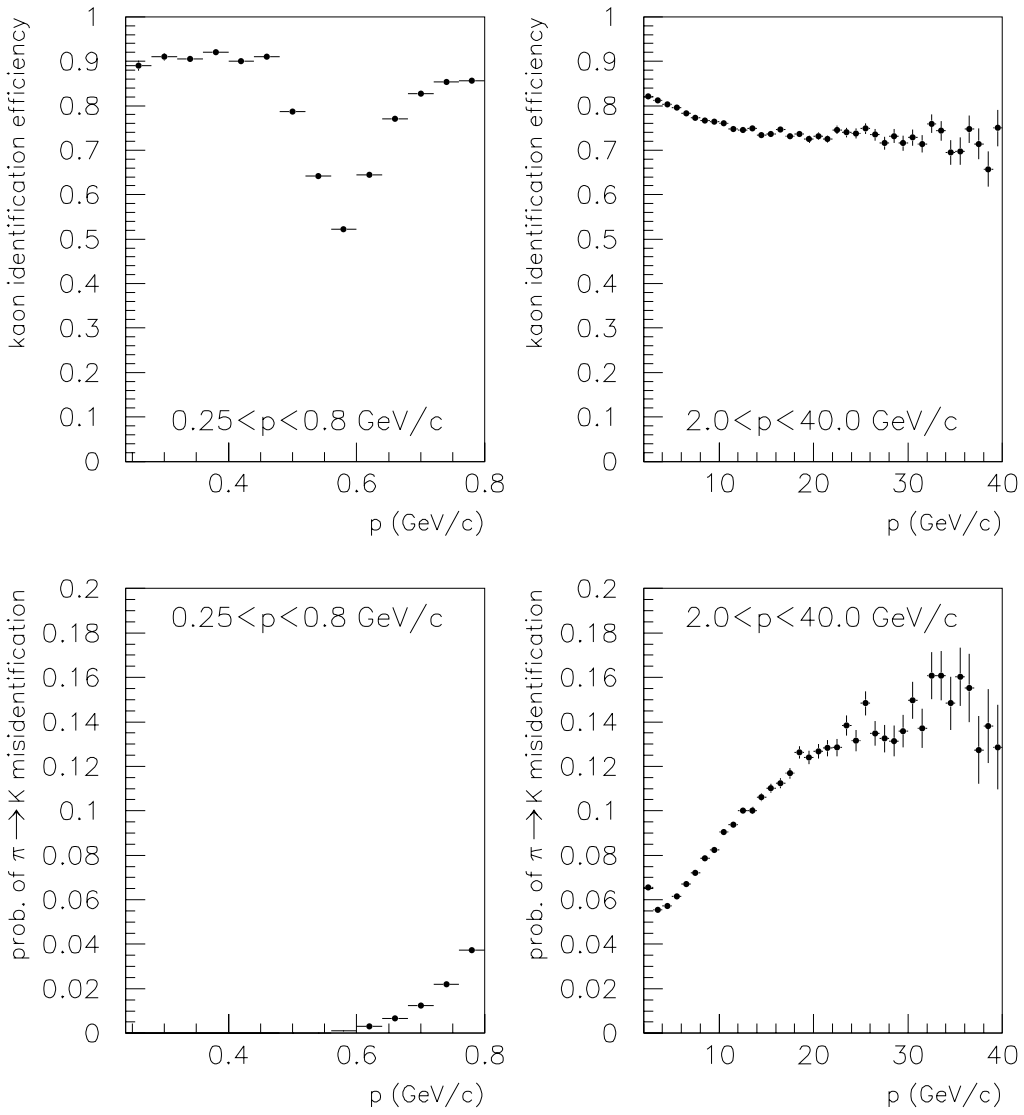

Figure 5.4: The variation of kaon identification efficiency and pion to kaon misidentification probability with particle momentum, for tracks from the JETSET Monte Carlo event sample. No kaon identification was attempted for tracks with momenta between 0.8 and 2.0 GeV/c, due to the cross-over region of the kaon and pion bands in the dE/dx distribution.

have been normalised to the same total number of selected Z^0 decay events as the data, in order to make a direct comparison.

In the KK spectra the $\phi(1020)$ signal is clearly visible in the neutral combinations. Apart from the intensity of the signal, the Monte Carlo simulates the shape of the data well although there are small discrepancies in both plots just above threshold. This may be due partly to the effects of Bose-Einstein correlations [39, 1] which are not simulated in the Monte Carlo.

In the Kπ mass spectra the signal to background ratio for the $K^*(892)^0$ is much smaller than for the $\phi(1020)$ due mainly to the large excess of combinatorial Kπ pairs as opposed to KK combinations. In order to enhance the signal, the spectra for doubly charged Kπ combinations were subtracted from those for neutral combinations on a bin by bin basis; the resultant 'subtracted' plot is shown in figure 5.7.

As the simulated events contain a record of the origin of each measured track it is possible to break down the Monte Carlo invariant mass spectra into their constituent parts. The main features of the KK and Kπ mass spectra are shown in figures 5.8 and 5.9. These consist of the signal, the combinatorial background and backgrounds from the decay of other states, where one or both of the decay particles have been misidentified, resulting in a distorted signal from the miscalculated invariant mass. One particularly important background of this type is from the decay of the $\rho(770)^0$ to two charged pions. According to the Monte Carlo, the reflection lies under the $K^*(892)^0$ peak so that a good understanding of this background is important in the analysis.

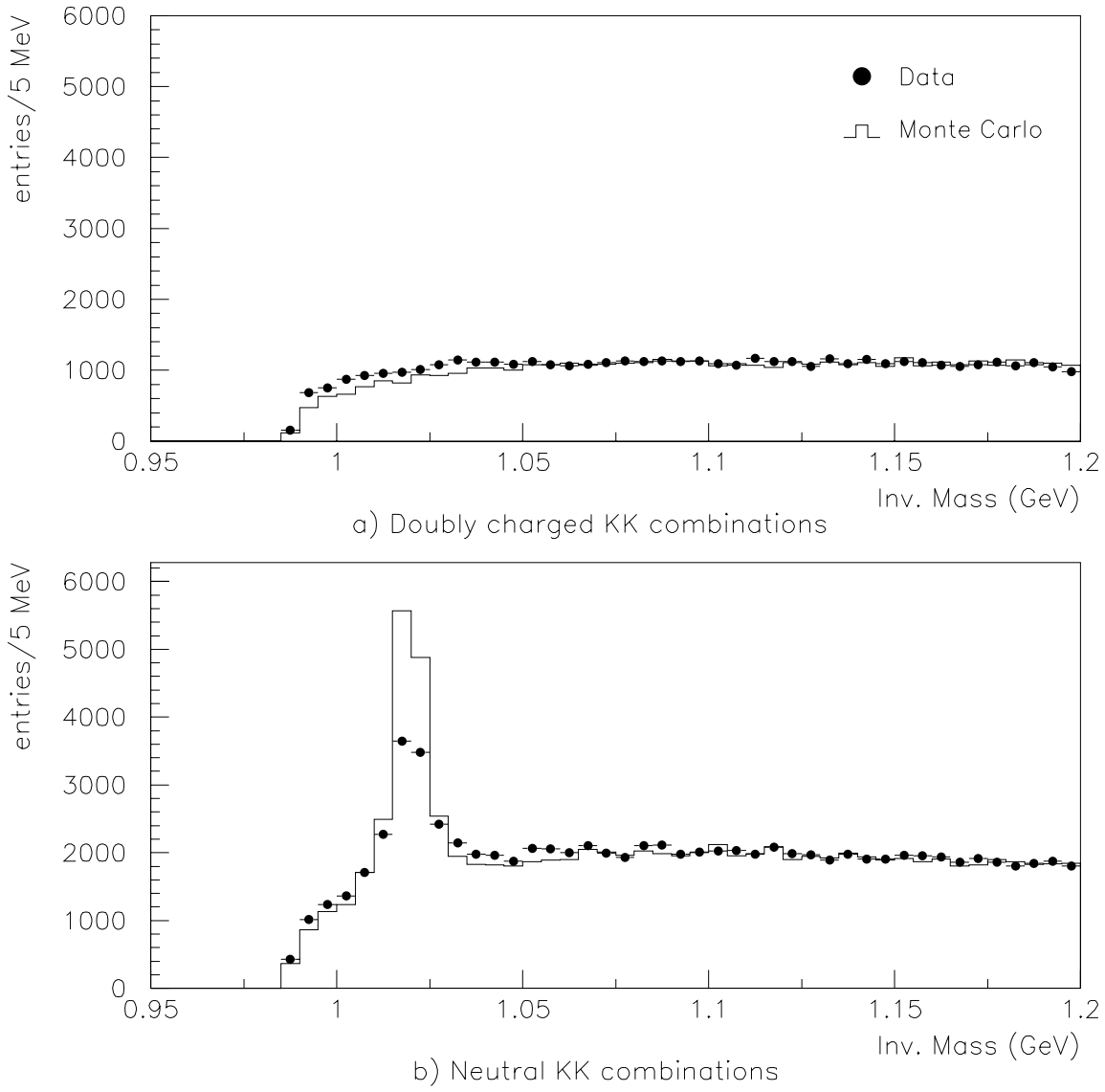

Figure 5.5: Invariant mass spectra for selected KK combinations.

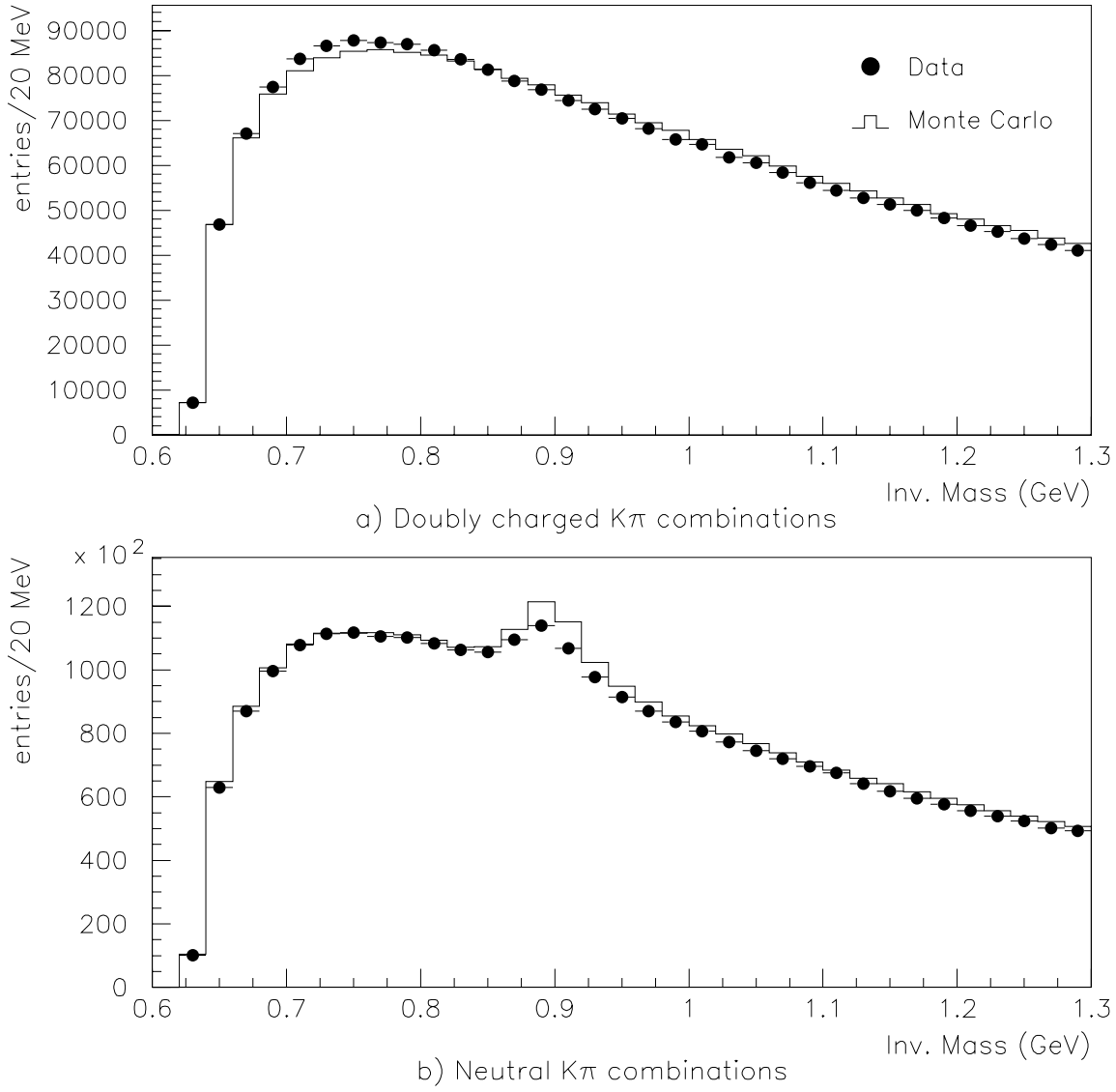

Figure 5.6: Invariant mass spectra for selected Kπ combinations.

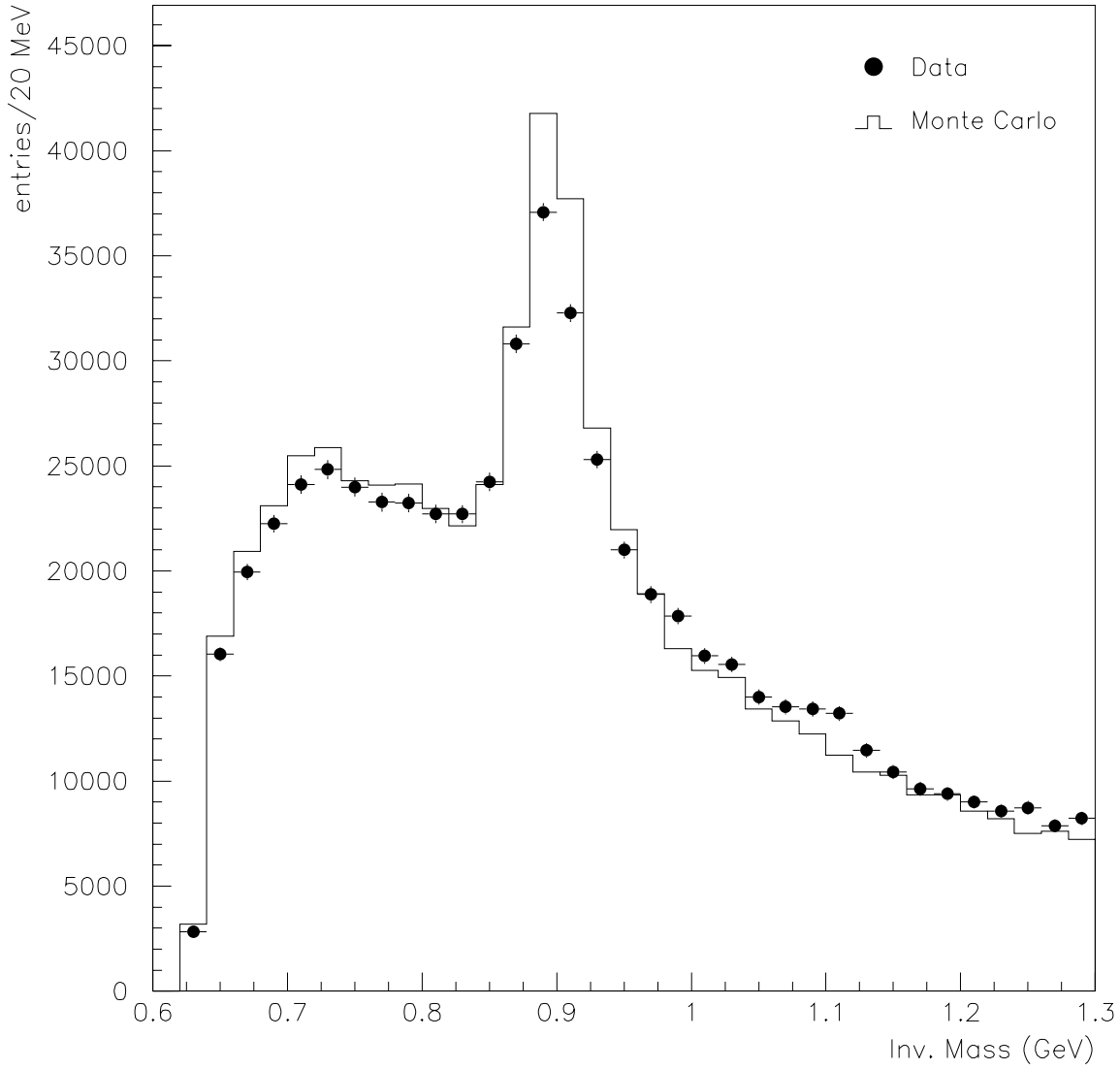

Figure 5.7: 'Subtracted' Invariant mass spectra for selected Kπ combinations.

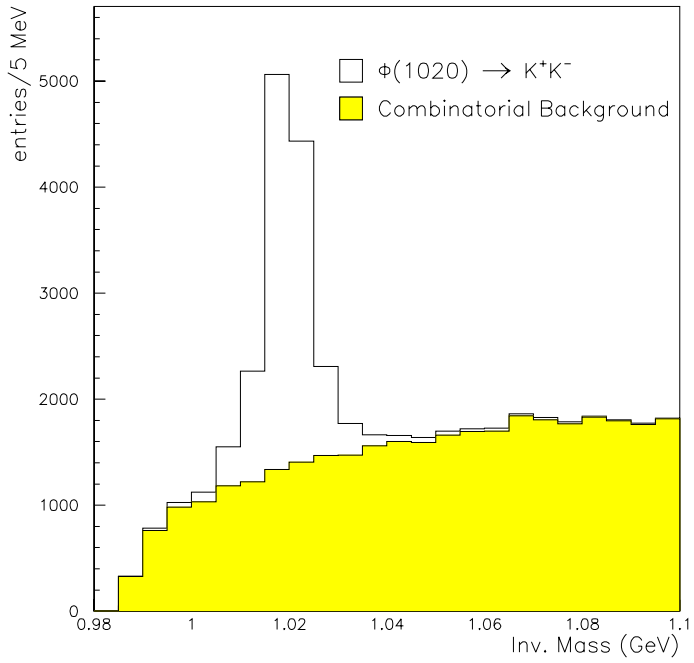

Figure 5.8: Composition of the JETSET Monte Carlo K^+K^- mass spectrum.

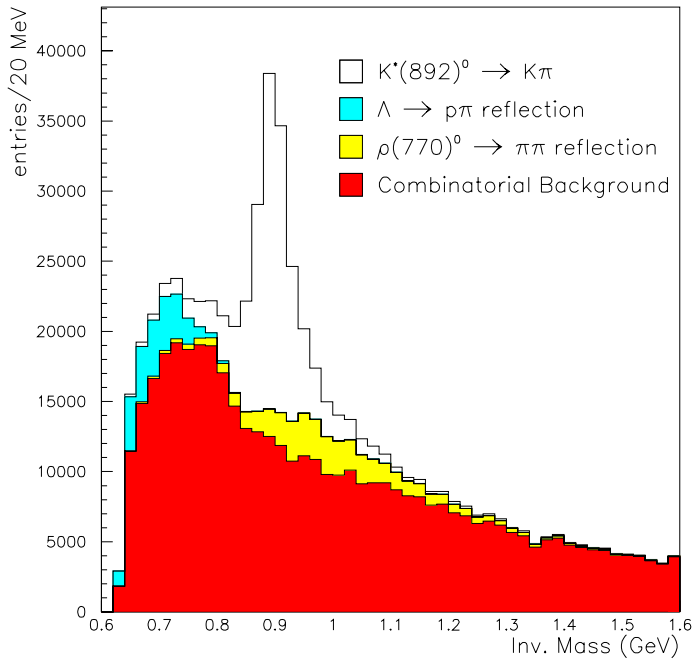

Figure 5.9: Composition of the 'subtracted' JETSET Monte Carlo $K\pi$ mass spectrum.

Chapter 6

Kaon identification efficiency

As the JETSET Monte Carlo sample is used extensively in the analysis it is important to check the consistency of particle identification efficiencies between the simulated data and those measured from the detector. To this end, efficiencies for kaon identification have been measured directly from the invariant mass spectra in the real data and compared to values deduced from the Monte Carlo simulation. The results from this study have been used as corrections to the inclusive rate measurements for the vector mesons $\phi(1020)$ and $\mathrm{K}^*(892)^0$.

6.1 Efficiency determination

For a sample of events which includes N decays of ϕ mesons to charged kaons, define F_n as the fraction of decays which remain after the requirement that exactly n ($n = 0$, 1 or 2) of the decay products have been identified as kaons using $\mathrm{d}E/\mathrm{d}x$, i.e.

$$F_n = \frac{N_{\phi \to \mathrm{K^+K^-}} : n \text{ identified kaons}}{N} . \tag{6.1}$$

Note that the above means n and only n identified particles, so F_0 is the fraction of decays where neither of the kaons was identified. These fractions can be written in

terms of the kaon identification efficiency η as

$$F_2 = \eta^2 \tag{6.2}$$

$$F_1 = 2\eta(1-\eta) \tag{6.3}$$

$$F_0 = (1-\eta)^2 \tag{6.4}$$

and

$$F_2 + F_1 + F_0 = 1 \ . \tag{6.5}$$

The number N is an unknown quantity in the real data, but the ratio of any two of the fractions can be determined, and from this the efficiency can be calculated. For example, if I_2 is the measured ϕ signal intensity from the decays where both kaons are identified, and I_1 is the signal intensity from the decays in which only one of the products is identified, then these measurements can be written in terms of the fractions as follows :

$$\frac{F_2}{F_1} = \frac{I_2}{N} \times \frac{N}{I_1} = \frac{I_2}{I_1} \ . \tag{6.6}$$

Using the efficiency relationships above

$$\eta = \frac{2I_2/I_1}{1+2I_2/I_1} \ . \tag{6.7}$$

In practice it was found that the intensity I_1 could not be measured from the data. Mass plots constructed from two track combinations containing only one identified kaon were found to be dominated by background (mainly from Kπ) and could not be fitted successfully. Instead a slightly different scheme was adopted, using two track combinations containing one and two identified kaons. This increased the signal to background ratio in the mass spectra to the point where viable fits were possible. The intensity of the $\phi(1020)$ signal in these plots, I_{12}, can be written as a sum of the intensity I_2 and the unmeasured intensity I_1 :

$$I_{12} = I_1 + I_2 \ , \tag{6.8}$$

and the expression for kaon identification efficiency given in equation 6.7 can be rewritten in terms of the measured intensities as follows :

$$\eta = \frac{2I_2/I_{12}}{1+I_2/I_{12}} \ . \tag{6.9}$$

This argument is only valid if the identification efficiency for each of the two kaons from a decay is the same, so possible correlations must be checked using Monte Carlo data.

6.2 Fitting the KK mass spectra

The K^+K^- invariant mass plots in the real data (in six bins of x_E) , produced as described in chapter 5, were fitted using the minimum χ^2 method, over a mass range from the KK threshold up to 1.06 GeV. The $\phi(1020)$ signal shapes for each of the fits were parametrised using the convolution of a relativistic Breit-Wigner, the theoretical line shape (see Appendix A), and a Gaussian function to account for the experimental resolution :

$$\phi_{\rm signal}(m) = \frac{1}{\sigma\sqrt{2\pi}} \int_{2m_{\rm K}}^{\infty} RBW(m')\, e^{-\frac{1}{2}\left(\frac{m-m'}{\sigma}\right)^2} dm' \ . \qquad (6.10)$$

The infinite upper bound of the integration was approximated by a range of 5σ above mass m. Outside of this range the Gaussian part of the integrand was insignificant. The background shapes were extracted from the appropriate Monte Carlo K^+K^- mass spectra.

In the fits only the overall background and signal levels, and the signal resolution parameter σ were allowed to vary. The $\phi(1020)$ mass and full width in the relativistic Breit-Wigner $RBW(m)$ were fixed at the values given in [38]. For each of the x_E regions, the intensity of the ϕ signal, I_2, was calculated from the results.

A second K^+K^- two particle mass spectrum was then constructed for each of the x_E bins using relaxed particle identification criteria: in each two track combination only one track was required to be identified as a kaon. The second track in each pair was required to pass all the other quality cuts, given in chapters 4 and 5, including those relating to the dE/dx crossover regions. These mass spectra were fitted using the same signal parametrisation, but with the resolution parameter, σ, fixed at the values measured in the first set of fits. The results were used to determine the ϕ intensity, I_{12}, in each x_E region. The results of the two sets of fits for each of the x_E bins are shown in figures 6.1 and 6.2. The procedures were repeated on the Monte Carlo data and an equivalent set of ϕ intensities measured for each of the six x_E regions.

As information regarding the generated and reconstructed type of each track was available for the simulated events it was possible to measure the number of $\phi \rightarrow K^+K^-$ decays in the samples where both, one, or neither of the kaons were

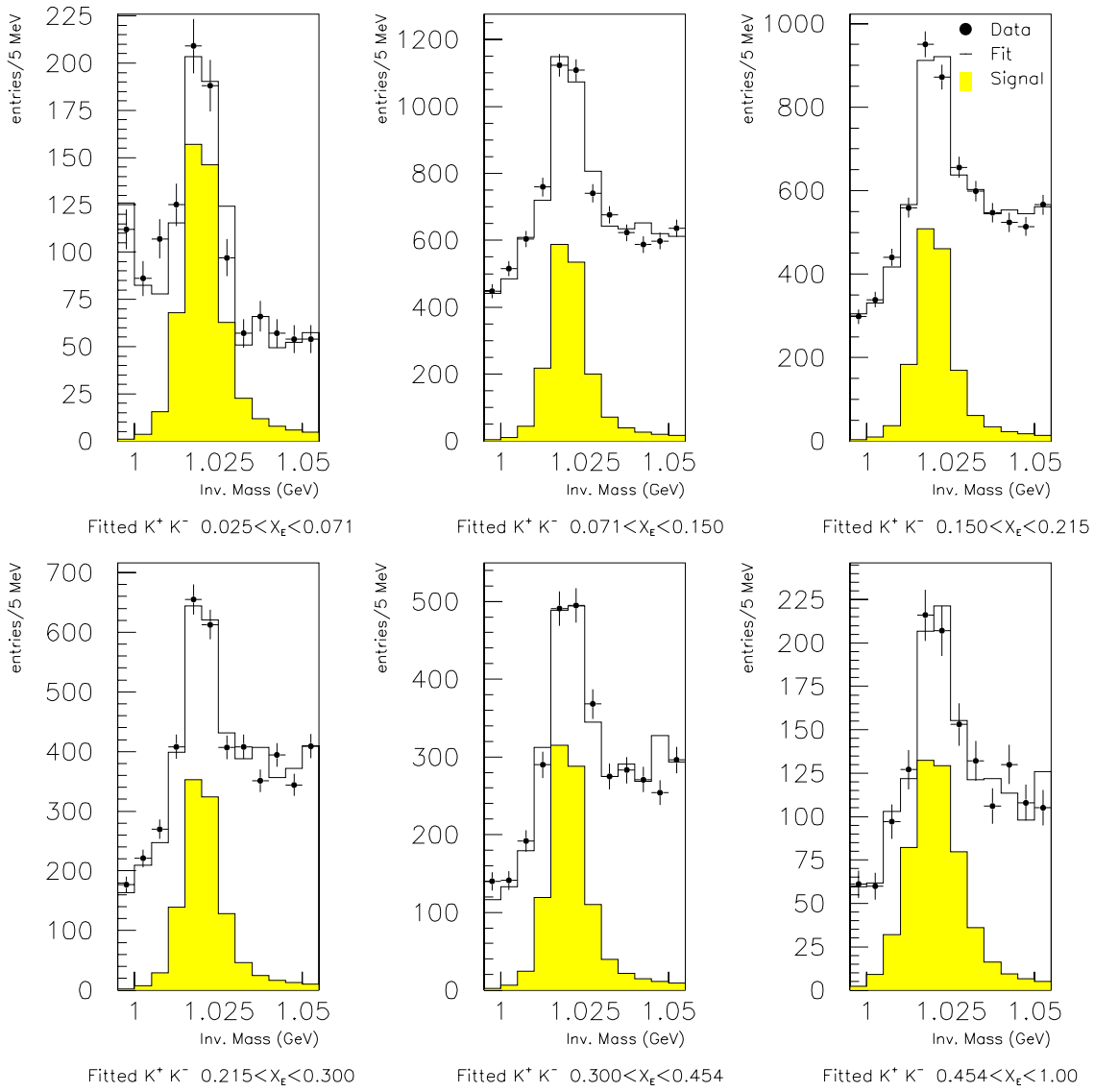

Figure 6.1: The two particle invariant mass spectra for pairs of identified kaons in six bins of x_E. The open histograms show the results of fits using a ϕ signal shape constructed from a relativistic Breit-Wigner convoluted with a Gaussian function. The fitted $\phi(1020)$ signal in each bin is displayed as a shaded histogram.

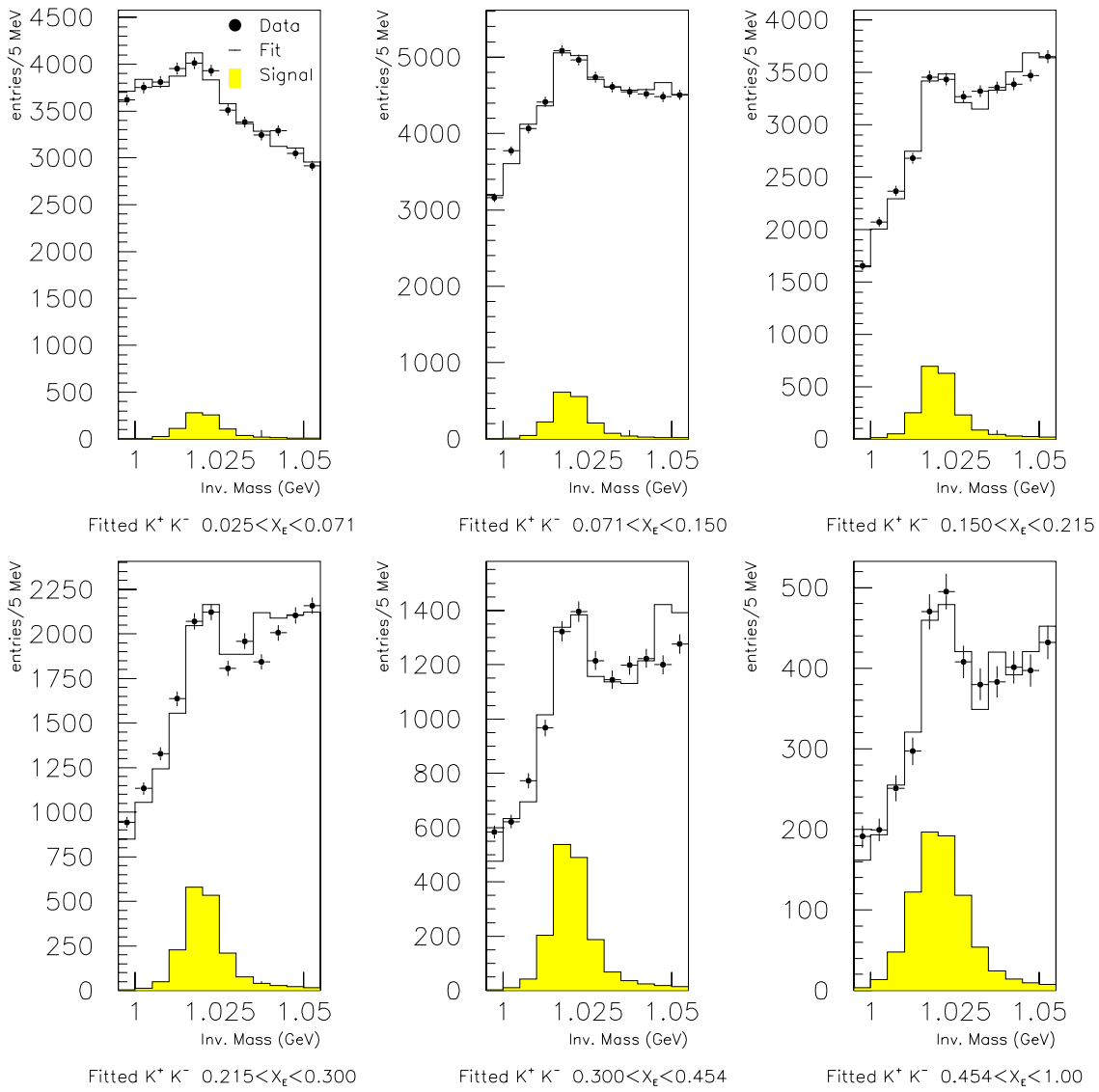

Figure 6.2: The two particle invariant mass spectra for pairs of tracks containing at least one identified kaon, in six bins of x_E. The open histograms show the results of fits using a ϕ signal shape constructed from a relativistic Breit-Wigner convoluted with a Gaussian function. The fitted $\phi(1020)$ signal in each bin is displayed as a shaded histogram.

identified, and hence to evaluate the fractions F_n. The measured values of these fractions from the Monte Carlo are given in table 6.1. These statistics were used to

x_E region	2 kaon i.d. F_2	1 kaon i.d. F_1	No kaon i.d. F_0
0.025 – 0.071	0.64	0.32	0.04
0.071 – 0.150	0.69	0.28	0.03
0.150 – 0.215	0.70	0.27	0.03
0.215 – 0.300	0.67	0.29	0.04
0.300 – 0.454	0.66	0.30	0.04
0.454 – 1.000	0.60	0.35	0.05

Table 6.1: Fractions of $\phi(1020) \rightarrow K^+K^-$ decays in the Monte Carlo event sample where two, one or zero kaons were identified using dE/dx.

determine the efficiency correlation factors (see section 6.4). The kaon identification efficiencies for the Monte Carlo events were calculated both from this method, and from the intensities measured in the fits, and both results were found to agree. In the final comparison with the data the efficiencies determined from F_n, with smaller errors, were used.

6.3 Results

Define R_I as the ratio of fitted intensities for real data. From equations 6.6 and 6.8, this quantity can also be expressed in terms of the fractions F_n (measured from the Monte Carlo data) as follows :

$$R_I = \frac{I_2}{I_{12}} = \frac{F_2}{F_1 + F_2} \ . \tag{6.11}$$

Hence using equation 6.9, the kaon identification efficiency η can be written in terms of the measurements as

$$\eta = \frac{2R_I}{1 + R_I} \ . \tag{6.12}$$

As I_2 and I_{12} are not independent their uncertainties will be correlated. For the Monte Carlo the uncertainty on the ratio can be determined using binomial statistics,

i.e.

$$\sigma_{R_I} = \sqrt{\frac{R_I(1-R_I)}{F_1+F_2}} \tag{6.13}$$

In the case of the real data the uncertainty from the fits must be taken into account. In general the uncertainty on R_I can be written

$$\sigma^2_{R_I} = \left(\frac{\partial R_I}{\partial I_{12}}\sigma_{I_{12}}\right)^2 + \left(\frac{\partial R_I}{\partial I_2}\sigma_{I_2}\right)^2 + 2\frac{\partial R_I}{\partial I_{12}}\frac{\partial R_I}{\partial I_2}C(I_{12},I_2)\ , \tag{6.14}$$

where $C(I_{12},I_2)$ represents the covariance between the two intensities. As the unmeasured intensity I_1 was relatively small in comparison with I_2 the uncertainty on I_{12} was approximated by just that on I_2. Hence

$$\left(\frac{\sigma_{R_I}}{R_I}\right)^2 \approx \left(\frac{\sigma_{I_2}}{I_2}\right)^2 + \left(\frac{\sigma_{I_2}}{I_{12}}\right)^2\ . \tag{6.15}$$

The calculated ratios R_I are given in table 6.2 and kaon identification efficiencies in table 6.3. In all the x_E regions the data and Monte Carlo values agree.

x_E region	Data $R_I = I_2/I_{12}$	Monte Carlo $R_I = F_2/(F_1+F_2)$
0.025 – 0.071	0.641±0.069	0.665±0.014
0.071 – 0.150	0.763±0.065	0.710±0.008
0.150 – 0.215	0.733±0.070	0.719±0.008
0.215 – 0.300	0.641±0.068	0.701±0.009
0.300 – 0.454	0.647±0.069	0.692±0.010
0.454 – 1.000	0.672±0.095	0.636±0.013

Table 6.2: Ratios of ϕ signals from the real data and Monte Carlo samples used to calculate the kaon identification efficiencies

6.4 Efficiency correlations

The procedure above assumes that the efficiency for identifying each kaon from a ϕ decay is the same. The simplest way to describe possible correlations is to include an extra factor r in the the expressions for F_n (equations 6.2 – 6.4) as follows :

$$F_2 \ = \ r\eta^2 \tag{6.16}$$

x_E region for ϕ	η_{data}	η_{MC}	$\eta_{\text{MC}}/\eta_{\text{data}}$
0.025 – 0.071	0.78 ± 0.05	0.799 ± 0.010	1.02 ± 0.07
0.071 – 0.150	0.87 ± 0.04	0.830 ± 0.005	0.96 ± 0.05
0.150 – 0.215	0.85 ± 0.05	0.837 ± 0.006	0.99 ± 0.06
0.215 – 0.300	0.78 ± 0.05	0.824 ± 0.006	1.06 ± 0.07
0.300 – 0.454	0.78 ± 0.05	0.818 ± 0.007	1.04 ± 0.07
0.454 – 1.000	0.80 ± 0.07	0.777 ± 0.010	0.97 ± 0.08

Table 6.3: Comparison of kaon identification efficiencies for data and Monte Carlo.

$$F_1 = 2\eta(1 - r\eta) \tag{6.17}$$

$$F_0 = 1 - 2\eta + r\eta^2 \ . \tag{6.18}$$

Here r is defined so that if η is the efficiency of identifying the first kaon, $r\eta$ is the efficiency of identifying the second. Using the above equations r can be written in terms of the fractions F_2 and F_1 as follows :

$$r = \frac{4}{(F_1/F_2 + 2)^2} \times \frac{1}{F_2} \ . \tag{6.19}$$

Note that r cannot be expressed using only ratios of the fractions, and so cannot be determined from the data. Using the fractions F_n measured from the Monte Carlo (table 6.1), r was calculated for each of the x_E regions. The resultant values are given in table 6.4.

x_E region for ϕ	correlation factor r
0.025 – 0.071	0.999 ± 0.007
0.071 – 0.150	1.004 ± 0.004
0.150 – 0.215	1.005 ± 0.004
0.215 – 0.300	1.010 ± 0.005
0.300 – 0.454	1.011 ± 0.005
0.454 – 1.000	1.005 ± 0.008

Table 6.4: Kaon identification efficiency correlation factors, measured from Monte Carlo events.

In all the x_E regions the correlation factor is consistent with unity. This indicates that the identification efficiency for each of the two kaons in a ϕ decay is the same.

This is to be expected as the low Q value of the $\phi \rightarrow K^+K^-$ decay will result in particles with similar lab momentum. As the identification efficiency is dependent on the momentum of the kaons, especially near the crossover regions of the dE/dx bands, a large difference in momentum would produce an apparent correlation in the measured efficiencies. As the Monte Carlo has been shown to simulate the data well for kaon identification this conclusion can also be applied to the real efficiency measurements.

6.5 Corrections to inclusive rate measurements

In the analysis of $\phi(1020)$ production the factors $(\eta_{MC}/\eta_{data})^2$ were applied as corrections to the measured rates and the uncertainties on these ratios were included as part of the overall systematic error, taken to be uncorrelated from bin to bin in x_E. As the kaons resulting from the $\phi(1020)$ decays used in this study cover a large momentum band (figure 6.3) it was assumed that the data and Monte Carlo identification efficiencies are comparable for all kaons, including for example those from $K^*(892)^0$ decays. The average value of η_{MC}/η_{data} in table 6.3, which amounted to 1.0, was used in the determination of the $K^*(892)^0$ multiplicity and the average of the errors on these ratios, ± 0.07, was assigned as part of the systematic uncertainty, again taken to be uncorrelated from bin to bin.

An alternative treatment of systematic errors due to identification efficiency measurements was also considered. The mass spectra integrated over all x_E were fitted as described above, both for data and Monte Carlo, and the overall kaon identification efficiency extracted. The ratio η_{MC}/η_{data} was found to be 1.00 ± 0.03. The error on this ratio was used to calculate the contribution to the systematic uncertainty on the total measured $\phi(1020)$ and $K^*(892)^0$ rates. The difference in the final systematic errors determined from this treatment and the one described above was found to be negligible.

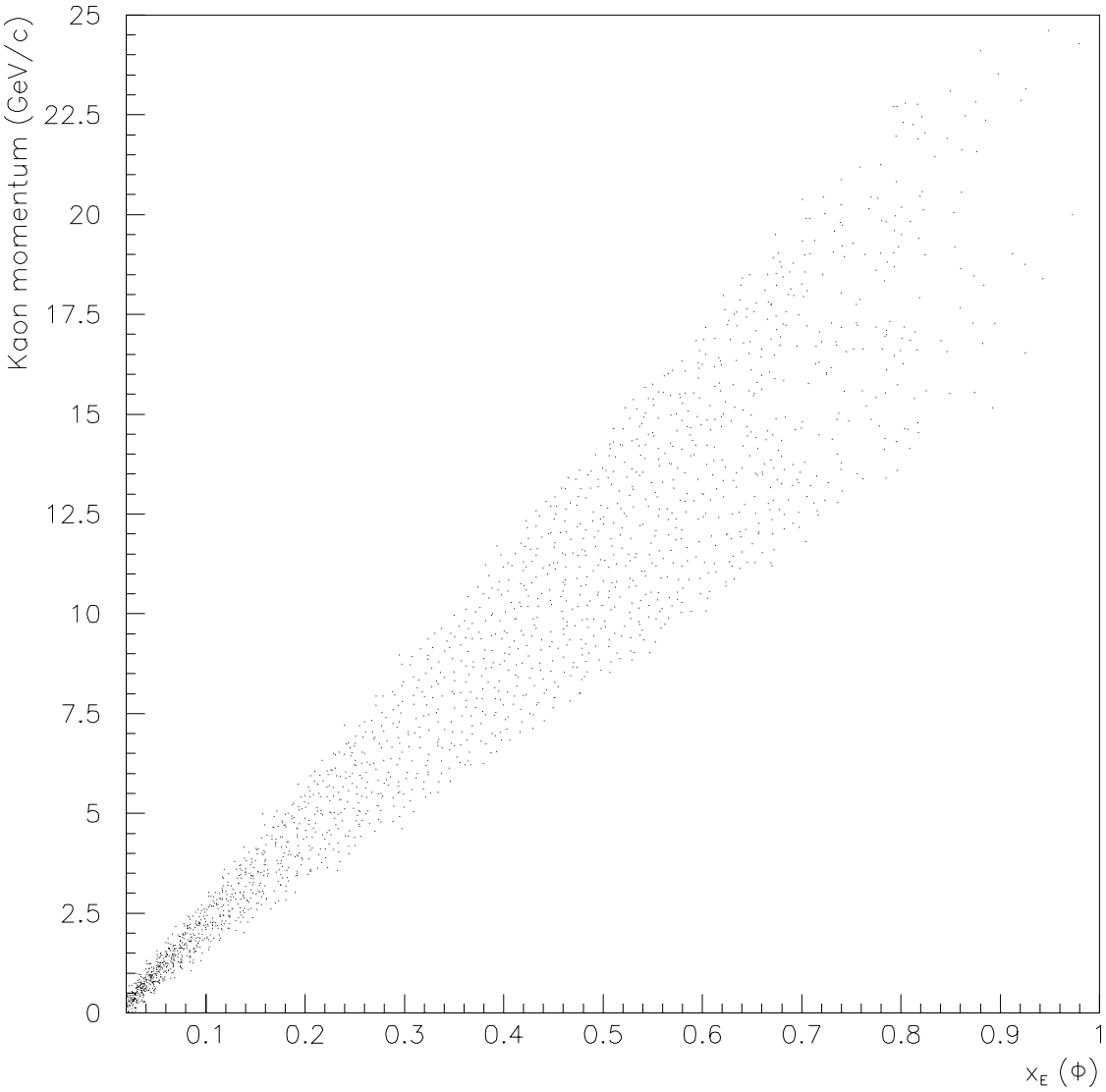

Figure 6.3: Distribution of Monte Carlo kaon momentum versus the x_E of the parent $\phi(1020)$ meson.

Chapter 7

Inclusive $\phi(1020)$ and $K^*(892)^0$ production

The inclusive production rates of $\phi(1020)$ and $K^*(892)^0$ mesons in the real data have been measured from fits to the K^+K^- and $K\pi$ two particle invariant mass spectra, produced as described in chapter 5. The results have been used to plot the differential cross sections (fragmentation functions) for the two vector mesons with respect to both scaled energy x_E and $\xi = \ln(1/x_p)$.

7.1 Fitting the K^+K^- mass spectra

The K^+K^- mass spectra were fitted using the minimum χ^2 method in exactly the same manner as in the earlier OPAL vector meson analysis [1]. The plots representing the six x_E regions were fitted over an invariant mass range from the KK threshold up to 1.06 GeV. In each x_E region the shapes of the signal and background contributions were extracted from the appropriate Monte Carlo mass spectra. In the fit the signal intensity and the level of combinatorial background were allowed to vary.

The results of the fits for each of the x_E bins are shown in figure 7.1. As

x_E Region	$x_{\rm lw}$	Multiplicity /Z^0 decay	$\frac{1}{\sigma_{\rm had}}\left[\frac{d\sigma}{dx_E}\right]$
0.025 – 0.071	0.046	$0.031 \pm 0.003 \pm 0.005$	$0.67 \pm 0.07 \pm 0.12$
0.071 – 0.150	0.108	$0.028 \pm 0.002 \pm 0.003$	$0.35 \pm 0.02 \pm 0.04$
0.150 – 0.215	0.182	$0.013 \pm 0.001 \pm 0.002$	$0.20 \pm 0.01 \pm 0.03$
0.215 – 0.300	0.256	$0.011 \pm 0.001 \pm 0.002$	$0.13 \pm 0.01 \pm 0.02$
0.300 – 0.454	0.372	$0.010 \pm 0.001 \pm 0.002$	$0.06 \pm 0.005 \pm 0.01$
0.454 – 1.000	0.654	$0.005 \pm 0.001 \pm 0.001$	$0.01 \pm 0.001 \pm 0.002$
0.023 – 0.025	-	0.002^*	-
0.023 – 1.000	-	$0.100 \pm 0.004 \pm 0.007$	-

* - Unobserved region, multiplicity determined using JETSET 7.3 / HERWIG 5.5

Table 7.1: Results for inclusive $\phi(1020)$ production.

the Monte Carlo mass spectra used for the fits had been normalised to the same number of Z^0 decays as in the data, the results were a direct measurement of the data to Monte Carlo intensity ratio for the $\phi(1020)$. The production rate in each of the x_E regions could then be determined by scaling the JETSET multiplicities and taking into account the corrections for particle identification efficiency calculated as described in chapter 6. To account for the small unobserved region at low x_E the Monte Carlo behaviour was assumed. Both JETSET 7.3 and HERWIG 5.5 were found to agree on the correction. The measured rates for each of the x_E bins are given in table 7.1. The overall multiplicity was determined to be $0.100 \pm 0.004 \pm 0.007$ per event. The first quoted error is statistical and the second is an estimate of the systematic error on the measurement, taken to be uncorrelated from bin to bin in x_E.

7.2 Fitting the Kπ mass spectra

As was pointed out earlier, an understanding of the $\rho(770)^0$ reflection in the Kπ mass spectra is essential in the determination of the $K^*(892)^0$ production rate. A study of the $\pi^+\pi^-$ invariant mass spectra in [1], and more recently in [40], revealed a marked difference between the data and JETSET Monte Carlo signal shapes for

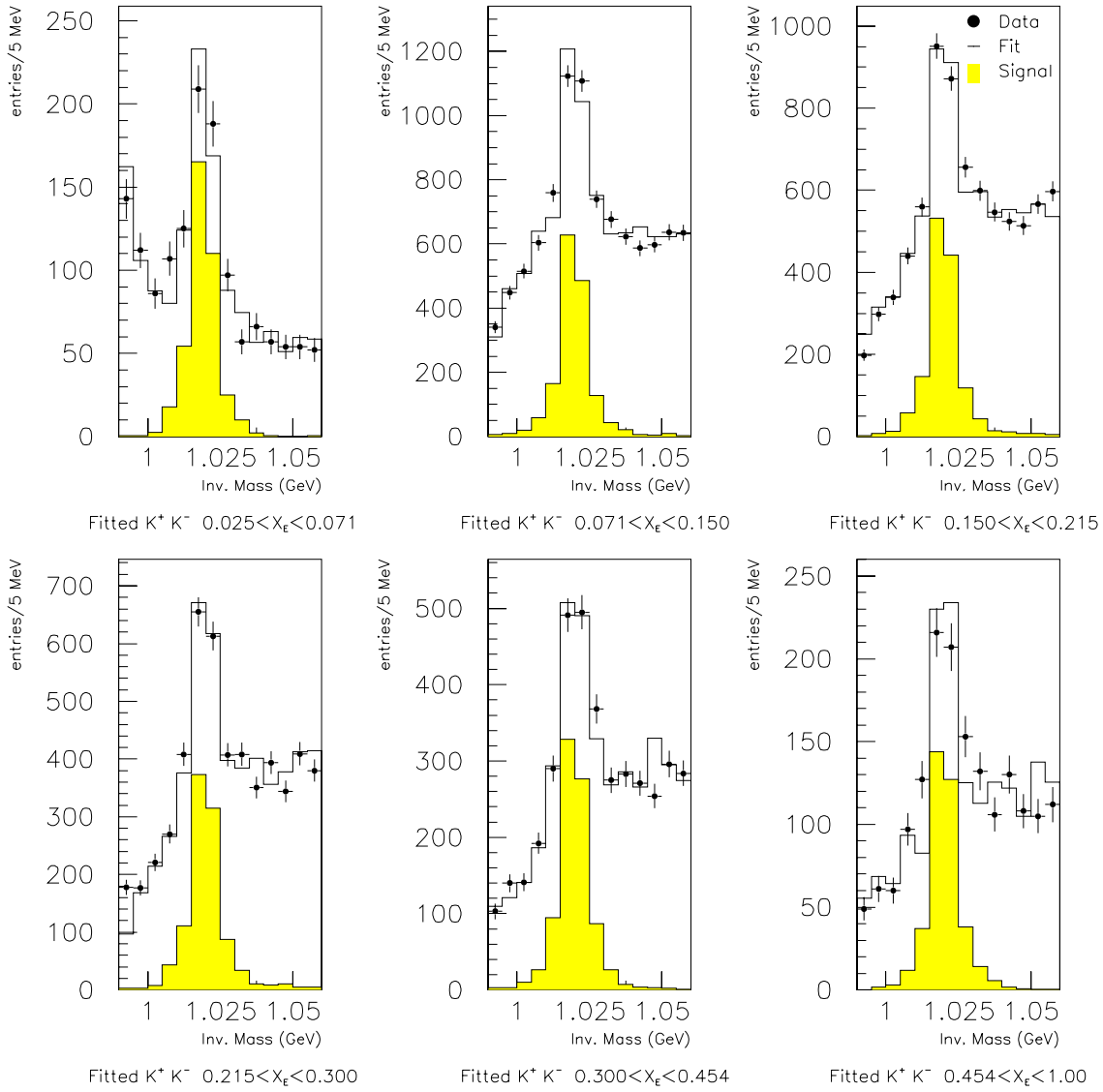

Figure 7.1: Fits to the KK mass plots in six bins of x_E. The open histograms show the results of the fits, and the shaded plots are the $\phi(1020)$ signals.

$\rho(770)^0$. It was suggested that the distortion could be due to Bose-Einstein correlations which were not simulated in default JETSET. A further study of the effect on the $\rho(770)^0$ line shape by these correlations and other mechanisms was made in [41]. Here it was suggested that the shape of the ρ^0 signal in $\pi^+\pi^-$ mass spectra could be parametrised as a distorted relativistic Breit-Wigner, written for a mass m as

$$I_\rho(m) = RBW(m)\left[1 + C\left(\frac{m_\rho^2 - m^2}{m\Gamma}\right)\right] , \tag{7.1}$$

where Γ is the mass dependent width of the relativistic Breit-Wigner $RBW(m)$ [42] and C is a variable parameter which depends on the momentum of the ρ^0, varying from around 1.0 at low values of scaled momentum x_p, down to zero for high momenta. The overall effect of equation 7.1 is to move the peak of the ρ^0 background to a lower mass, by up to 40 MeV for C equal to one, as shown in figure 7.2.

In order to study the effect of this on the ρ^0 background in the Kπ mass spectra, distorted reflections were generated using the following procedure. Two body $\rho^0 \rightarrow \pi^+\pi^-$ decays were generated using the Monte Carlo program GENBOD [43] with a line shape determined from the parametrisation given above. The behaviour of C was represented simply by $(1 - x_p)$ with the momentum spectrum of the ρ^0 mesons taken from JETSET.

Using the histograms of the variation of pion to kaon misidentification probability with momentum, constructed in chapter 5 (figure 5.4), Kπ reflections were created from generated $\rho^0 \rightarrow \pi^+\pi^-$ decays. The reflections were plotted in the same bins of x_E as used in the $K^*(892)^0$ analysis. Using the same procedure a second set of reflections was generated using a normal Breit-Wigner function as input to GENBOD rather than the above parametrisation.

Three separate sets of fits were made to the Kπ mass spectra over an invariant mass range from 0.64 to 1.2 GeV. For the first fits, the JETSET $\rho(770)^0$ shape (a simple non-relativistic Breit-Wigner) was used, but for the other two the reflections generated using GENBOD, with and without distortions, were included instead, with the intensity normalised to the default JETSET value in each case. For all the fits the $K^*(892)^0$ signal shape was taken from the Monte Carlo mass spectra, the intensity from the $\phi(1020)$ background was fixed to values obtained from earlier fits to the KK spectra and all other non combinatorial backgrounds except for the $\rho(770)^0$ were set at default JETSET levels. The fitted spectra using the JETSET

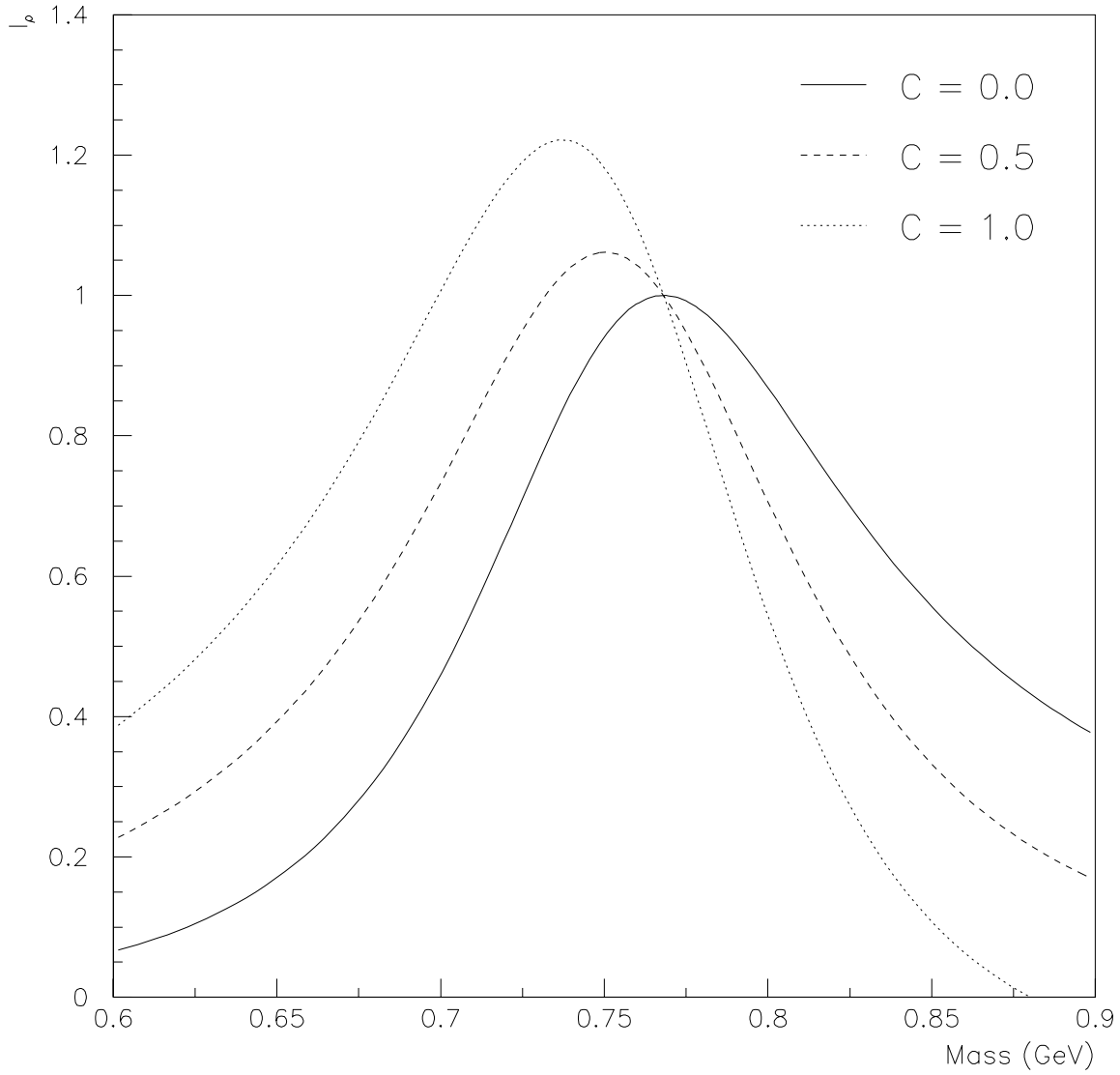

Figure 7.2: Line shapes for $\rho(770)^0$ using a distorted relativistic Breit-Wigner function (equation 7.1) for various values of the parameter C.

x_E Region	$x_{\rm lw}$	Multiplicity /Z^0 decay	$\frac{1}{\sigma_{\rm had}}\left[\frac{d\sigma}{dx_E}\right]$
0.021 – 0.044	0.033	$0.151 \pm 0.014 \pm 0.010$	$6.56 \pm 0.61 \pm 0.43$
0.044 – 0.071	0.057	$0.121 \pm 0.019 \pm 0.016$	$4.48 \pm 0.70 \pm 0.59$
0.071 – 0.107	0.088	$0.133 \pm 0.008 \pm 0.015$	$3.69 \pm 0.22 \pm 0.42$
0.107 – 0.150	0.127	$0.097 \pm 0.006 \pm 0.009$	$2.25 \pm 0.14 \pm 0.21$
0.150 – 0.180	0.165	$0.040 \pm 0.004 \pm 0.004$	$1.33 \pm 0.13 \pm 0.13$
0.180 – 0.215	0.197	$0.037 \pm 0.004 \pm 0.004$	$1.06 \pm 0.11 \pm 0.11$
0.215 – 0.255	0.234	$0.041 \pm 0.003 \pm 0.004$	$1.02 \pm 0.08 \pm 0.10$
0.255 – 0.300	0.278	$0.031 \pm 0.003 \pm 0.003$	$0.69 \pm 0.07 \pm 0.07$
0.300 – 0.454	0.372	$0.055 \pm 0.003 \pm 0.005$	$0.36 \pm 0.02 \pm 0.03$
0.454 – 1.000	0.661	$0.026 \pm 0.002 \pm 0.002$	$0.05 \pm 0.004 \pm 0.004$
0.020 – 0.021	-	0.011*	-
0.020 – 1.000	-	$0.743 \pm 0.027 \pm 0.027$	-

* - Unobserved region, multiplicity determined using JETSET 7.3 / HERWIG 5.5

Table 7.2: Results for inclusive $K^*(892)^0$ production.

$\rho(770)^0$ reflections are shown in figure 7.3.

The fit results using the JETSET ρ^0 reflection and those with generated ρ^0 shapes with no distortions were consistent. This indicated that the generated reflections from GENBOD were reliable even though they had not been passed through a full detector simulation. When the ρ^0 reflections included distortion effects as parametrised by equation 7.1, the fitted $K^*(892)^0$ intensity was consistently lower. This was to be expected as the distortion effects move the reflected ρ^0 peak down in mass closer to the $K^*(892)^0$, thus reducing the effective fitted K^* intensity.

The mean of the two fit values for each x_E bin was used to calculate the overall $K^*(892)^0$ production rate. The difference between the two was used as an estimate of the systematic uncertainty due to the $\rho(770)^0$ reflection. As in the $\phi(1020)$ analysis a small correction was applied for the unobserved region in x_E based on JETSET and HERWIG predictions. The measured rates for each of the x_E regions are given in table 7.2. The overall production rate was determined to be $0.74 \pm 0.03 \pm 0.03$ $K^*(892)^0$ mesons per hadronic Z^0 decay.

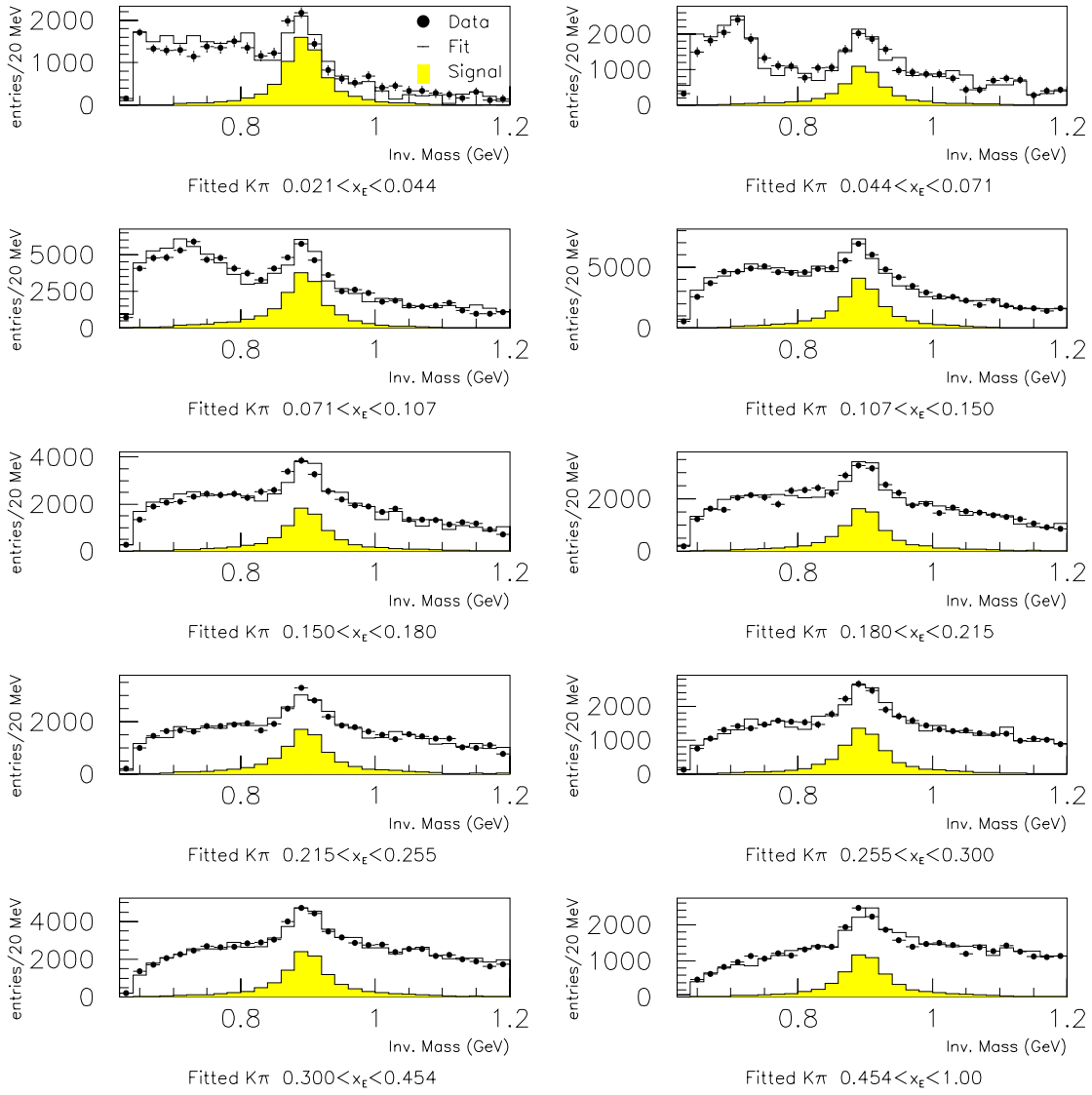

Figure 7.3: Fits to the Kπ mass plots in ten bins of x_E. The open histograms show the results of the fits, and the shaded plots are the $K^*(892)^0$ signals.

7.3 Differential cross sections

For both the $\phi(1020)$ and $K^*(892)^0$ mesons, normalised differential cross sections were calculated and plotted as a function of x_E. To determine the appropriate positions $x_{\rm lw}$ for the data points within the x_E bins, the procedure recommended in [44] was used. Both HERWIG and JETSET curves in each bin were considered, but significant differences in the calculated positions were found only for the highest x_E region, which corresponded to the widest bin. For this point the mean of the two positions was used and the difference was taken to be the uncertainty on the x_E position in the bin. The resulting values of $x_{\rm lw}$ are given in tables 7.1 and 7.2. The results are shown in figures 7.4 and 7.5 together with the fragmentation functions for JETSET 7.3 and HERWIG 5.5. The fragmentation function is also shown for JETSET with certain parameters tuned as described in [1] to reproduce a number of measured production rates; two JETSET parameters were altered, the strangeness suppression factor, PARJ(2), was set to 0.245 (the default value is 0.3) and the probability that a strange meson will have spin 1, PARJ(12), was changed from 0.6 to 0.43. The x_E bin limits are also shown on the plots, in the manner recommended in [44].

For a comparison with measurements of other hadron states the entire $\phi(1020)$ and $K^*(892)^0$ analyses were repeated using bins of the variable $\xi = \ln(1/x_p)$ rather than x_E. The modified leading log approximation in QCD with local parton-hadron duality (MLLA+LPHD) [16] predicts that differential cross sections with respect to this variable should have a Gaussian like shape. Figures 7.6 and 7.7 show the measured distributions for $\phi(1020)$ and $K^*(892)^0$ along with the Gaussian fits used to measure the peak positions. The values of $\xi_{\rm peak}$ were determined to be 2.29 ± 0.05 and 2.40 ± 0.04 for the $\phi(1020)$ and $K^*(892)^0$ respectively.

7.4 Systematic errors

The effects on the production rates of the $\phi(1020)$ and $K^*(892)^0$ from the various sources of systematic error investigated are summarised in table 7.3.

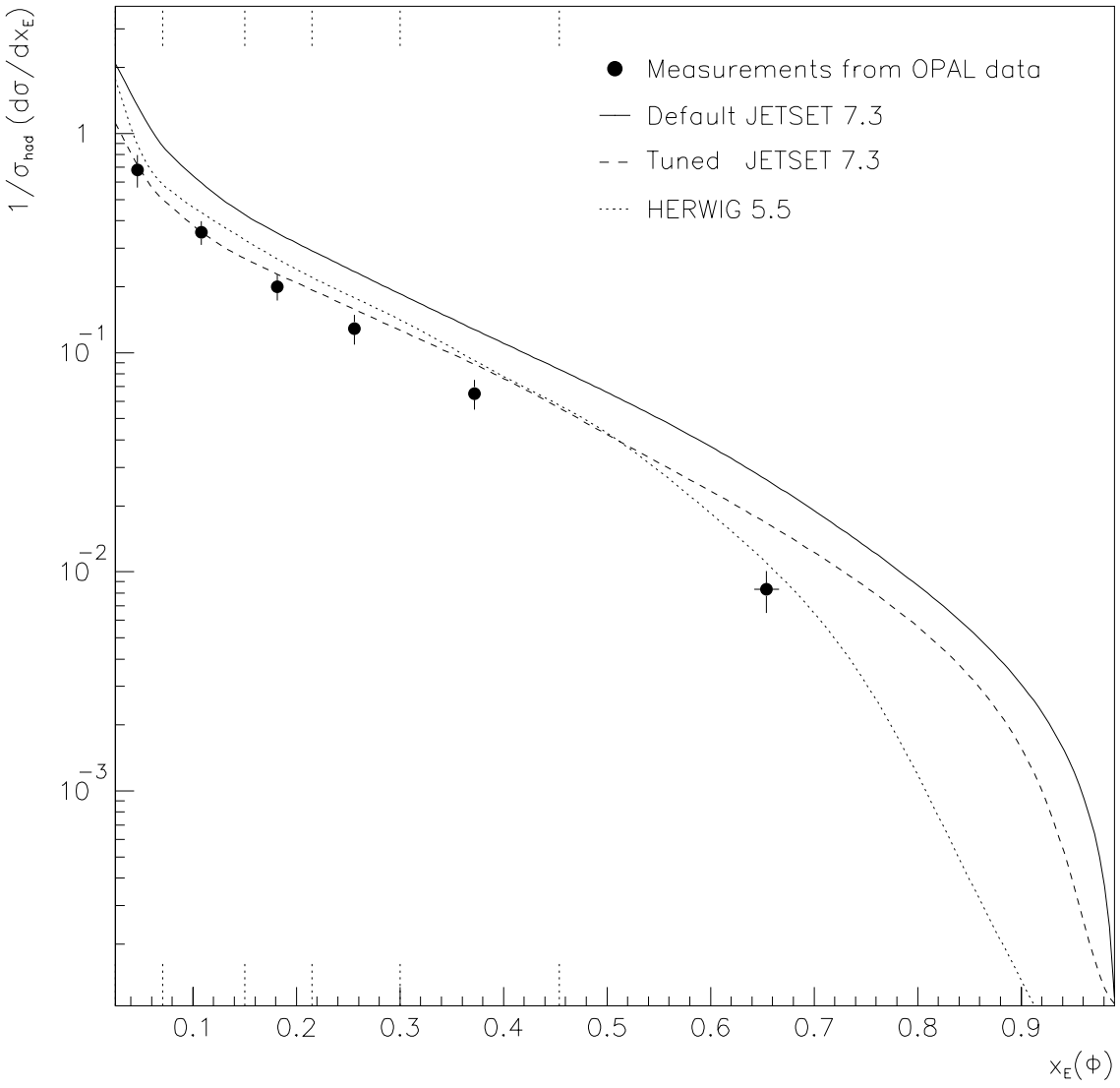

Figure 7.4: Differential cross sections for measured and simulated $\phi(1020)$ production. The error bars show the combined statistical and systematic uncertainty on each point. The bin ranges are indicated by means of the short vertical lines at the edges of the plot.

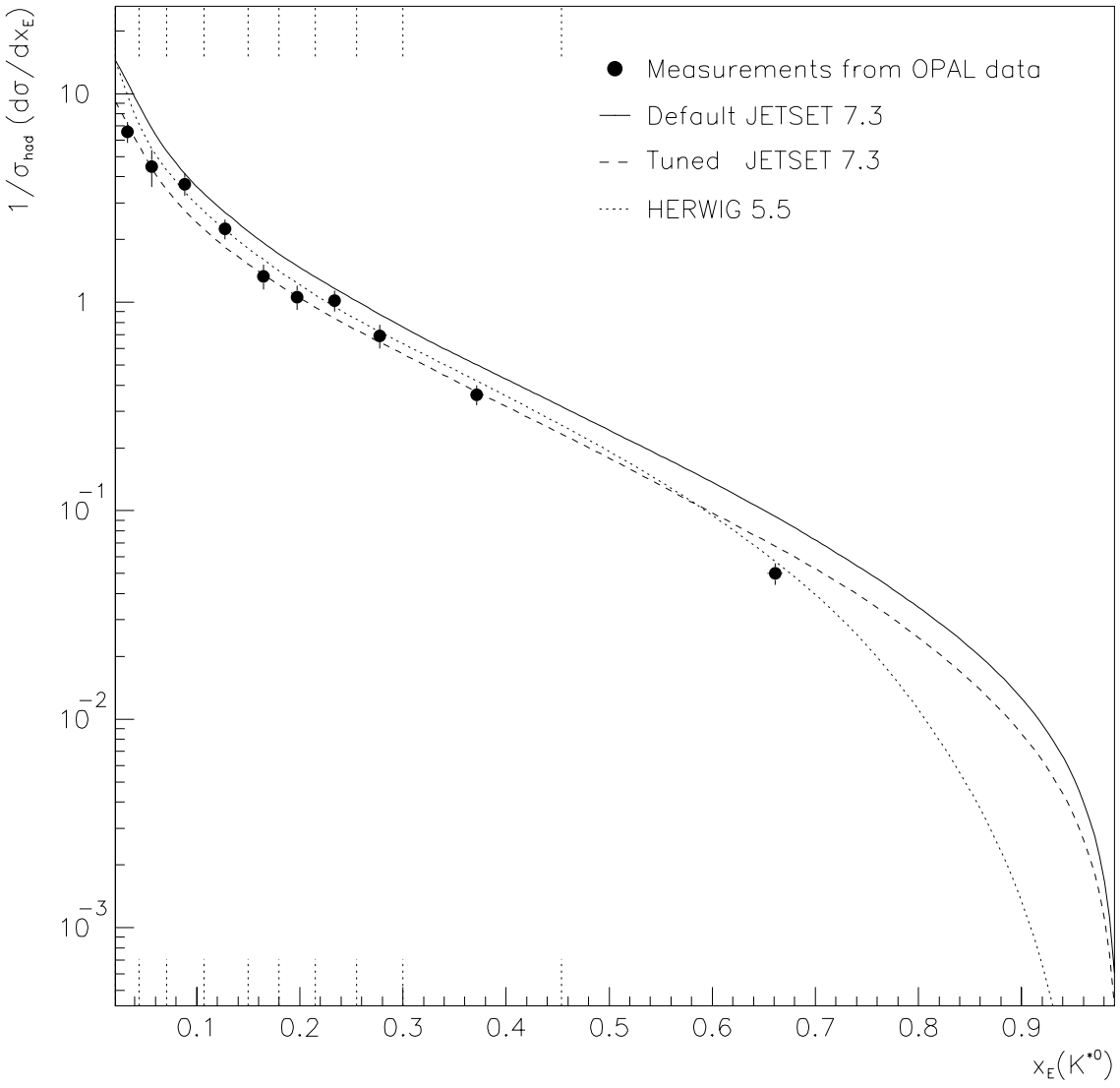

Figure 7.5: Differential cross sections for measured and simulated $K^*(892)^0$ production. The error bars show the combined statistical and systematic uncertainty on each point. The bin ranges are indicated by means of the short vertical lines at the edges of the plot.

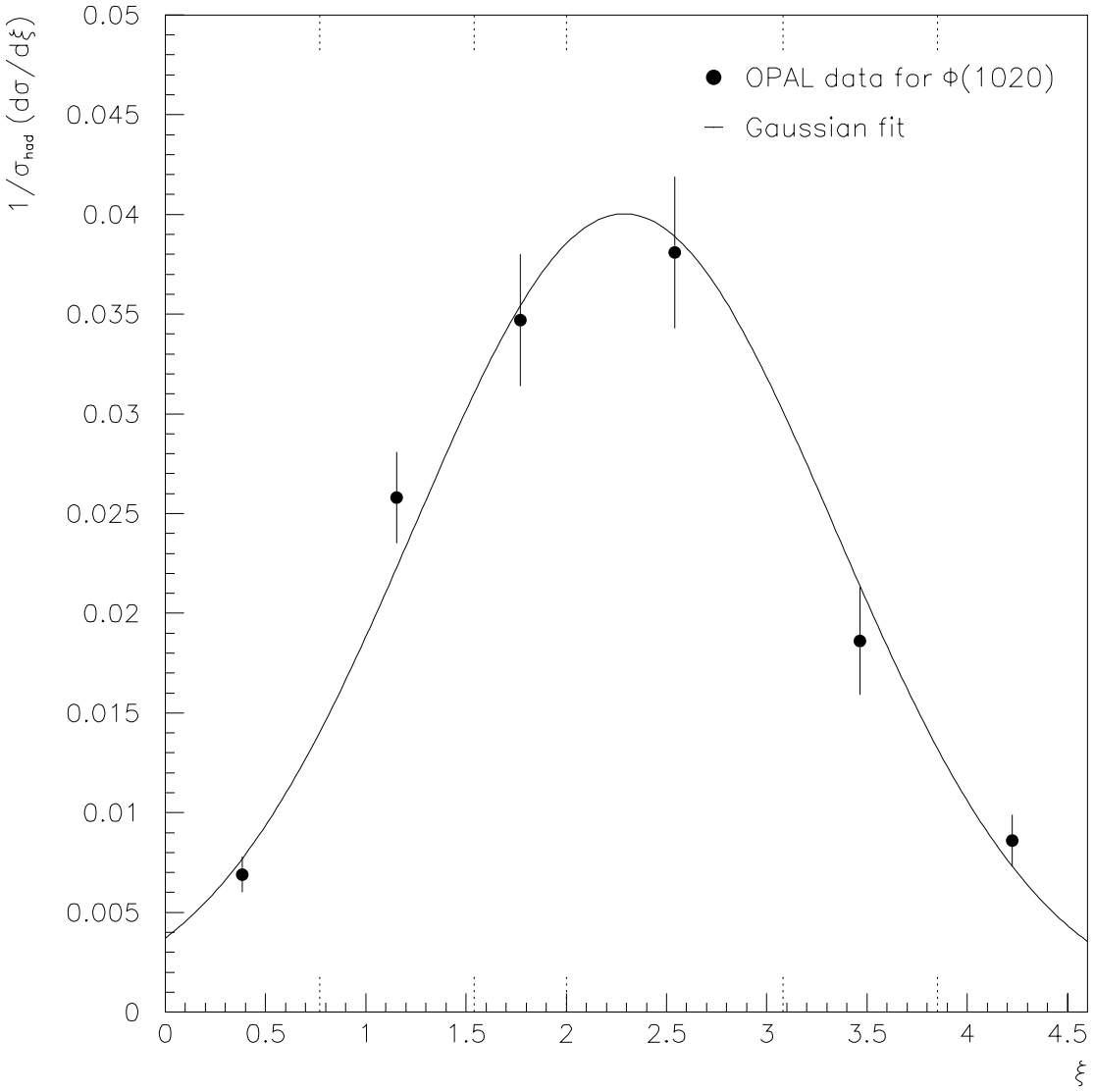

Figure 7.6: Differential cross section for $\phi(1020)$ as a function of $\xi = \ln(1/x_p)$. The error bars show the combined statistical and systematic uncertainty on each point. The bin ranges are indicated by means of the short vertical lines at the edges of the plot.

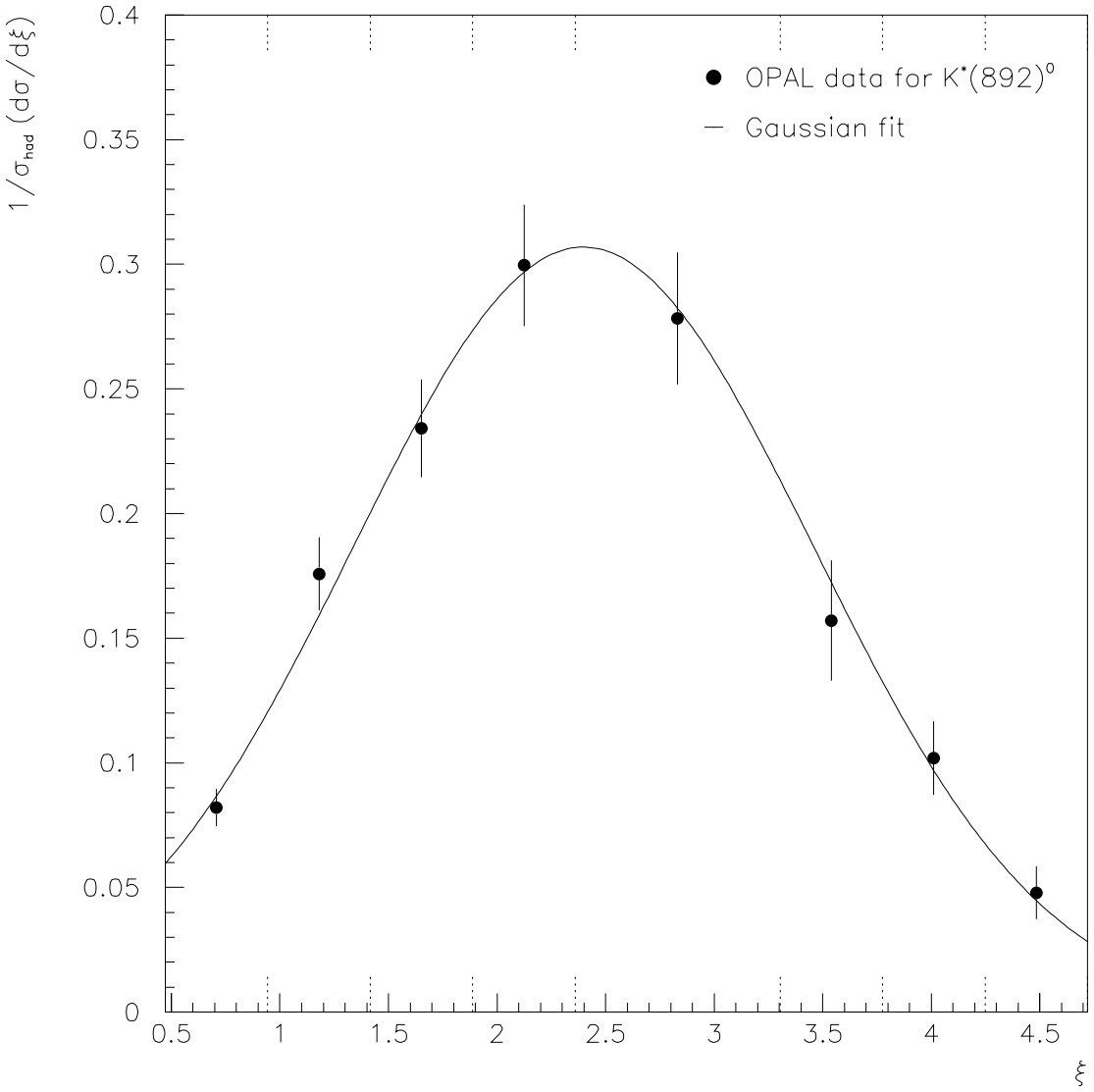

Figure 7.7: Differential cross section for $K^*(892)^0$ as a function of $\xi = \ln(1/x_p)$. The error bars show the combined statistical and systematic uncertainty on each point. The bin ranges are indicated by means of the short vertical lines at the edges of the plot.

The normalisation procedure used to compare the data and Monte Carlo samples resulted in an overall 1.4% error on the final multiplicities. This came from both the reweighting of Monte Carlo events to account for matching inefficiencies between the central jet chamber and outer z-chambers and from the model dependence of the quality cuts.

The systematic effects due to uncertainties in the kaon particle identification were calculated using the errors on the efficiency measurements described in chapter 6. The outcome of this was a 5.6% uncertainty on the $\phi(1020)$ multiplicity and a 2.4% error on the $K^*(892)^0$. These values turned out to be the largest contributions to the systematic errors. However it must be noted that they stem from the fits used in the efficiency measurements and should decrease in magnitude with increased statistics.

As the $\phi(1020)$ is a narrow state with a natural width similar to the intrinsic mass resolution of the detector, discrepancies in the shape of the state between the data and Monte Carlo may have a systematic effect on the fits. To test this, both the data and JETSET Monte Carlo K^+K^- mass spectra were fitted to a combination of a relativistic Breit-Wigner convoluted with a Gaussian (the same signal shape as used in the efficiency calculations), and a Weibull function [45] to represent the background. This two parameter function is written for an invariant mass m,

$$W(m) = \frac{P_1}{P_2}\left(\frac{m - t_{KK}}{P_2}\right)^{P_1-1} \exp\left[-\left(\frac{m - t_{KK}}{P_2}\right)^{P_1}\right] , \qquad (7.2)$$

where t_{KK} is the KK mass threshold. The width of the Gaussian part, which provides a measure of the resolution of the signal, was found to be compatible between the two data sets. The fits were then repeated for the data mass spectra with the resolution fixed at $\pm 1\sigma$ of the fitted width in the Monte Carlo. Using this procedure the intensity of the $\phi(1020)$ signal was found to vary by 1%.

Bose-Einstein correlations and residual correlations represent a source of systematic errors in the two vector states. For the $\phi(1020)$ the systematic errors for this effect were taken directly from the published work [1] where a reweighting technique was used to simulate the effect in the Monte Carlo mass plots. A 3.5% effect on the overall rate is reported from the study and this was included in the systematics in the present analysis. For the $K^*(892)^0$ the effect is indirect, occurring in $\pi^+\pi^-$ systems which are reflected into the $K\pi$ mass plots due to $\pi \rightarrow K$ misidentification.

Source of systematic error	error on $\phi(1020)$	error on $K^*(892)^0$ rate
Normalisation of Monte Carlo	± 0.0010	± 0.010
Particle i.d. efficiency	± 0.0056	± 0.018
Mass resolution	± 0.0010	-
Bose-Einstein effects	± 0.0035	± 0.015
$\rho(770)^0$ intensity	-	± 0.009
Branching ratio	± 0.0017	-
Total	± 0.0070	± 0.027

Table 7.3: Systematic uncertainties on $\phi(1020)$ and $K^*(892)^0$ rates.

This effect has been studied as reported in section 7.2.

As the $\rho(770)^0$ production rate has not been measured reliably in Z^0 decay [1, 6, 40, 41], mainly due to problems in understanding the line shape, the effect of varying the intensity of the reflection in the mass plots was studied. It was found that a variation of $\pm 30\%$ in the ρ^0 intensity resulted in only a 1.2% change in the fitted $K^*(892)^0$ intensity and had a negligible effect on the $\phi(1020)$. Finally a 1.6% uncertainty was added to the systematic error on the measured $\phi(1020)$ rate to account for the uncertainty on the $\phi \rightarrow K^+K^-$ branching ratio [38].

7.5 Conclusions

The measurements of $\phi(1020)$ and $K^*(892)^0$ meson production in Z^0 decay reported in this chapter represent a significant improvement in precision over those previously published. Table 7.4 shows the measured production rates together with the values obtained from the analysis of 1990 OPAL data [1] and from JETSET and HERWIG Monte Carlo. Also listed are the multiplicities obtained from JETSET after certain parameters had been adjusted as described in section 7.3. For both the vector states, default JETSET and HERWIG predict a significantly larger rate than the measured values. The tuned version of JETSET however is in agreement with the measured $K^*(892)^0$ rate and within two standard deviations of the experimental $\phi(1020)$ multiplicity.

Particle	1990 - 92 data	1990 data	JETSET default (tuned)	HERWIG
$K^*(892)^0$	0.74 ± 0.04	0.76 ± 0.09	1.05 (0.71)	0.87
$\phi(1020)$	0.100 ± 0.008	0.086 ± 0.018	0.191 (0.115)	0.136

Table 7.4: Measured and predicted multiplicities for vector meson production in Z^0 decay.

The overall shape of the differential cross sections measured as a function of x_E (figures 7.4 and 7.5) are in good agreement with both Monte Carlo models for x_E less than 0.5. The Monte Carlo predictions for the fragmentation functions are significantly different for $x_E > 0.5$. In this region the data for both vector mesons are in somewhat better agreement with HERWIG than with JETSET.

The differential cross sections plotted with respect to the variable $\xi = \ln(1/x_p)$ were found to fit well to a Gaussian shape. The measured peak positions plotted against particle mass are shown in figure 7.8 along with data from other hadron states [3, 4, 46]. For each particle, the most precise measurement in the literature is shown. The modified leading log approximation in QCD, using local parton-hadron duality [16] predicts a linear decrease in $\xi_{\rm peak}$ as a function of mass. The JETSET Monte Carlo model predicts values of $\xi_{\rm peak}$ which are in broad agreement with the data for all the measured hadrons. A linear decrease in $\xi_{\rm peak}$ as a function of mass is obtained from the Monte Carlo when only primary hadrons are considered, as shown in figure 7.8. The inclusion of secondary particles from the decay of other hadrons smears out the simple mass dependence, thus producing the effect observed in the data.

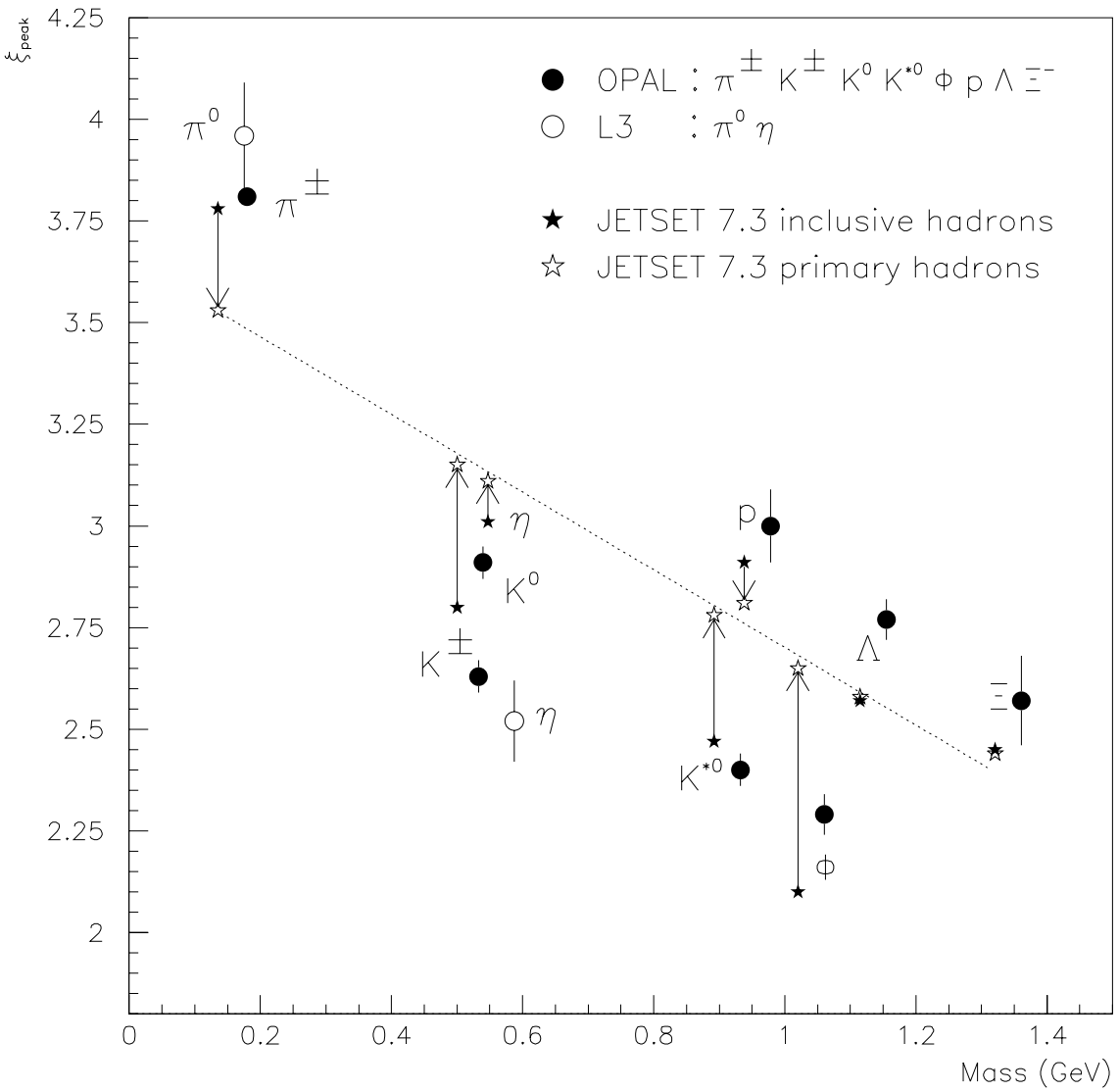

Figure 7.8: The variation of ξ_{peak} with mass for various hadron states. Measured data points are shown as circles, with the JETSET values shown as stars. For π and K, one star represents both the charged and neutral states. The arrows show the change in ξ_{peak} for JETSET Monte Carlo if only primary hadrons are considered.

Chapter 8

Inclusive $K_2^*(1430)^0$ production

In the original analysis of strange vector meson production [1], based on the data taken by OPAL in 1990, the measured Kπ mass spectrum contained some evidence for the production of the tensor meson $K_2^*(1430)^0$. After two further years of LEP running the increase in the number of recorded multihadronic events has made a measurement of the inclusive production rate of this meson possible. Using the result, the JETSET parameter which governs the level of tensor meson production has been tuned and its effect on the inclusive rates of other vector and tensor mesons studied.

8.1 Fitting the Kπ mass spectra

As the $K_2^*(1430)^0$ is a wide state, with a natural width of 109 MeV, additional cuts were introduced to obtain the best possible signal to background ratio in the Kπ mass spectra. In order to reduce the combinatorial background from Kπ and $\pi\pi$ pairs the selected tracks were required to pass more stringent quality cuts before particle identification was attempted, than those used for the vector states. The minimum number of points of $\mathrm{d}E/\mathrm{d}x$ measurement was increased from 20 to 100 and the number of z space points from one to five. It was found that improving the $\mathrm{d}E/\mathrm{d}x$ and momentum measurement in this way was more effective than tightening

the cuts made on the dE/dx weights. The kaon identification efficiencies for both data and Monte Carlo were re-evaluated for this new set of cuts, following the procedures described in chapter 6.

The Kπ two-particle invariant mass spectra were plotted by combining identified kaons with all the other tracks in each event. Two regions of x_E were considered, up to 0.3 and from 0.3 to 1.0. As in the $K^*(892)^0$ analysis the histograms for like and unlike charge combinations were subtracted bin by bin to emphasise the signal. The resultant 'subtracted' spectra are shown in figure 8.1. A clear signal is visible for the lower x_E region, but at large x_E the effects of charmed meson production serve to complicate the Kπ mass spectrum. This meant that the production rate could only be measured over a limited x_E range.

The multiplicity could not be extracted from the data using the same procedure as for the vector mesons since the JETSET event sample did not include tensor mesons. The Monte Carlo data generated using HERWIG did contain the $K_2^*(1430)^0$, but it could not be used either in the fits since HERWIG does not simulate the natural widths of resonant states. The HERWIG sample was used however to calculate the acceptance. Instead the data were fitted to a parametrisation made up of signal and background contributions. Two signal shapes were fitted to the peak, a relativistic Breit-Wigner, the theoretical shape of the state, and a simple Gaussian. These shapes were combined with both parabolic and exponential background functions, yielding four possible fit combinations. The fits were carried out over a mass range from 1.05 up to 1.8 GeV. Initially the mass and width of the signal were allowed to vary and the resulting parameters were found to be consistent with the nominal values for the $K_2^*(1430)^0$ [38]. For example, using a relativistic Breit-Wigner signal and an exponential background the mass and width of the state were determined to be $m_{K_2^*} = 1.434 \pm 0.010$ GeV and $\Gamma_{K_2^*} = 0.104 \pm 0.032$ GeV. For the final fits these two parameters were fixed at the Particle Data Group default values. The results of these final fits are shown in figure 8.2.

Two further signal measurements were made by fitting the background functions to the side bands of the mass spectra. The overall signal was taken as the mean of the values obtained from the six fits. The deviation from this mean was used as an estimate of the systematic uncertainty in the measured signal.

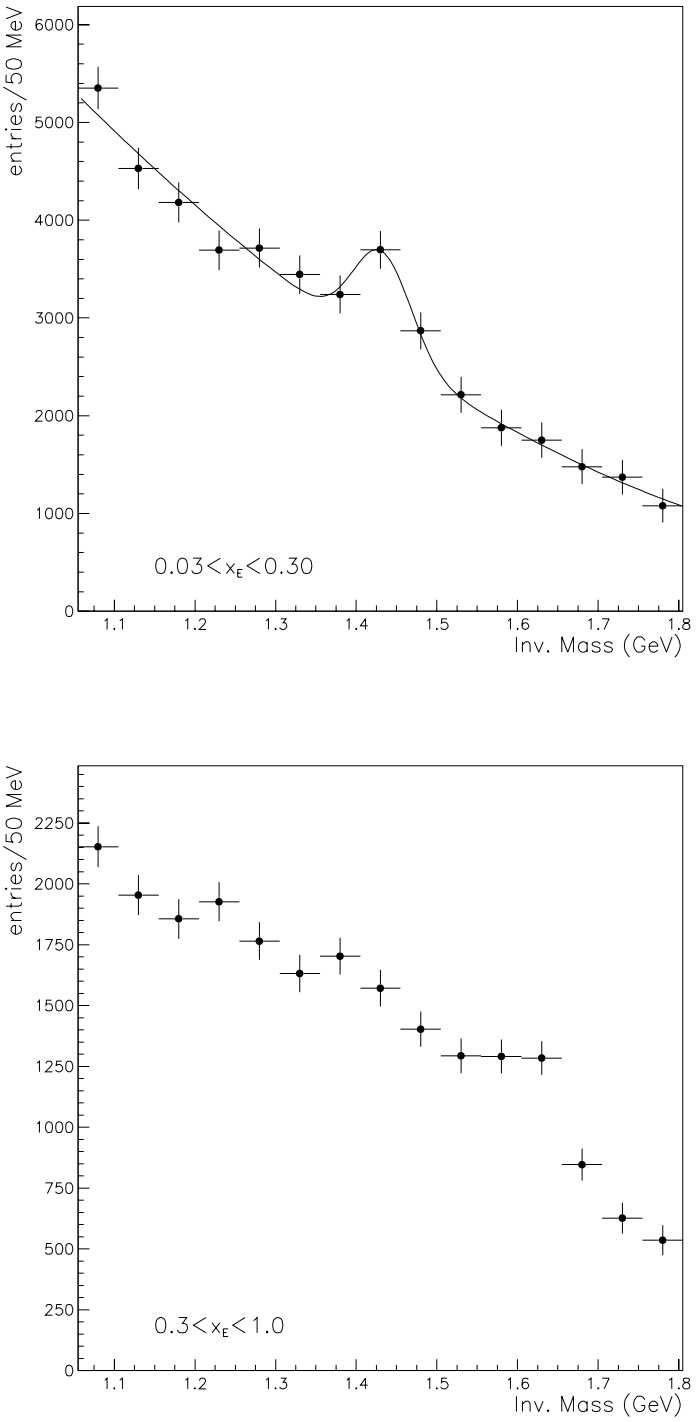

Figure 8.1: 'Subtracted' Invariant mass spectra for Kπ combinations around the $K_2^*(1430)^0$ mass. The fit shown on the upper plot is to the combination of an exponential background and a Gaussian signal.

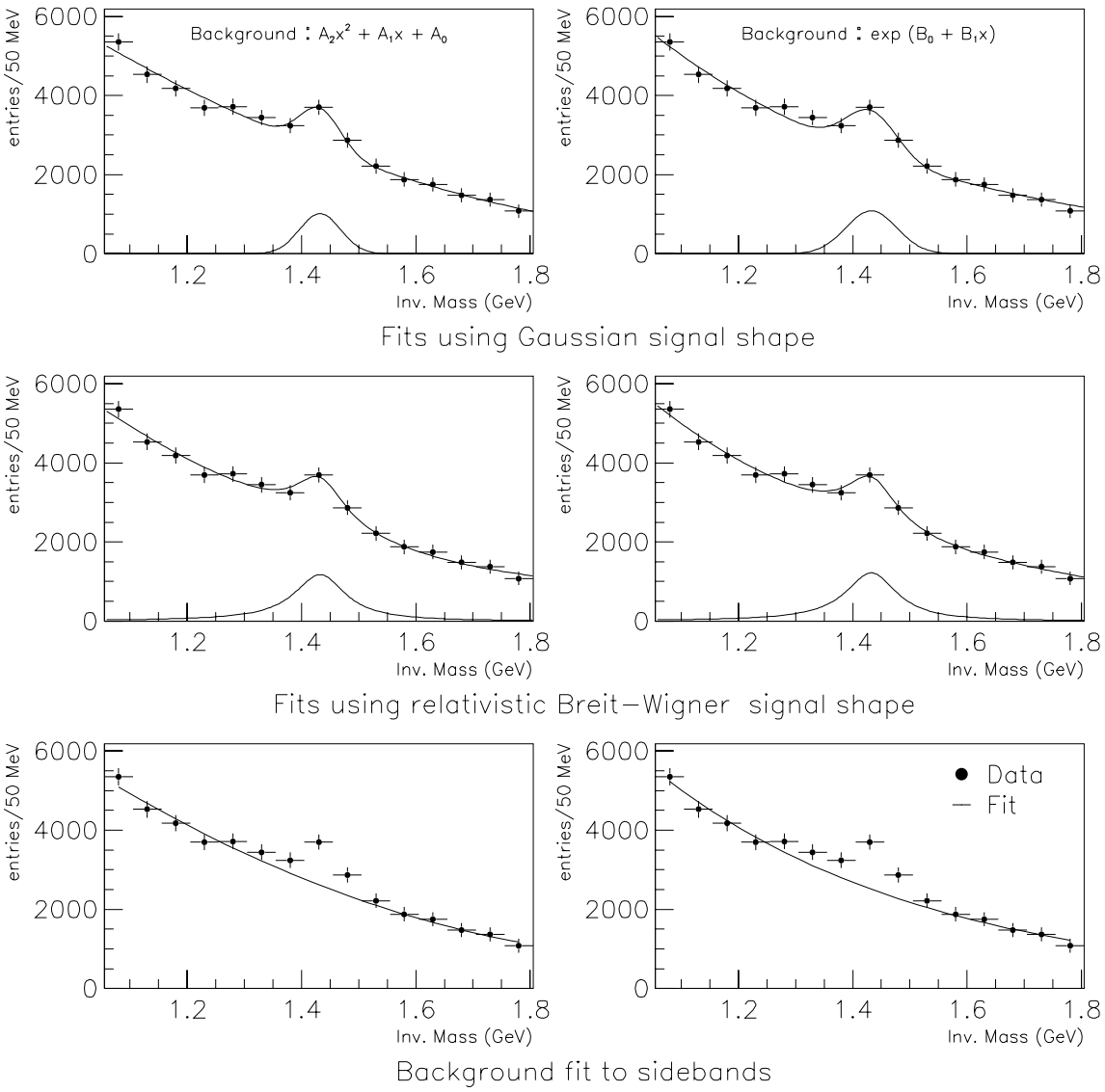

Figure 8.2: Fits to the 'subtracted' Kπ invariant mass spectrum using various functions to represent the $K_2^*(1430)^0$ signal and background.

8.2 Acceptance determination

The detector acceptance was determined from the JETSET and HERWIG Monte Carlo samples using unrelated $K\pi$ tracks with invariant mass within the signal mass region. Decays of the $K_2^*(1430)^0$ to $K\pi$ from the HERWIG events were also investigated. It was expected that the angular distribution of the $K\pi$ combinations in the centre of mass frame would be different for the two sources, the $K_2^*(1430)^0$ products decaying isotropically and the unrelated tracks showing a bias towards the jet axis of the event. This effect can be seen for $K\pi$ combinations generated by HERWIG in Figures 8.3 and 8.4. The angle θ^* is that between the kaon direction in the $K\pi$ rest system and the combined momentum vector of the two tracks in the lab.

As the inclusive kaon momentum spectrum is harder than the inclusive pion spectrum [4], possibly due to kaons produced in the decay of high momentum charm and bottom hadrons, in any unrelated $K\pi$ combination there is a tendency for the kaon to have the larger momentum. This difference in momentum is on average large enough to overcome the effect of the Lorentz boost into the $K\pi$ rest system which, because of the kaon's larger mass, would reduce the value of the kaon momentum more than that of the pion. Thus overall the kaons still tend to be forward in the $K\pi$ rest frame and this results in a bias towards positive $\cos\theta^*$, as seen in figure 8.4.

Both the angular distribution and integrated acceptance for unrelated combinations were found to be consistent for the two different Monte Carlo samples. However the acceptance was found to be significantly larger over the whole angular range for those $K\pi$ combinations from the decay of the meson, as shown in figure 8.5.

In order to determine whether this effect was specific to the fragmentation model used by HERWIG, the acceptance and angular distributions for $K\pi$ combinations produced by JETSET were also measured. As the JETSET event sample used for the analysis did not include tensor mesons, a new sample was produced. To turn on the production of tensor mesons in the fragmentation process the JETSET parameter PARJ(17) was set to 0.5 (default value 0.0). (For an explanation of this parameter, see section 8.4.) The original JETSET sample was produced by passing the Monte Carlo events through a full simulation of the detector, but this is a very time consuming process. The new sample was instead run through the detector

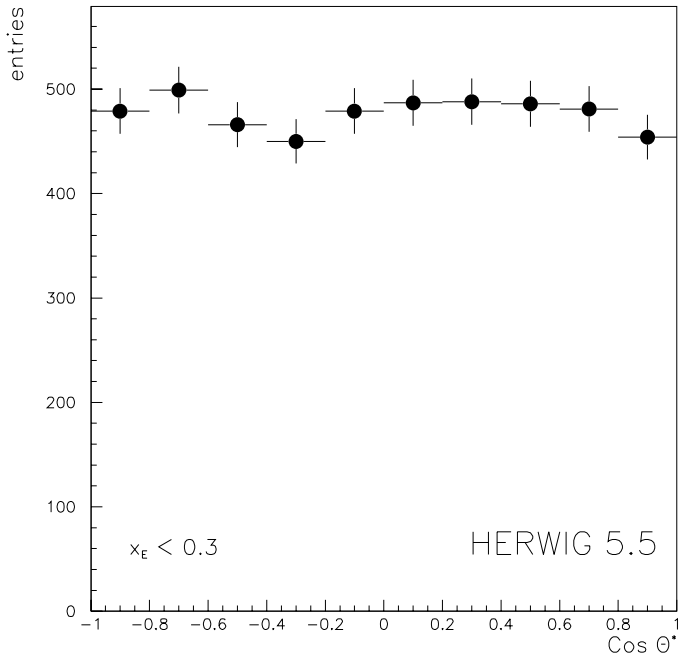

Figure 8.3: The angular distribution of kaons from Kπ combinations which originate from the decay of $K_2^*(1430)^0$ mesons.

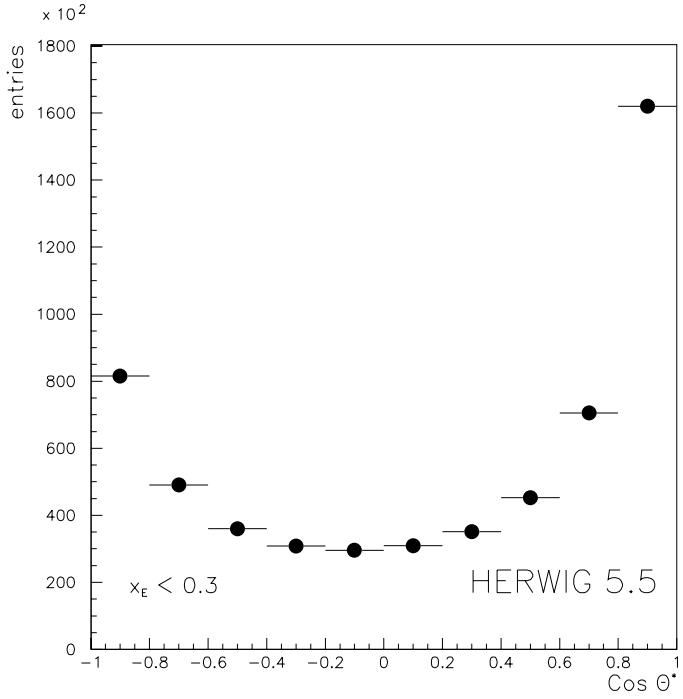

Figure 8.4: The angular distribution of kaons from unrelated Kπ combinations with two-particle invariant mass between 1.05 and 1.8 GeV.

simulation program GOPAL [32] in 'smear mode', where the detector response is simulated by smearing out the tracks with algorithms which include resolutions and efficiencies measured from the real apparatus. This process is much faster than the full simulation and is known to produce comparable results, although they cannot of course be used for the measurement of absolute efficiencies or acceptances.

The angular distributions of acceptance for Kπ two track combinations for this new JETSET event sample were measured in the same way as for the HERWIG data. The acceptance distributions for unrelated Kπ combinations from the two JETSET samples were in good agreement and so the division of the two histograms was used as a bin by bin normalisation for the distribution for combinations from $K_2^*(1430)^0$ decays, which could only be measured from the new event sample. The results are shown in figure 8.6.

As the acceptance distributions from events generated using both the Monte Carlo programs show the same discrepancy between those from unrelated Kπ combinations and those from $K_2^*(1430)^0$ decays, the source of this effect cannot be the fragmentation model. Instead it must be due to the kinematics of the events.

To check whether the effect was dependent on the size the of mass window used to select the unrelated two-particle combinations or the limits of the x_E region, both of these were varied and the distributions remeasured. Neither of these parameters were found to affect the discrepancy. The distributions were also measured with respect to several kinematic variables which could affect the acceptance, including the transverse momentum of the combined Kπ tracks with respect to the thrust axis of the event, the rapidity of the combination, and the rapidity difference between the combined tracks and all the other observed particles in the event. Unfortunately, all these studies yielded similar results to the original investigation using $\cos\theta^*$, with the acceptance significantly larger for Kπ from $K_2^*(1430)^0$ mesons over the whole range for each of the variables. It must be concluded that the reason for the difference is not yet understood. For this reason the average of the two HERWIG acceptance measurements was used to determine the inclusive $K_2^*(1430)^0$ production rate and the difference included as a part of the systematic uncertainty.

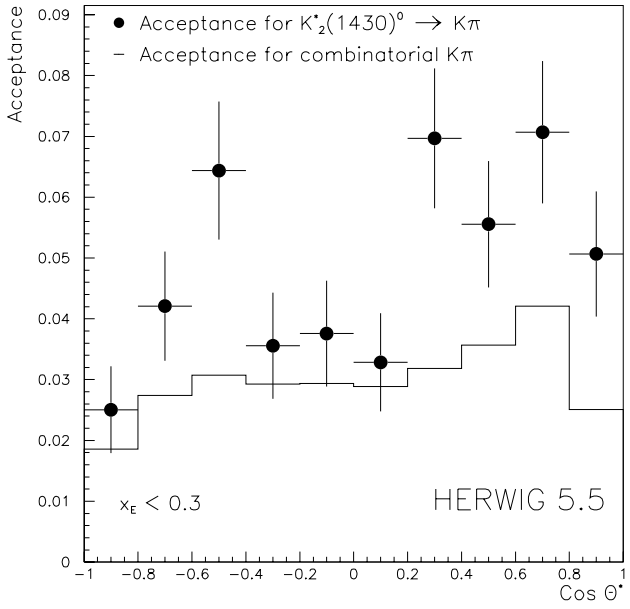

Figure 8.5: The detector acceptance for Kπ combinations, produced by the HERWIG Monte Carlo program, with respect to the angle of the kaon in the Kπ rest frame. The histogram shows the acceptance for unrelated Kπ combinations and the points are the acceptance for Kπ from the decay of $K_2^*(1430)^0$ mesons.

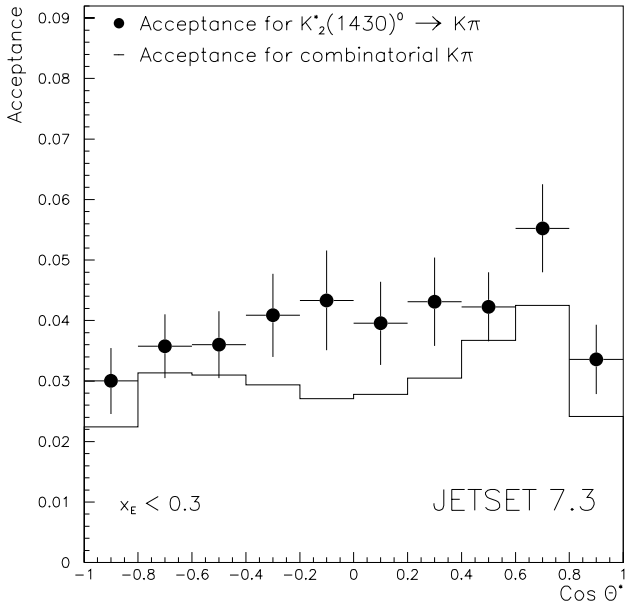

Figure 8.6: The detector acceptance for Kπ combinations, produced by the JETSET Monte Carlo program (using 'smear mode' detector simulation), with respect to the angle of the kaon in the Kπ rest frame.

Source of systematic	Uncertainty on $K_2^*(1430)^0$ rate
Acceptance determination	± 0.048
Signal fitting	± 0.027
Particle i.d. efficiency	± 0.013
Branching ratio	± 0.005
Total	± 0.057

Table 8.1: Systematic uncertainties on the $K_2^*(1430)^0$ rate.

8.3 Results

The overall multiplicity for $x_E < 0.3$ was determined to be $0.19 \pm 0.04 \pm 0.06$ $K_2^*(1430)^0$ mesons per hadronic Z^0 decay. The HERWIG prediction for this state is 0.11 mesons per Z^0 decay, just outside the measured uncertainty. The main contributions to the systematic error were from the signal and acceptance measurements as outlined above. Other smaller contributions came from $K\pi$ identification efficiency measurements and the $K_2^*(1430)^0 \rightarrow K\pi$ branching ratio. A summary of the systematic errors is given in table 8.1.

8.4 Tuning the JETSET $K_2^*(1430)^0$ production rate

The JETSET Monte Carlo program contains only one parameter which controls the production of tensor mesons in the fragmentation process, PARJ(17). This parameter actually governs the probability that a meson with its component quarks' spins aligned is produced with an orbital angular momentum of 1, giving a spin $J = 2$ for the state. The default value of PARJ(17) in the program is zero and so no tensor mesons are produced in hadronic Z^0 decays. It is possible to adjust the parameter value so that the program reproduces the measured $K_2^*(1430)^0$ rate. Changes in PARJ(17) will also affect the production of vector meson states. As the production rates of $\phi(1020)$ and $K^*(892)^0$ mesons predicted by default JETSET are significantly larger than those measured from the data in chapter 7, it is interesting to see whether the addition of tensor mesons in the Monte Carlo model improves

Particle	$x_{p/E}$ range	Measured rate	JETSET default	JETSET optimised
$\rho(770)^0$	$x_p > 0.05$	0.83 ± 0.14	0.93	0.82
$K^*(892)^0$	Full range	0.74 ± 0.04	1.05	0.84
$\phi(1020)$	Full range	0.100 ± 0.008	0.191	0.136
$f_2(1270)$	$x_p > 0.1$	0.11 ± 0.05	-	0.14
$K_2^*(1430)^0$	$x_E < 0.3$	0.19 ± 0.07	-	0.19

Table 8.2: Measurements and JETSET predictions for the inclusive rates of various mesons. The Monte Carlo values are given for PARJ(17) = 0.0 (default) and PARJ(17) = 0.3, the optimised value found using the $K_2^*(1430)^0$ measurement.

the predictions for these states.

A scan of PARJ(17) was made for values between 0.15 and 0.45, with all other JETSET parameters fixed at the default values. A level of 0.5 was already known to be too large, as the production rate of $K_2^*(1430)^0$ measured from the new JETSET sample, described in section 8.2, was almost twice the measured rate. As the measured rate was limited to $x_E < 0.3$, only Monte Carlo mesons in this range were considered. The JETSET prediction was found to be within one standard deviation of the measured $K_2^*(1430)^0$ rate for a range of PARJ(17) between 0.185 and 0.415. The central value of this range, PARJ(17) = 0.3, was used as input to JETSET, and the inclusive rates of various vector and tensor states measured. The results, together with the rates for default JETSET and experimental measurements, are given in table 8.2. The measurements for $\rho(770)^0$ and $f_2(1270)$ are taken from reference [6]. The inclusion of tensor mesons in the Monte Carlo decreases the rate of all the vector mesons listed; in the case of the $\rho(770)^0$ the new value agrees with the experimental result, but for the strange mesons the reduction is not enough to make the rates for $K^*(892)^0$ and $\phi(1020)$ comparable with the measured values. For the only other tensor meson which has been measured at LEP, the $f_2(1270)$, the JETSET prediction is in agreement with the measured production rate within large errors.

An interesting value to calculate from the results is the ratio of tensor to vector production rate for $K_2^*(1430)^0$ and $K^*(892)^0$ mesons. It is likely that this ratio will be similar for strange and non-strange mesons. A ratio for non-strange mesons of

0.22 ± 0.08 for $x_p > 0.1$ has been measured for the $f_2(1270)$ and the $\rho(770)^0$ in [6], although it should be noted that the measured $\rho(770)^0$ does not take into account the distortions in the $\pi^+\pi^-$ mass spectra. The ratio for strange particles, $K_2^*(1430)^0$ to $K^*(892)^0$, from the results in this thesis is 0.29 ± 0.10 for $x_E < 0.3$. The two values agree within rather large errors, and also agree with the JETSET predictions after adjusting the value of PARJ(17). A summary of the ratios for the data and JETSET Monte Carlo are given in table 8.3.

Particles	$x_{p/E}$ range	Measured ratio	JETSET (PARJ(17)=0.3)
$f_2(1270)$ / $\rho(770)^0$	$x_p > 0.1$	0.22 ± 0.08	0.29
$K_2^*(1430)^0$ / $K^*(892)^0$	$x_E < 0.3$	0.29 ± 0.10	0.27

Table 8.3: Measurements and JETSET predictions for the ratio of tensor to vector production rate for strange and non-strange mesons.

Chapter 9

High x_E $\phi(1020)$ production

9.1 Sources of $\phi(1020)$ in hadronic events

In a simple picture of the process $e^+e^- \rightarrow$ hadrons a ϕ meson can be produced in three main ways, illustrated in figure 9.1. The first mechanism involves the combination of a primary strange quark from the Z^0 decay with a pair-produced quark (from the sea); the second is similar, but both of the quarks are from the sea. The third source of ϕ mesons is from the decay of other hadrons. An example of this 'secondary' production is the decay of the charmed meson D_s to $\phi\,\pi$.

In the JETSET Monte Carlo program, secondary ϕ production can be easily separated from the other two sources as the history of each particle is recorded in the event record produced by the generator. The first two types cannot be distinguished using the event record as the Lund fragmentation model used in JETSET does not make a direct link between the particles produced in the parton shower process (quarks and gluons) and those created from the Lund string stretched between them (see chapter 2).

Although this means that the source of a given ϕ meson cannot be determined, it is possible to evaluate the proportion of $\phi(1020)$ from each source in a sample of events. The first type of ϕ production can only take place in events where the

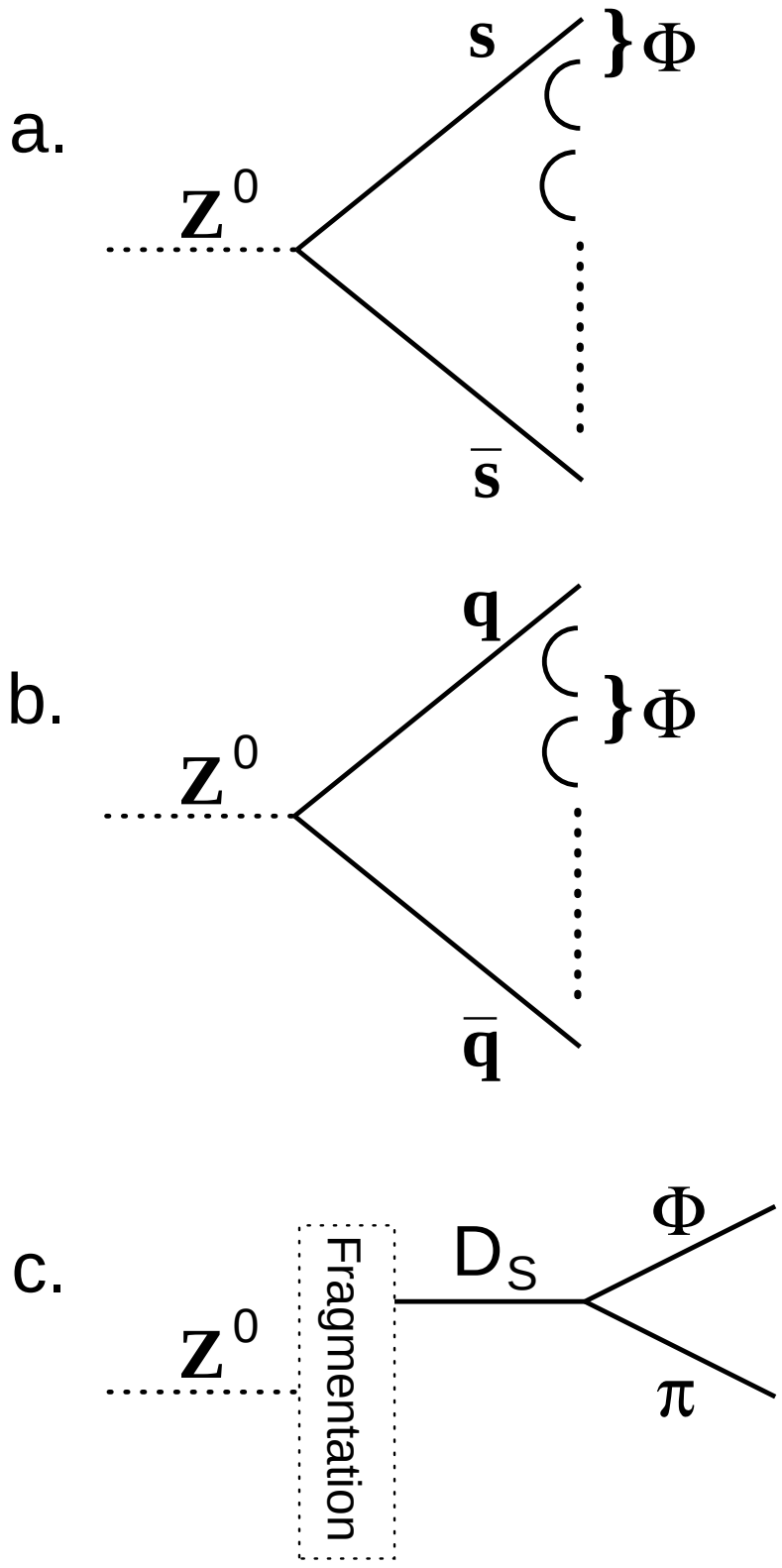

Figure 9.1: The three possible production mechanisms for $\phi(1020)$ mesons in a simple hadronisation picture: a. Including a primary strange quark from Z^0 decay; b. From sea quarks; c. Secondary production from the decay of other hadrons.

Z^0 decays to strange quarks, whereas the second type should be found in the same proportion in both $Z^0 \rightarrow d\bar{d}$ and $Z^0 \rightarrow s\bar{s}$ type events. As the flavour of a JETSET event (the type of the primary quarks) can be found from the event record, a Monte Carlo sample can be subdivided into events which can and cannot contain ϕ mesons produced from primary quarks. After removing those from decays, the number of ϕ mesons in the sample containing primary strange quarks is just the difference between the number of ϕ mesons in the strange-flavour events and the number in the down-flavour events.

It is likely that ϕ mesons produced from primary quarks will tend to have a larger proportion of the available energy than those produced from only sea quarks or from decays. In order to investigate this, the x_E spectrum for JETSET $\phi \rightarrow K^+K^-$ was divided, as outlined above, into the three production categories. Secondary ϕ mesons from hadron decays and those from Lund fragmentation were separated using the particle history in the event record, and for the latter group individual spectra were plotted for each event flavour type. The plots for up, down, charm and bottom-flavour events were found to be very similar, but the spectrum for strange-flavour events was different, with a larger proportion of ϕ mesons at high x_E. To separate out the ϕ mesons containing primary quarks, the spectrum for down-flavour events was subtracted from the strange-flavour plot. The other plots were then combined to form the contribution from ϕ mesons containing only sea quarks. The resultant x_E spectra are shown in figure 9.2.

The results from the Monte Carlo indicate that $\phi(1020)$ produced with large values of x_E are indeed more likely to be from primary quarks. In fact for $x_E > 0.45$ the contribution from sea quark production is less than 10% of the total and the main background is from secondary production.

These results indicate that by cutting on x_E it should be possible to isolate a sample of ϕ mesons in real data in which a large proportion are produced from primary quarks. Such a sample could be used to investigate the properties of the $Z^0 \rightarrow s\bar{s}$ interaction. One such property is the polarisation of the primary quarks. If a $\phi(1020)$ produced in fragmentation retains information about the spin state of its parent quark then this could be observed in the angular distribution in the decay of the meson to charged kaons.

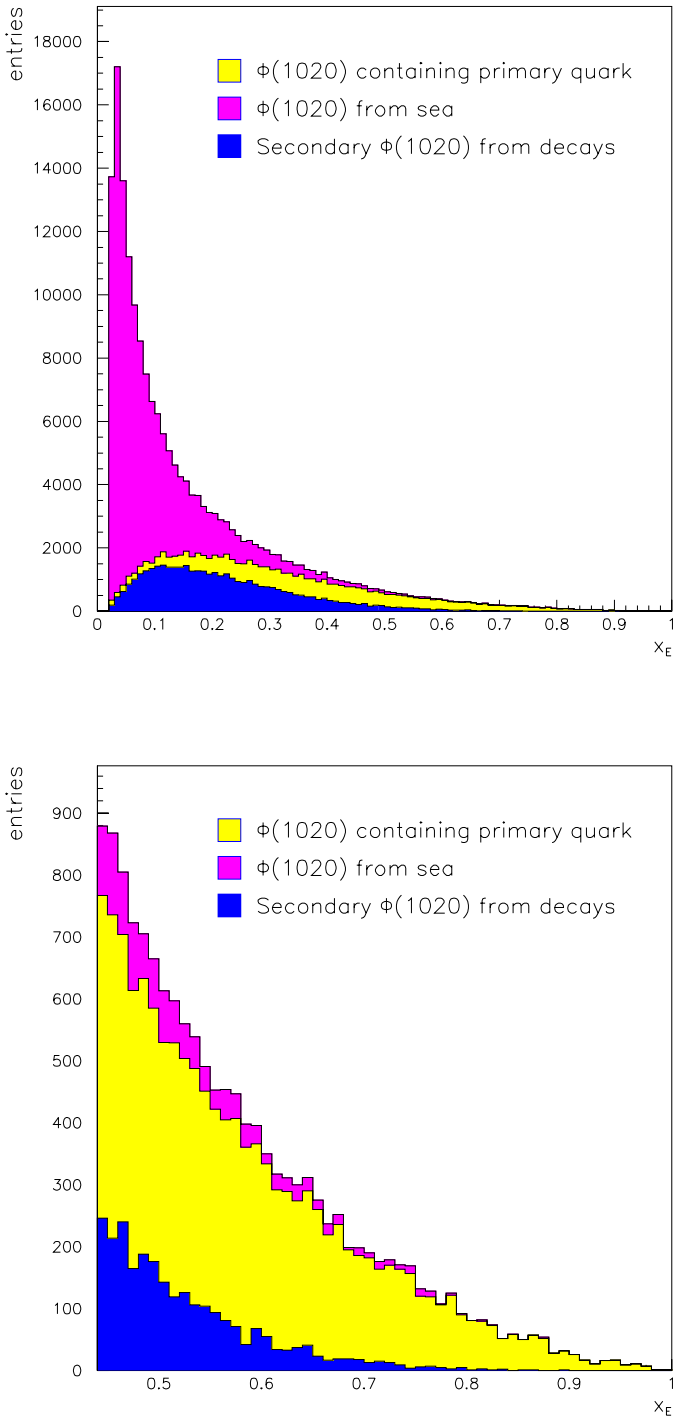

Figure 9.2: The x_E spectrum for JETSET $\phi \rightarrow K^+K^-$ showing the contributions from the three possible production mechanisms. The lower plot shows the contributions for ϕ mesons with $x_E > 0.45$.

9.2 Angular distribution of $\phi \rightarrow K^+K^-$ decays

For parity conserving decays of a hadron of spin (s, s_z) the general form of the decay angular distribution in the particle rest frame is given by W_{s,s_z} [47] :

$$W_{s,s_z}(\theta^*) = \sum_{j=0}^{l_{\max}} \alpha_j \cos^{2j}\theta^* \ . \tag{9.1}$$

Here θ^* is the decay polar angle with respect to the z axis and $l_{\max}$ is the maximum possible relative orbital angular momentum between the decay products. The values of α_j depend on the spin state of the decaying particle. If the z axis is defined by the momentum of the initial state in the lab frame then the z component of spin is proportional to the helicity of the initial state.

For a decay of the $\phi(1020)$ to charged kaons, $l_{\max} = 1$, so the distribution can be written from above as :

$$W^{\phi}_{s,s_z}(\theta^*) = \alpha_0 + \alpha_1 \cos^2\theta^* \ . \tag{9.2}$$

If the spin of the initial ϕ is aligned with the momentum, i.e. $s_z = \pm 1$, then $\alpha_1 = -\alpha_0$ and W^{ϕ} becomes

$$W^{\phi}_{1,\pm 1}(\theta^*) = \frac{3}{8\pi}\sin^2\theta^* \ ; \tag{9.3}$$

if the spin is orthogonal to the momentum then $\alpha_0 = 0$, and the distribution has the following form :

$$W^{\phi}_{1,0}(\theta^*) = \frac{3}{4\pi}\cos^2\theta^* \ . \tag{9.4}$$

The angular distribution for JETSET Monte Carlo $\phi \rightarrow K^+K^-$ for ϕ mesons from fragmentation is given in figure 9.3. As this distribution is flat, it implies that the ϕ mesons produced in Lund fragmentation have no preferred helicity state.

According to calculations using the Standard Model made in [48] strange quarks produced in Z^0 decay should be highly longitudinally polarised ($P^s_L = -0.92$). An interesting question to ask is whether this quark polarisation is transferred to the final state hadrons, or whether it is lost in the fragmentation process. In events where a ϕ meson is produced containing a primary strange quark, it might be expected that any polarisation transferred would manifest itself in the helicity of the ϕ. If

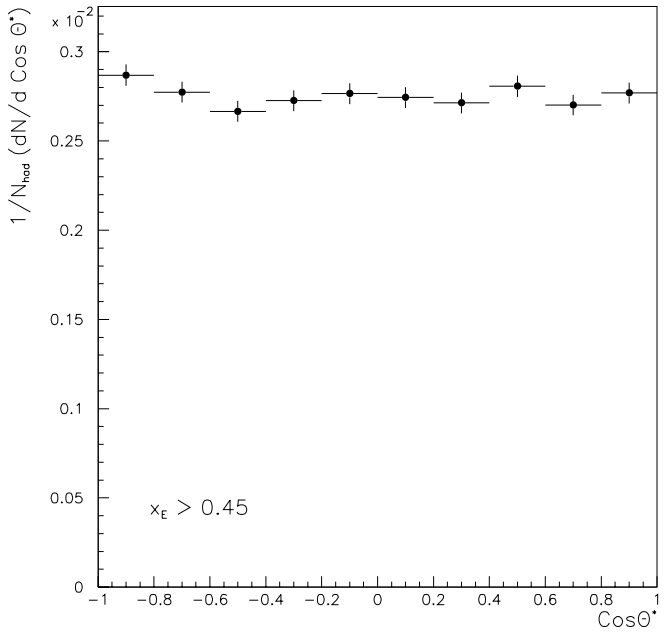

Figure 9.3: The angular distribution of $\phi \rightarrow K^+K^-$ decays in JETSET Monte Carlo, for ϕ mesons produced in Lund fragmentation.

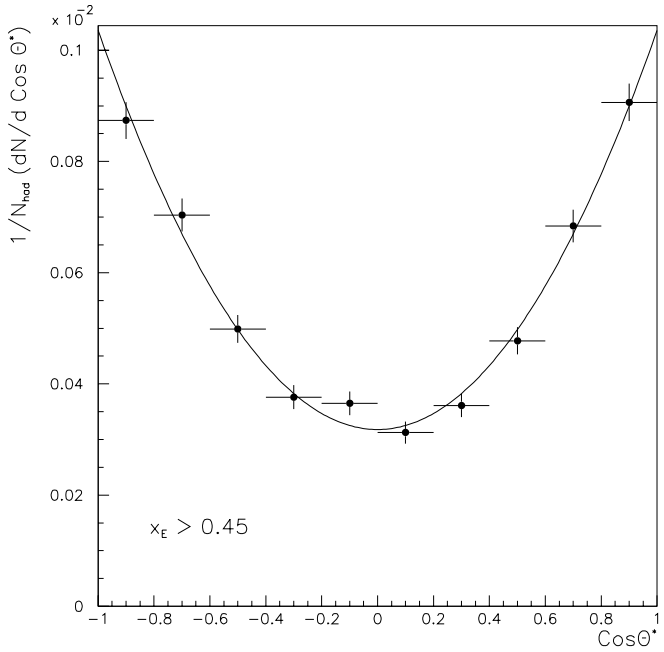

Figure 9.4: The angular distribution of $\phi \rightarrow K^+K^-$ decays in JETSET Monte Carlo, for secondary ϕ mesons produced from the decay of other hadrons. The line is a fit to the function $a_0 + a_1 \cos^2\theta^*$, the expected shape of the distribution.

this is true then the angular distribution for 'primary' $\phi(1020)$ would follow that given in equation 9.3.

The helicity of the ϕ mesons in real data can be measured by fitting the angular distribution of charged kaons from ϕ decays to the form given in equation 9.2. To determine the contributions to α_0 and α_1 which are due to ϕ production from primary quarks, the angular distributions from the other production mechanisms must be understood.

In the region $x_E > 0.45$ (figure 9.2) there is only a small contribution from ϕ mesons from the sea. According to the JETSET model this type of production has no angular dependence. The main contribution other than that from $\phi(1020)$ from primary quarks is from secondary ϕ mesons from the decay of other hadrons. Of these only those from the decay of $D_s^{\pm}$ to $\phi\pi^{\pm}$ have a non-uniform angular distribution. As this decay is pseudoscalar to vector plus pseudoscalar the final state must have a relative orbital angular momentum of one in order to conserve angular momentum. Further, the direction of this orbital angular momentum must be perpendicular to the plane of the D_s decay products. This means that the spin of the ϕ meson must also be perpendicular to the decay plane (in the opposite direction), so that it will have helicity zero and the decay angular distribution will be given by equation 9.4. The decay angular distribution for secondary produced ϕ mesons for JETSET Monte Carlo is given in figure 9.4. The plot clearly shows the $\cos^2\theta^*$ dependence from $D_s^{\pm} \to \phi\pi^{\pm}$ decays as well as the constant level from other secondary ϕ meson decays.

9.3 Measuring the angular distribution

For the real data, the KK two-particle invariant mass spectrum was constructed by combining all pairs of oppositely charged tracks in each event which passed the track quality cuts described in chapter 4, and had a combined x_E greater than 0.45. To maximise the statistics no dE/dx kaon identification was used. The main background due to $\pi^+\pi^-$ pairs (which is reduced by using kaon identification) was not really a problem as the level falls off rapidly with increasing x_E. The lower bound for x_E was a compromise between maximising the proportion of ϕ mesons which,

$\lvert\cos\theta^*\rvert$ region	Monte Carlo Acceptance	$\frac{1}{N_{\rm had}}\frac{{\rm d}N}{{\rm d}\lvert\cos\theta^*\rvert}$
0.00 – 0.33	0.35 ± 0.03	0.0032 ± 0.0007
0.33 – 0.66	0.32 ± 0.06	0.0019 ± 0.0006
0.66 – 1.00	0.29 ± 0.04	0.0027 ± 0.0007

Table 9.1: Differential rates for $\phi \rightarrow {\rm K^+K^-}$ decays at $x_E > 0.45$ in each of the three $\lvert\cos\theta^*\rvert$ regions.

according to the Monte Carlo, contained primary quarks (the greater the value of x_E the better) and producing the best possible signal to background ratio in the plots i.e. maximising the total number of $\phi(1020)$ passing the cuts. In order to measure the angular distribution the histogram was divided into three bins of $\lvert\cos\theta^*\rvert$. The absolute value was used as the distribution was expected to be symmetric about $\cos\theta^* = 0$.

The resultant mass spectra were fitted using the minimum χ^2 method to a combination of a Gaussian function for the ϕ signal and a Weibull function (equation 7.2) over a mass range from the KK threshold up to 1.07 GeV. A Gaussian was used, rather than the relativistic Breit-Wigner used elsewhere in the analysis, as the two-particle mass resolution of the detector in the x_E region in question is around 20 MeV, much greater than the natural width of the state. The mass spectra together with the results of the fits are shown in figure 9.5.

The acceptance for each of the $\lvert\cos\theta^*\rvert$ bins was measured from the Monte Carlo event sample, using the information available regarding the generated and reconstructed type of each track. By combining these acceptance measurements with the results from the fits the differential rate in each of the $\lvert\cos\theta^*\rvert$ bins was calculated. The results are given in table 9.1. These values were used to plot the angular distribution of the kaons in ϕ decays, shown in figure 9.6. The errors shown are a combination of the statistical uncertainties from the fits to the mass spectra and systematic errors from the acceptance measurements.

The measured angular distribution was fitted to the form given in equation 9.2. The fitted parameters were found to be $\alpha_0 = 0.026 \pm 0.006$ and $\alpha_1 = -0.003 \pm 0.013$. These results are compatible with a flat distribution, indicating that there is no

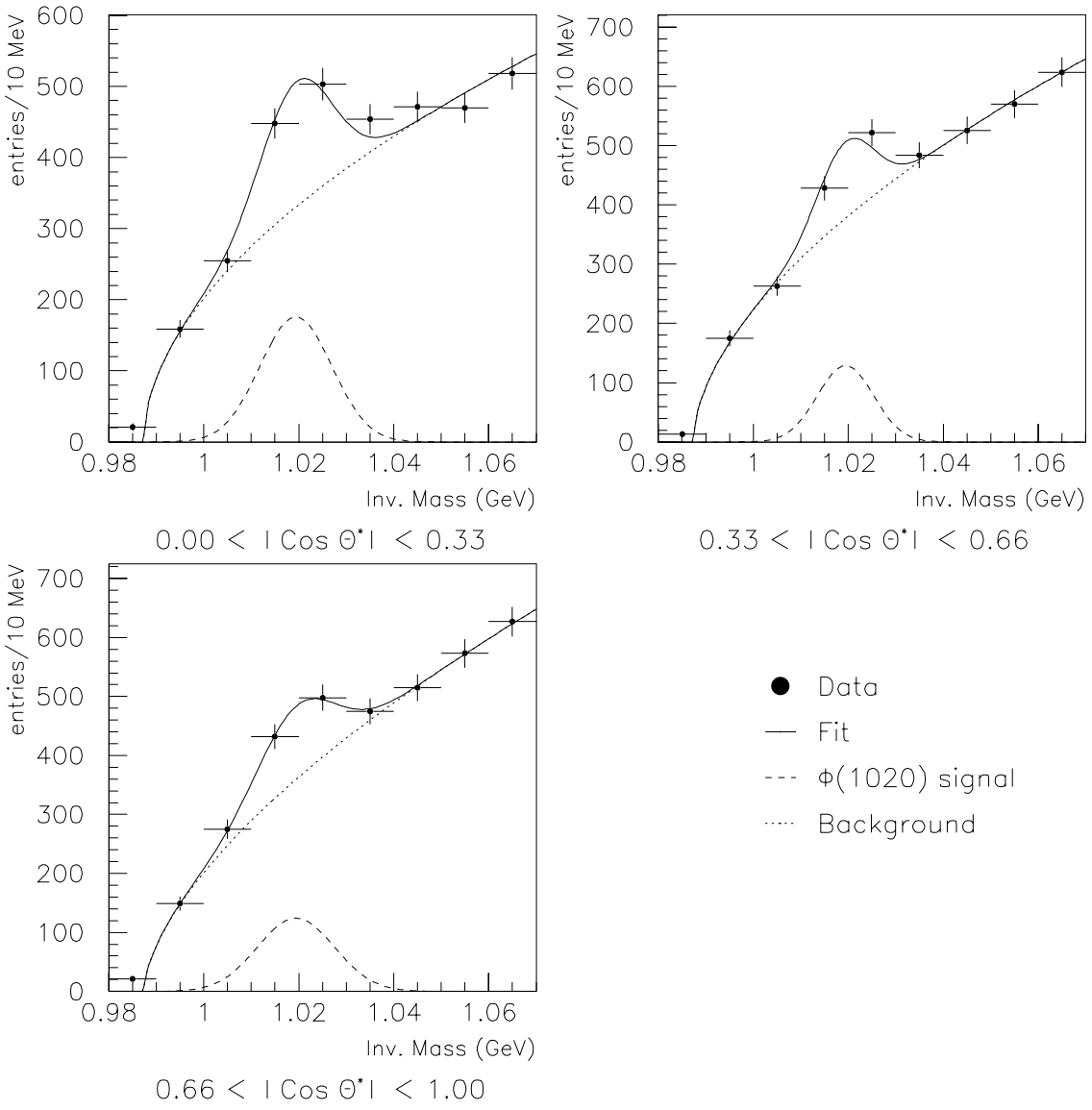

Figure 9.5: The KK two-particle invariant mass spectra for $x_E > 0.45$ in three bins of $|\cos\theta^*|$. The fits are a combination of Gaussian and Weibull functions.

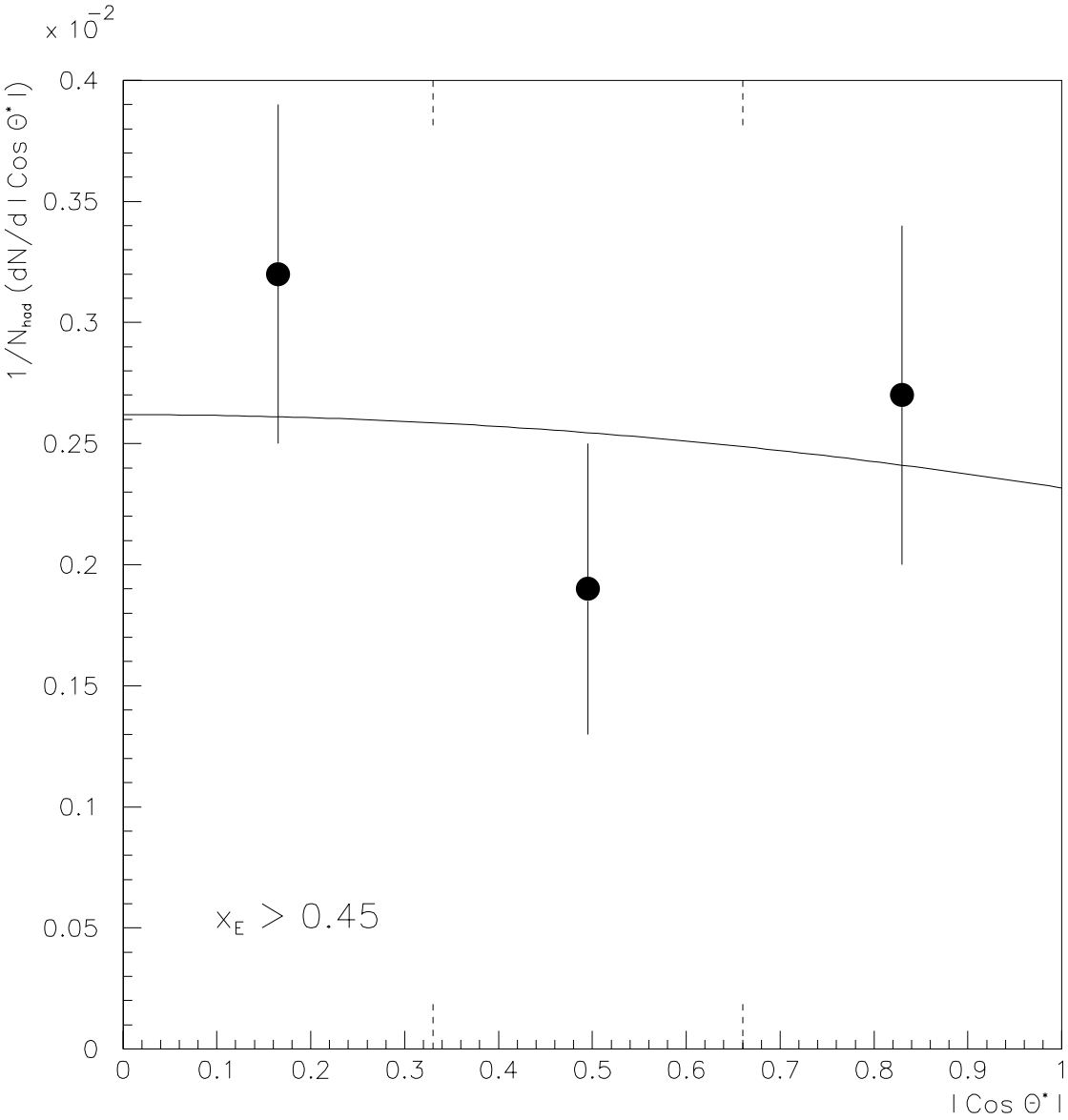

Figure 9.6: The angular distribution with respect to $|\cos\theta^*|$ of charged kaons from the decay of $\phi(1020)$ mesons with $x_E > 0.45$. The bin ranges are indicated by means of the short vertical lines at the edges of the plot. The line on the plot is a fit to the form given in equation 9.2.

evidence for a preferred helicity state in overall ϕ production with $x_E > 0.45$ in the data.

9.4 Conclusions

As outlined in section 9.2 the shape of the overall angular distribution depends on two factors, the helicity state of the ϕ mesons which contain primary quarks and the size of the contribution from secondary ϕ mesons from D_s decays. If the longitudinal polarisation of the primary strange quarks is transferred to the 'primary' mesons then the distribution should follow that given in equation 9.3, with the differential rate tending to zero as $|\cos\theta^*| \rightarrow 1$. However this effect could be diluted by the contribution from ϕ mesons produced in $D_s \rightarrow \phi\pi$ decays which would decay according to equation 9.4. In order to remove this contribution, to see the underlying distribution due to ϕ mesons which contain primary quarks, the inclusive D_s production rate is required. Unfortunately, this quantity has not been measured at LEP at the present time, and so no real conclusions can be made.

According to JETSET (figure 9.2) the contribution to ϕ production from decays of other hadrons such as the D_s decreases rapidly with increasing x_E. With larger multihadronic statistics it may be possible to eliminate the effect of secondaries by cutting on a higher value of x_E, and hence to determine the helicity state of the ϕ mesons which contain primary strange quarks directly, from the resulting angular distribution.

Although this study must be regarded as only preliminary, it has shown that the angular distribution of the decay $\phi \rightarrow K^+K^-$ at high x_E can be measured using two-particle invariant mass spectra. This could prove a useful tool in future analyses.

Chapter 10

Discussion and conclusions

In this thesis, measurements are given of the inclusive production rates of the strange vector mesons $K^*(892)^0$ and $\phi(1020)$ and the tensor meson $K_2^*(1430)^0$ in hadronic Z^0 decays. The results for the vector states are in agreement with those from an earlier OPAL analysis [1] but provide a significant improvement in precision. The $K_2^*(1430)^0$ rate represents the first measurement of a strange tensor meson at LEP.

Table 10.1 contains a summary of the inclusive rate measurements. Also shown in the table are the rates predicted by the Monte Carlo programs JETSET and HERWIG. For JETSET with the default OPAL parameter set (tuned to reproduce the overall event shapes) the rates for both $\phi(1020)$ and $K^*(892)^0$ are significantly larger than the measured values. The JETSET expectation for the $\phi(1020)$ is almost twice the measured rate. The HERWIG predictions for the vector mesons, although better than default JETSET, are still over two standard deviations from the measured multiplicities. The inclusive rate for the $K_2^*(1430)^0$ from HERWIG is just outside the measured uncertainty.

Also listed in the table are the multiplicities obtained from JETSET after certain parameters had been adjusted. The first of the two sets of 'tuned' JETSET results is based on a study carried out in [1] and described in chapter 7. The two parameters altered were PARJ(2), the strangeness suppression factor, and PARJ(12) which is

	$K^*(892)^0$	$\phi(1020)$	$K_2^*(1430)^0$
Measurement	0.74 ± 0.04	0.100 ± 0.008	0.19 ± 0.07
JETSET default OPAL	1.05	0.191	-
JETSET tuned PARJ(2), PARJ(12)	0.71	0.115	-
JETSET tuned PARJ(17)	0.84	0.136	0.19
HERWIG	0.87	0.136	0.11

Table 10.1: Summary of the inclusive rate measurements for vector and tensor mesons made in the analysis, together with the predictions of the JETSET and HERWIG Monte Carlo programs. The K_2^* measurement is for $x_E < 0.3$.

the probability that a strange meson will have spin 1. With these parameters set so that the program reproduces a number of measured production rates, the predicted multiplicity for $K^*(892)^0$ is in agreement with the measurement but the $\phi(1020)$ rate is still too large by around two standard deviations. The second set of tuned JETSET results come from work described in chapter 8. The parameter which controls the level of tensor meson production, PARJ(17), was varied in order to get the program to reproduce the measured inclusive $K_2^*(1430)^0$ rate. This parameter also affects the level of vector meson production, reducing the rates for $\phi(1020)$ and $K^*(892)^0$ mesons.

With the extra degree of freedom introduced by including tensor mesons in the Monte Carlo it may be possible to tune the values of all three parameters mentioned above simultaneously, using the multiplicities for mesons and baryons which have been measured by all four LEP experiments. Such a study is beyond the scope of this thesis. This method of tuning is almost certainly not unique; other combinations of parameters could also be used to get the same effect on the particle rates. However any procedure which can improve the simulation of LEP physics is a useful exercise.

The fragmentation functions for the two vector mesons have been measured and for the first time the differential cross sections have been plotted with respect to the variable $\xi = \ln(1/x_p)$. The Gaussian-like shape for these distributions, predicted by the modified leading logarithm approximation in QCD with the hypothesis of local parton-hadron duality (MLLA+LPHD) [16], has been confirmed and the peak values of ξ measured. When plotted against particle mass (figure 7.8) the $\xi_{\rm peak}$ values

for the measured vector mesons and other hadron states were found to be in broad agreement with the predictions of the JETSET Monte Carlo program, but not with the MLLA+LPHD prediction of a linear decrease in $\xi_{\rm peak}$ with increasing hadron mass. However, when only primary hadrons were considered in the Monte Carlo an agreement with MLLA+LPHD was found. It was concluded that the inclusion of secondary particles from the decay of other hadrons smears out the simple mass dependence, thus producing the effect observed in the data.

Three possible mechanisms for ϕ-meson production in multihadronic events were investigated using the JETSET Monte Carlo program. The first mechanism involves the combination of a primary s or $\bar{\rm s}$ quark from the Z^0 decay with a pair-produced quark from the sea. In the second type of ϕ-meson production both the constituent quarks are from the sea. (In terms of the Lund model of fragmentation used in JETSET this quark pair-production results from the break-up of a string.) The third type is secondary production where the ϕ mesons are from the decay of other hadrons. It is likely that ϕ mesons produced from primary quarks will tend to have a larger proportion of the available energy than those produced from only sea quarks or from decays. This was confirmed by plotting the x_E spectra for ϕ mesons from the three sources, as shown in figure 9.2. This meant that by cutting on x_E a sample of ϕ mesons could be isolated in the real data in which a large proportion are produced from primary quarks.

The Standard Model predicts that strange quarks produced in Z^0 decay are longitudinally polarised. If this property is transferred to final state ϕ mesons which contain one of the primary quarks then it is likely to manifest itself as a polarisation of the ϕ mesons. The angular distribution of $\phi \rightarrow {\rm K^+K^-}$ decays from such a sample (with $x_E > 0.45$) was measured by fitting the KK two-particle invariant mass spectra in bins of decay angle $|\cos\theta^*|$. The resulting distribution was found to be flat, indicating that overall the ϕ mesons have no preferred helicity. However any angular dependence could have been diluted by the presence of secondary ϕ mesons from the decay $\rm D_s \rightarrow \phi\,\pi$. In order to extract the distribution from ϕ mesons containing primary quarks the inclusive production rate for $\rm D_s$ must be known. Unfortunately, this quantity has not at the present time been measured at LEP. Clearly future studies of high x_E ϕ-meson production in multihadronic events will be useful.

Appendix A

The signal shape for a two body decay

The Breit-Wigner approximation [42] provides a good model of the line shape for a resonance decay. In this approximation the variation of signal intensity with mass is given by the relativistic Breit-Wigner formula :

$$RBW(m) = \frac{C\, m_0^2\, \Gamma(m)^2}{(m_0^2 - m^2)^2 + m_0^2\, \Gamma(m)^2} \ , \tag{A.1}$$

where C is a normalisation constant and m_0 is the peak mass of the resonance. The mass dependent width, $\Gamma(m)$, for a two-body decay can be written, from [42], as

$$\Gamma(m) = \Gamma(m_0) \left(\frac{q(m)}{q(m_0)} \right)^{2l+1} \frac{\rho(m)}{\rho(m_0)} \ . \tag{A.2}$$

In this expression $\Gamma(m_0)$ is the width of the state at the resonance mass, l is the orbital angular momentum of the decay products and $q(m)$ is the momentum of each product particle in the centre of mass frame of the decay. The term $\rho(m)$ is a 'relatively slowly varying function' which depends on the decay type. If the decay products are A and B, $q(m)$ can be written in terms of the particle masses as follows

$$q(m)^2 = \frac{(m^2 - m_A^2 + m_B^2)^2}{4m^2} - m_B^2 \ . \tag{A.3}$$

The relativistic Breit-Wigner formula was used extensively in the present analysis to model the line shape of $\mathrm{K}^*(892)^0$, $\phi(1020)$ and $\mathrm{K}_2^*(1430)^0$ decays. For the

vector mesons the orbital angular momentum term l is unity as the decays are both vector to two pseudoscalar states. According to [42], to the lowest order in perturbation theory the form of $\rho(m)$ depends on the parity and the spin of the particles involved. For the vector meson decays in question the appropriate form is given as :

$$(1^-) \rightarrow (0^-)(0^-) \ , \ l = 1 \quad : \quad \rho(m) = m^{-1} \ . \tag{A.4}$$

By substituting the value for l and expression for $\rho(m)$ into equation A.2, the mass dependent width for $\phi(1020)$ and $\mathrm{K}^*(892)^0$ can be written

$$\Gamma(m) = \Gamma(m_0) \left(\frac{q(m)}{q(m_0)} \right)^3 \left(\frac{m_0}{m} \right) \ . \tag{A.5}$$

For the analysis of the tensor state $\mathrm{K}_2^*(1430)^0$ the full form of $\Gamma(m)$ given in equation A.2 could not be used as reference [42] does not list the appropriate form for $\rho(m)$. Instead the ρ term was removed and the width was calculated according to :

$$\Gamma(m) = \Gamma(m_0) \left(\frac{q(m)}{q(m_0)} \right)^5 \ . \tag{A.6}$$

Bibliography

[1] P. D. Acton et al., OPAL Coll.: Z. Phys. C56 (1992) 521.

[2] B. Adeva et al., L3 Coll.: Phys. Lett. B259 (1991) 119;
D. Buskulic et al., ALEPH Coll.: Phys. Lett. B292 (1992) 210-220;
O. Adriani et al., L3 Coll.: Phys. Lett. B286 (1992) 403;
P. Abreu et al., DELPHI Coll.: Phys. Lett. B275 (1992) 231.

[3] G. Alexander et al., OPAL Coll.: Phys. Lett. B264 (1991) 467.

[4] R. Akers et al., OPAL Coll.: "Measurement of the Production Rates of Charged Hadrons in e^+e^- Annihilation at the Z^0", CERN-PPE/94-49.

[5] P. D. Acton et al., OPAL Coll.: Phys. Lett. B305 (1993) 407.

[6] P. Abreu et al., DELPHI Coll.: Phys. Lett. B298 (1993) 236.

[7] T. Sjöstrand: Comp. Phys. Commun. 39 (1986) 347;
T. Sjöstrand: Comp. Phys. Commun. 43 (1987) 367;
M. Bengtsson and T. Sjöstrand: Nucl. Phys. B289 (1987) 810.

[8] I. J. R. Aitchison and A. J. G. Hey: "Gauge Theories in Particle Physics", 2nd Edition, Adam Hilger (1989).

[9] S. L. Glashow: Nucl. Phys. 22 (1961) 579;
A. Salam: "Elementary Particle Theory", ed. N. Svartholm, Almqvist (1968) 367;
S. Weinberg: Phys. Rev. Lett. 19 (1967) 1264.

[10] R. P. Feynman: "The Theory of Fundamental Processes", New York: Benjamin (1962) Ch. 5.

[11] G. Marchesini and B.R. Webber: Nucl. Phys. B310 (1988) 461;
G. Marchesini et al.: Comp. Phys. Commun. 67 (1992) 465.

[12] L. Lönnblad: "A Manual for ARIADNE Version 3", LU TP 89-10 (June 1989).

[13] R. Odorico, University of Bologna preprint DFUB 88-27 (1988).

[14] S. Ritter: Computer Physics Commun. 31 (1984) 401;
R. Kirschner, S. Ritter: Physica Scripta 23 (1981) 763;
S. Ritter: Z. Phys. C16 (1982) 27.

[15] Y. I. Azimov, Y. L. Dokshitzer, V. A. Khoze and S. I. Troyan: Z. Phys. C27 (1985) 65;
Y. I. Azimov, Y. L. Dokshitzer, V. A. Khoze and S. I. Troyan: Z. Phys. C31 (1986) 213.

[16] Y. L. Dokshitzer, V. A. Khoze and S. I. Troyan : J. Phys. G: Nucl. Part. Phys. 17 (1991) 1481;
Y. L. Dokshitzer, V. A. Khoze and S. I. Troyan : Z. Phys. C55 (1992) 107.

[17] "Z Physics at LEP 1", ed. G. Altarelli et al., CERN 89-08 Vol. 3 p.157.

[18] B. Andersson, G. Gustafson, T. Sjöstrand: Physica Scripta 32 (1985) 574.

[19] P. Acton et al., OPAL Coll.: Phys. Lett. B305 (1993) 415;
D. Buskulic et al., ALEPH Coll.: "Production of K^0 and Lambda in Hadronic Z Decays", CERN-PPE/94-074;
P. Abreu et al., DELPHI Coll.: Phys. Lett. B318 (1993) 249.

[20] R. Akers et al., OPAL Coll.: "An Update of the Z^0 Line Shape and Lepton Asymmetry Measurements with 1993 data for the 1994 Summer Conferences.", OPAL Physics Note PN143 (1994);
The LEP Collaborations : ALEPH, DELPHI, L3 and OPAL: Phys. Lett. B276 (1992) 247.

[21] G. Alexander et al., OPAL Coll.: Z. Phys. C52 (1991) 175.

[22] R. Hemingway: "Inclusive Particle Production in Z^0 Decays", ICHEP, Glasgow (1994).

[23] V. Gibson: "Charm and Beauty Hadron Production at $\sqrt{s} \sim M_{Z^0}$", ICHEP, Glasgow (1994);
R. Batley: "Electroweak b physics results from LEP", DPF-94, Albuquerque, New Mexico (1994).

[24] M. Z. Akrawy et al., OPAL Coll.: Phys. Lett. B236 (1990) 364.

[25] D. Buskulic et al.: ALEPH Coll.: Phys. Lett. B313 (1993) 312;
P. Abreu et al., DELPHI Coll.: "Search for the Standard Model Higgs Boson in Z^0 Decays", CERN-PPE/94-46;
O. Adriani et al., L3 Coll.: Phys. Lett. B303 (1993) 391;
R. Akers et al., OPAL Coll.: Phys. Lett. B327 (1994) 397.

[26] D. Decamp et al., ALEPH Coll.: Phys. Lett. B237 (1990) 291;
R. Akers et al., OPAL Coll.: "Search for Neutral Higgs Bosons in the Minimal Supersymmetric extension of the standard model", CERN-PPE/94-120;
R. Akers et al., OPAL Coll.: "Search for a Scalar Top Quark Using the OPAL Detector", CERN-PPE/94-103;
M. Z. Akrawy et al., OPAL Coll.: Phys. Lett. B240 (1990) 261.

[27] Proceedings of the ECFA Workshop on LEP 200, ed. A. Böhm, W. Hoogland, CERN 87-08.

[28] K. Ahmet et al., OPAL Coll.: Nucl. Instr. and Meth. A305 (1991) 275.

[29] P. Allport et al.: Nucl. Instr. and Meth. A324 (1993) 34;
P. Allport et al.: Nucl. Instr. and Meth. A346 (1994) 476.

[30] M. Z. Akrawy et al., OPAL Coll.: "The Trigger System of the OPAL Experiment at LEP", CERN-PPE/91-32.

[31] D. Charlton et al.: Nucl. Instr. and Meth. A325 (1993) 129.

[32] J. Allison et. al.: Nucl. Instr. and Meth. A317 (1992) 47.

[33] R. Brun et al.: "GEANT3 Users' Guide", CERN-DD/EE/84-1.

[34] M. Z. Akrawy et al., OPAL Coll.: Z. Phys. C47 (1990) 505.

[35] H. A. Bethe: "Handbuch der Physik 24/1", J. Springer Verlag Berlin (1933) 491.

[36] A. V. Alakoz et al.: Nucl. Instr. and Meth. 124 (1975) 41.

[37] M. Hauschild et al.: Nucl. Instr. and Meth. A314 (1992) 74.

[38] Particle Data Group: Physical Review D45, Part 2 (June 1992).

[39] P. Acton et al., OPAL Coll.: Phys. Lett. B267 (1991) 143.

[40] P. Abreu et al., DELPHI Coll.: "Invariant Mass Dependence of Particle Correlations in Hadronic Final States from the Decay of the Z^0", CERN-PPE/94-02.

[41] G. D. Lafferty: Z. Phys. C60 (1993) 659.

[42] J. D. Jackson: Nuovo Cim. 34 (1964) 1644.

[43] F. James: CERN Program Library, Ref W515.

[44] G. D. Lafferty and T.R. Wyatt: "Where to Stick Your Data Points: The Treatment of Measurements Within Wide Bins", CERN-PPE/94-72.

[45] I. N. Bronshtein and K. A. Semendyayev: "Handbook of Mathematics", Van Nostrand Reinhold, 1979.

[46] P. D. Acton et al., OPAL Coll.: Phys. Lett. B291 (1992) 503;
M. Acciarri et al., L3 Coll.: "Measurement of Inclusive Production of Neutral Hadrons from Z Decays", CERN-PPE/94-53.

[47] S. U. Chung: "Spin Formalisms", CERN 71-8.

[48] Kuhn and Zerwas: Nucl. Phys. B272 (1986) 560.

Acknowledgements

First and foremost I would like to thank my supervisor George Lafferty for an immense amount of help and support over the last three years and especially in the preparation of this thesis. Thanks must also go to all the members of the Manchester HEP group, in particular John Allison for the help with GEANT, Roger Barlow for all matters statistical and Fred Loebinger for... well everything from lunchtime conversation to his organisational wizardry. A special thank you to Bill Gary at CERN for an excellent summary of HERWIG, faxed all the way to the UK.

To the Crossword crew, Rob, Jane, Andy (and Roger) I did manage a few clues! and to all the students who have been around during the last year, Stuart, Nick T., Gareth, Bob, Jim, Nick O., Oliver, Sue and Ben, for livening up the process of writing up (and giving me excuses to take a break once in a while, "me know about PAW, never!").

To all my friends at CERN for help, inspiration and lots of pizza: Charles 'Chuckie' Jui, good luck with your new job - I'll drink to that (cos. you can't in Utah!), Jim Letts - 'I'm sorry ma'am, thats a matter of national security' and Teresa, Paul 'Casper' Schenk and Rita (and the turtles) and Shunlung 'break a leg' Chu. On the computing side thanks to the UC Riverside group for the use of their facilities during my second year; (the rent cheque is in the post Bill!)

Acknowledgements must go to all the members of the OPAL collaboration and LEP machine group at CERN, without whom none of the analysis would have been possible.

A big hello to my friends outside HEP, to Paul Floyd (it will all be over by Christmas), Rob Cummings, for help more times than I can count in the last three years and to Frode Tennebœ for the E-mail insights into Norwegian life!

Finally I must thank my family for twenty-four years of putting up with a developing physicist, and to Emma for love and support and for *nearly* believing me when I said it was a real job.